Wave Energy Converter Design via a Time-Domain Rankine Panel Method

by

João Seixas de Medeiros

B.S., Naval and Oceanic Engineering
Federal University of Rio de Janeiro (UFRJ)

Submitted to the Department of Mechanical Engineering
in partial fulfillment of the requirements for the degree of

Master of Science in Mechanical Engineering

at the

MASSACHUSETTS INSTITUTE OF TECHNOLOGY

February 2017

Author .... Signature redacted
Department of Mechanical Engineering
Jan 15, 2017

Certified by........... Signature redacted
Stefano Brizzolara
Visiting Research Scientist, PI
Thesis Supervisor

Accepted by .... Signature redacted
Rohan Abeyaratne
Chair, Mechanical Engineering Graduate Program Committee

Wave Energy Converter Design via a Time-Domain Rankine Panel Method

by

João Seixas de Medeiros

Submitted to the Department of Mechanical Engineering
on Jan 15, 2017, in partial fulfillment of the
requirements for the degree of
Master of Science in Mechanical Engineering

Abstract

Efficient design of energy converters heavily depends on the capacity of the designer to accurately predict the device's dynamic, which ultimately leads to the power extraction. This is specially true for wave energy converters (WEC), which usually present a high cost per kWh generated. In this thesis a particular WEC which uses a rotating mass for power extraction is studied. A numerical model for the prediction of its motion and power extraction is presented. The nonlinear dynamic model consists of a time-domain three dimensional Rankine panel method coupled, in the time integration, with a MATLAB algorithm which solves for the equations of the gyroscope and Power Take-Off (PTO). The former acts as a force block, calculating the forces due to the waves on the hull, which is then sent to the latter through TCP/IP, which couples the external dynamics and performs the time-integration using a 4th order Runge-Kutta method.

With the proposed code, two case studies are examined. The first consists of two gyroscopes, rotating in opposite directions, to negate undesirable yaw effects on the WEC's hull. The device's optimum PTO damping value and flywheel spin are then shown, which change for different sea states. The second is a comparison against results from experimental testing of a 1:50 model at the Davidson Laboratory during the Wave Energy Prize.

Thesis Supervisor: Stefano Brizzolara
Title: Visiting Research Scientist, PI

Acknowledgments

As this chapter of my journey ends, I would like to thank my advisor, Dr. Stefano Brizzolara for all the support he gave me. His guidance was fundamental to my return to MIT for graduate school, as well as for my growth as an engineer and as a person.

To all my friends, especially the MIT ones, for sharing this road with me. Pedro, Rafa, Isaura, Diogo, Ivo, Sam, Abiodun, Victor, Sahil, Malivai, Audren, Dixia and Jacob, just to name a few, made my day-to-day much more enjoyable. I hope to keep seeing these faces every day, as I embark into the PhD.

To Heloisa, for putting up with me. You are one of the best friends I could have ever asked for.

Finally, to my parents, Claudio and Cristiana, as well as my brother Pedro and my grandmothers Ana and Lia. I wouldn't be half the man I am today if it was not for their everlasting love and care. Also my grandparents Arthur and Sergio, wherever they may be, for always looking after me and instigating my passion for science.

The present work was done with support from the Brazilian National Council of Scientific and Technology Development (CNPq)

Contents

List of Figures

List of Tables

List of Symbols

a_{ij}	Added mass matrix, one of the constituents of the wave radiation forces
a^o_{ij}	Added mass matrix due to impulsive motion of the body, usually called infinite frequency added-mass
A	Wave amplitude
$\mathbf{B}$	Hull's maximum beam
b_{ij}	Damping matrix, one of the constituents of the wave radiation forces
$b^o_{ij}(\infty)$	Damping matrix due to impulsive motion of the body
c_{ij}	Restoration matrix
c^o_{ij}	Restoration matrix due to impulsive motion of the body
c_l	Power Take-Off linear damping constant
$\mathbf{D}$	Hull's depth
d	Gyroscope diameter
E	Total wave energy density per unit area of the mean free surface
$\overline{E}$	Total averaged wave energy density per unit area of the mean free surface over one period
$\mathfrak{F}$	Energy flux across a control volume $\mathcal{V}$

$f_k(t)$ Wave force signal exciting the body motion

g Gravitational acceleration

h Water depth ($y < 0$)

H Wave height

I_{xx} Gyroscope's flywheel roll inertia

I_{yy} Gyroscope's flywheel pitch inertia

J Gyroscope's flywheel spin inertia

I_x^f Gyroscope frame roll inertia

I_y^f Gyroscope frame pitch inertia

I_z^f Gyroscope frame yaw inertia

k Wave number

k_l Power Take-Off spring constant

$\mathbf{L}$ Length Over All, the hull's maximum length

M_{ij} Body mass matrix

m_f Gyroscope's flywheel mass

p Fluid pressure

R_{xx} IOwec's roll radius of gyration

R_{yy} IOwec's pitch radius of gyration

R_{zz} IOwec's yaw radius of gyration

$Z_j(\omega)$ Response Amplitude Operator for the j^{th} degree of freedom

S_b Submerged body wetted surface

H_s Significant wave height

$S(\omega, \theta)$ Wave energy spectrum

S_{wp} Device's water plane area

T Wave period

T_d Hull's design draft (submergence)

T_p Peak wave period in a given spectrum

$\vec{v}$ Fluid velocity

VCG Vertical position of the center of gravity, measured from the undisturbed free surface, positive upwards

V_g Wave group velocity

v_n Normal velocity on the surface of the body. The normal vector points into the fluid

V_p Wave phase velocity

X_i Wave excitation force, usually a combination of incident (Froude-Krylov) and diffraction pressure

Greek letters

Δ Device's displaced mass at the design draft

η Wave elevation

λ Wave length

ω Wave radian frequency

ϵ_f Force signal phase

ϵ_m Motion signal phase

Ψ Total disturbance velocity potential of the Boundary Value Problem

ϕ Velocity potential of the fluid

Φ Basis flow potential. One of the three components of the total disturbance potential

ϕ_D Diffracted wave potential

φ Flywheel spin rotation

ϕ_I Incident wave potential

ϕ_l Local flow potential. One of the three components of the total disturbance potential

ϕ_R Radiated wave potential

ϕ_S Scattered wave potential

ψ Wave flow potential. One of the three components of the total disturbance potential

ρ Fluid density

σ Gyroscope pitch rotation

θ Gyroscope roll rotation

ξ_j Body displacement for the j^{th} degree of freedom due to wave excitation

$\dot{\xi}_j$ Body velocity for the j^{th} degree of freedom due to wave excitation

$\ddot{\xi}_j$ Body acceleration for the j^{th} degree of freedom due to wave excitation

ζ Gyroscope yaw rotation

Chapter 1

Introduction

In December 2015, the 21st Conference of Parties (COP21) gathered in Paris to decide on goals for reduction of carbon-dioxide emissions and limit Global Warming. The accord achieved a major goal by limiting the average global warming to 2 degrees Celsius above pre-industrial temperatures, while striving for a limit of 1.5 degrees Celsius, if possible. This agreement has been well received by the media, since it was stipulated by a joint effort of countries which previously diverged on greenhouse gas emission controls such as India, China, United States and the European Union.

According to the International Energy Agency (IEA), the electric sector contributes with roughly two thirds of all the greenhouse gas emissions [17]. The world's energy generation major source is coal, accounting by 39% of all production, followed by gas, which accounts for 22%, while oil retains 5% of the share [18]. This is a scenario bound to change in the following years, especially with large scale adoption of renewable energy generation, which is receiving ever increasing attention from both the United Stated and the European Union, which included multilateral agreements on development and deployment of renewable technology through the IEA.

Another important player in the shift of a dominant fossil fuel energy generation to a renewable one is the rising in gas and oil prices in the following years. According to the projections of the 2015 Annual Energy Outlook (AEO), prices of crude oil and natural gas are expected to rise. Particularly for latter, even in the most conservative scenario, prices should double by 2040. The rise of oil and gas prices depends on assumptions such as resource availability and growth in demand, especially in countries not in the Organization for Economic Co-operation and development [19]. Regarding energy consumption in the US the AEO states the following:

"Although projections see a modest growth in US energy consumption, the rising long-term natural gas prices, the high capital costs of new coal and nuclear generation capacity, state-level policies, and cost reductions for renewable generation in a market characterized by relatively slow electricity demand growth favor increased use of renewables."

1.1 The Wave Energy Resource

Wave energy is receiving increased attention and (governmental) support as a promising renewable resource to replace part of the global energy supply [1]. However, wave power conversion is still based on less mature technology compared to other renewable source converters. Available wave power is enormous with a density of about 2-3 kW/m^2 [1]. Other benefits include the larger percentage of time in which continuous capacity of energy production by Wave Energy Converters (WEC) is available over a year (versus 20–30% of wind and solar devices) [20], the easier predictive capability for wave climates than for winds and solar radiation [21] and better correlation between resource and demand (about 3 billion people in the world live in coastal areas) [1].

Figure 1-1 shows the available energy per meter of wave front in different areas of the ocean, averaged over one year time (results obtained over an observation period of 10 years, from satellite, spot measurements and visual observations). As can be noticed, the most energetic areas of the oceans are in the south hemisphere ($40^{\underline{o}}$-$60^{\underline{o}}$ S), but also between $40^{\underline{o}}$ and $60^{\underline{o}}$ N both on the Pacific and in the Atlantic sides, the energy density is quite relevant. Seasonal variations are in general considerably larger in the northern than in the southern hemisphere, which makes the south coasts of South America, Africa and Australia particularly attractive for exploitation [1].

Several different Wave Energy Converters (WEC) designs have been introduced

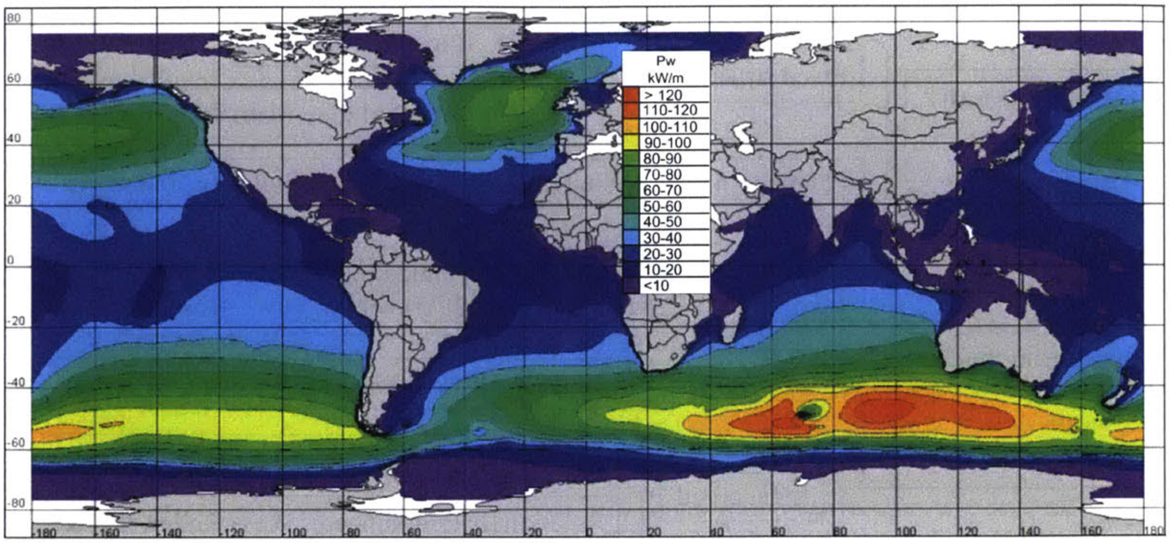

Figure 1-1: Global annual mean wave power estimation in kW/m spanning 10 years period [1].

throughout the years, with very distinct working principles. While most are dedicated devices operating offshore, some onshore solutions have been proposed. However, the mean wave energy decays rapidly when the measurement point gets close to the coast, be it due to wave breaking, bottom friction, diffraction or refraction. Therefore, it is expected that the greatest opportunity for wave energy extraction is not on the coast, but rather offshore, in deeper waters of the order of several hundreds of meters.

1.2 Outlook of Current Wave Energy Converters

Technological developments and studies on WECs have flourished over the last three decades. It is usual to classify the different types of WECs on the basis of the physical principle utilized for the generation of electrical energy, as it is done in the schematic diagram of Figure 2. Among the various types of WECs, which comprise concepts which made to prototype stage, few are designed to operate offshore. Most of them, like those based on the oscillating water columns (OWC) or on overtopping waves, need to be installed into rigid maritime structures directly on the coastal line or at a short distance from it. The so called onshore or near-shore devices necessarily suffer from an energy decay due to hydrodynamic transformation processes that affect waves

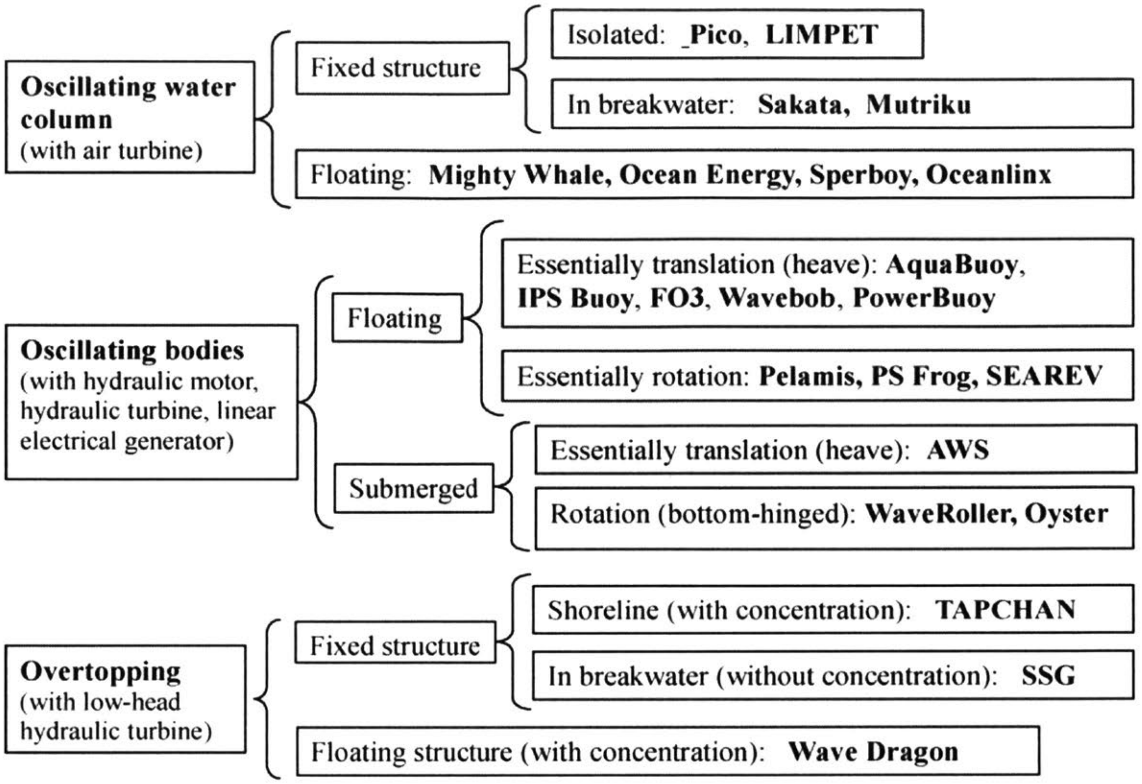

Figure 1-2: Classification of WECs per working principle [2].

propagating from offshore (where the sea bottom proximity effects are negligible) to near-shore areas, where the shallow water effects drastically reduce the available transported energy by the waves.

Salter summarizes the WEC design challenge very well: "The essential problem is finding a method to convert dispersed, random, alternating forces into concentrated, direct force, using a mechanism which is efficient at low levels and yet robust enough to withstand the worst conditions" [22]

The European Marine Energy Centre provides a very illustrative collection of animations of different WECs [23], complementing Figure 1-2. In the following sections we will take a look on these ideas and how they operate. This will later lead to the Inertial Ocean Wave Energy Converter (IOwec), the case study of this thesis, which could be classified as an oscillating body.

1.2.1 Oscillating Water Column

Modern wave energy research started with Yoshio Masuda's studies on Oscillating Water Columns (OWC) [2]. One of the first wave converters invented, the OWC works by trapping air inside a chamber sitting on the water surface. As the surface oscillates due to waves, the air is pushed in and out of the chamber. By placing a turbine inside the air intake/outtake, electric energy is generated by the turbine's torque (Figure 1-3a). Masuda's first creation in this sense was a navigation buoys whose lights were powered by an OWC [2].

To simplify the energy conversion problem, a Wells turbine is traditionally used in OWCs (Fig. 1-3b). This particular turbine rotates in the same way, regardless of the airflow direction. This is necessary, since the air flows in both directions from the chamber, depending whether a wave crest or trough is passing through the structure [4].

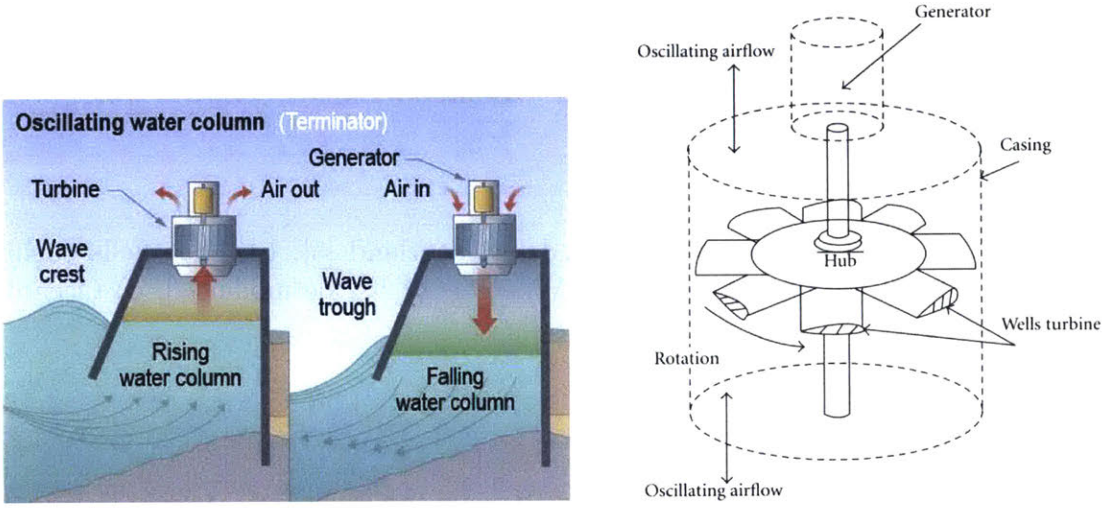

(a) (b)

Figure 1-3: a) Illustration of the OWC working principle [3]; b) The Wells turbine, commonly used in OWCs [4].

Still inside the spectrum of OWCs we have onshore (Fig. 1-3a) and offshore structures. The former, being located inland, is easier and cheaper to build, but suffers from the aforementioned bottom effects. Examples of onshore OWCs are the 500kW LIMPET, built in Islay, Scotland and the 400kW PICO, built in the Azores

Islands [24]. Examples of offshore OWCs are the Mighty Whale [7, 25] (Figure 1-4c) and 1MW greenWAVE from Oceanlinx (Figure 1-4d).

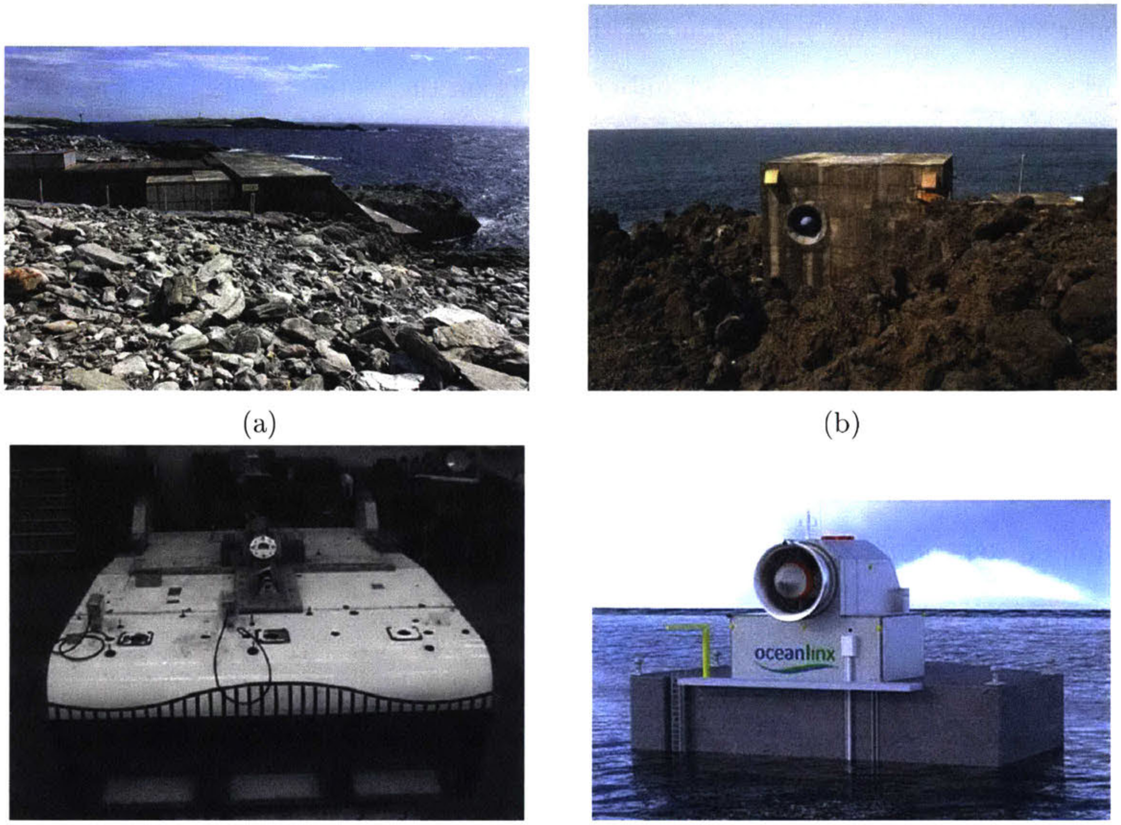

(a) (b)

(c) (d)

Figure 1-4: a) LIMPET power plant in Islay, Scotland [5]; b) The Wells turbine, commonly used in OWCs [6]; c) Mighty Whale 1/20th scale model [7]; d) Oceanlinx greenWAVE plant.

1.2.2 Oscillating Bodies

Oscillating bodies in waves are, by far, the most used concept for wave energy converters. A myriad of designs have been proposed, ranging from simple buoys oscillating in heave driving a generator, to carpet-like structures positioned underwater [22, 26, 27, 28, 29, 30]. Designers tend to focus on extracting energy from one degree of freedom of the longitudinal diametral plane, usually heave or pitch. The Norwegian wave buoy is a typical example of single body heaving devices, which utilizes the relative motion of a floating unit against a pole hinged at the bottom of the sea to generate electricity [26, 31] (Fig. 1-5a). This design is also categorized as a point-absorber, meaning its characteristic length is much smaller than the predominant wave length. A 200MW power station composed by an array of 410 of such buoys is also envisioned. Unfortunately, however, at the publication date, this station was not economically competitive, mainly due to high labor costs [26].

Another interesting point absorber was WaveBob, a device consisting of two heaving bodies with different inertia and restoring characteristics (Fig. 1-5b). Energy was converted by a Power-Take Off (PTO) from the relative motion between two buoys [28]. In 2013 WaveBob Ltd. failed to raise the necessary funds to continue its operations and had to liquidate its assets [32].

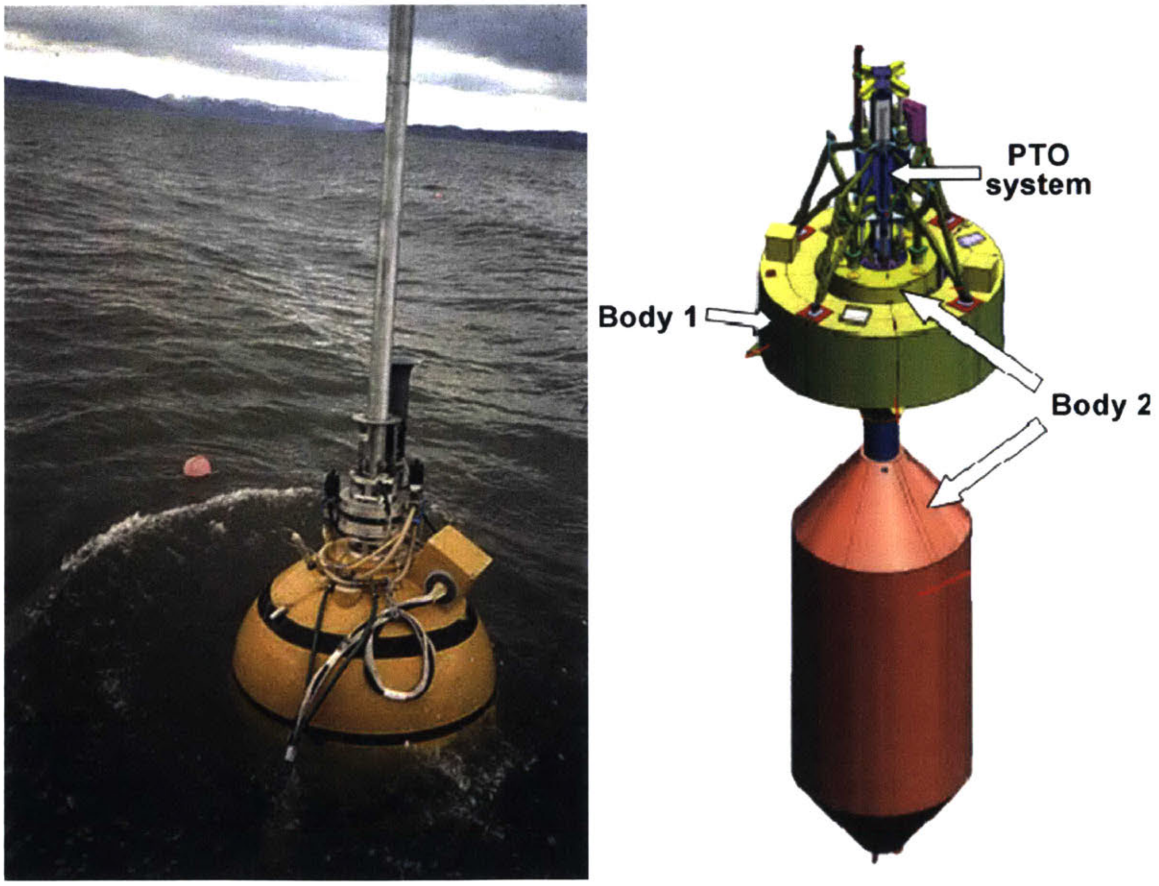

(a) (b)

Figure 1-5: a) Norwegian wave buoy [2]; b) Wavebob [2].

WECs utilizing body angular motion (e.g. pitch) for energy extraction have found a more consistent success. Salter's famous Nature article on his rotating double cylinder-like body first focused the attention on these kind of designs, inspiring modern converters [22]. The design, later called Duck, uses gyroscopes inside its smaller cylinder, extracting energy from the torque produced by the gyroscopes when the body oscillates (Fig. 1-6a).

An effective recent development is the Pelamis, an attenuator-type WEC (i.e. characteristic length of a few wave lengths). It is composed of four long cylinders connected by hinged joints on the extremities. A hydraulic PTO inside such hinges is actuated by the relative motion of the bodies. Three Pelamis are currently operational on the coast of Portugal, delivering 750kW each [2].

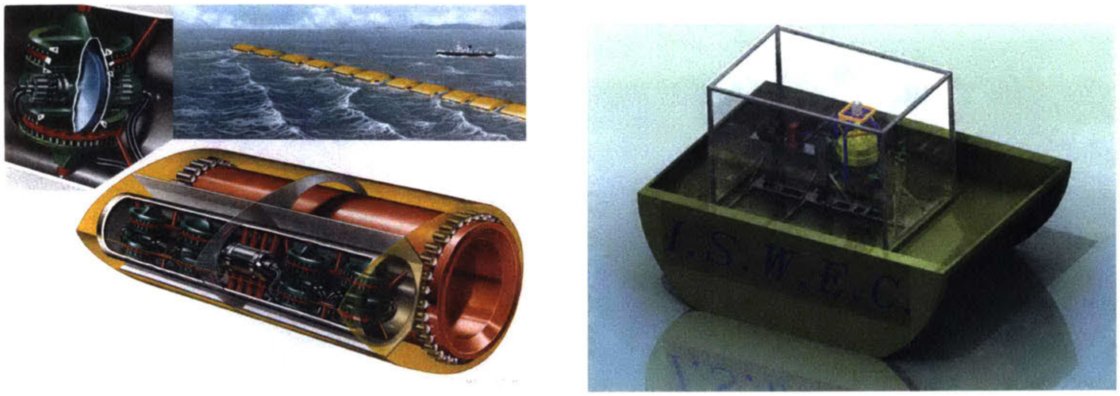

(a) (b)

Figure 1-6: a) Artist impression of Salter's Duck [8]; b) ISWEC $1/8^{th}$ scale model [9].

The WEC technology which this thesis focuses on is a second generation of the Inertial Sea Wave Energy Converter (ISWEC), a device inspired by Salter's idea. The ISWEC, developed at the Politecnico de Torino, is an oscillating body with a gyroscope inside. As the hull pitches it induces a roll of the spinning flywheel and, by placing a PTO on the roll axis, energy can be extracted (Fig. 1-6b). The uniqueness of this proposal lies in the fact the entire mechanical system is isolated from sea water, lowering corrosion and drastically reducing maintenance costs. Early scale model tests indicated a rating of about 300kW for a $34m$ device [9].

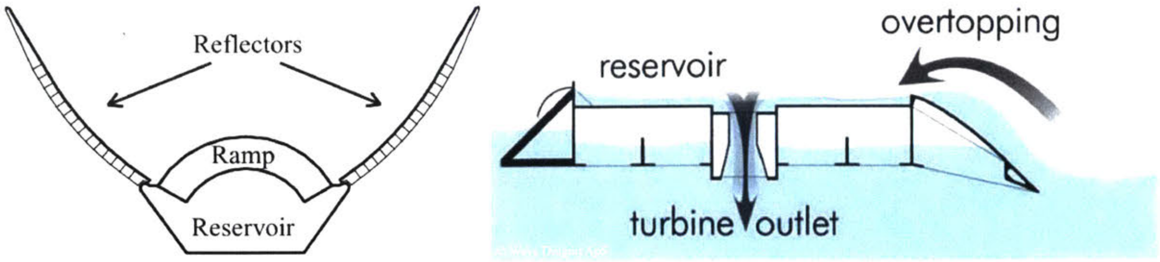

Figure 1-7: Wave Dragon working principle [10].

1.2.3 Overtopping

Overtopping devices have a very peculiar way of operating. While OWCs and oscillating bodies use, in their own way, motion induced by the waves, this technology doesn't. It works by capturing water close to the wave crest on a pool sitting above sea-level and driving such stored water through a low-head hydraulic turbine [2]. The main advantage of this technology is the capability of storing energy in form of a potential, driving it through the PTO when convenient. One of the most famous projects is the Wave Dragon, which uses wave deflectors to direct and concentrate waves until they reach and spill into the reservoir (Fig.1-7). The designers expect a rating of 4-10MW of energy for the full scale Wave Dragon [10].

Chapter 2

Dynamics in Waves for WEC Design

The most common ocean gravity waves are formed by wind action over the free-surface. The process can be better understood by idealizing the effects of wind blowing with constant speed over a surface at rest. At first the driving force will be friction, with the existence of a boundary-layer on the surface. This friction creates short (capillary) waves of high frequency. If the wind was to suddenly stop, this waves would quickly decay due to viscous effects [11].

As the wind becomes stronger the capillary waves grow large enough to be greatly affected by Bernoulli effects. Crests now start being pulled upwards due to a local increase of wind speed over it, which corresponds to a local pressure decrease (much like a foil), while also being propelled forward due to separation. The wave grows larger and faster up to the point when its speed equals the wind speed. Therefore, larger sea states are due to stronger winds acting on large fetches [11].

The mechanics of progressive waves on the ocean surface is well described by ideal fluid effects. The following section summarizes the derivation of some relevant formulae concerning free surface waves that will be widely used for the analysis in the next sections. Further details can be found in classical text books [12, 33, 34].

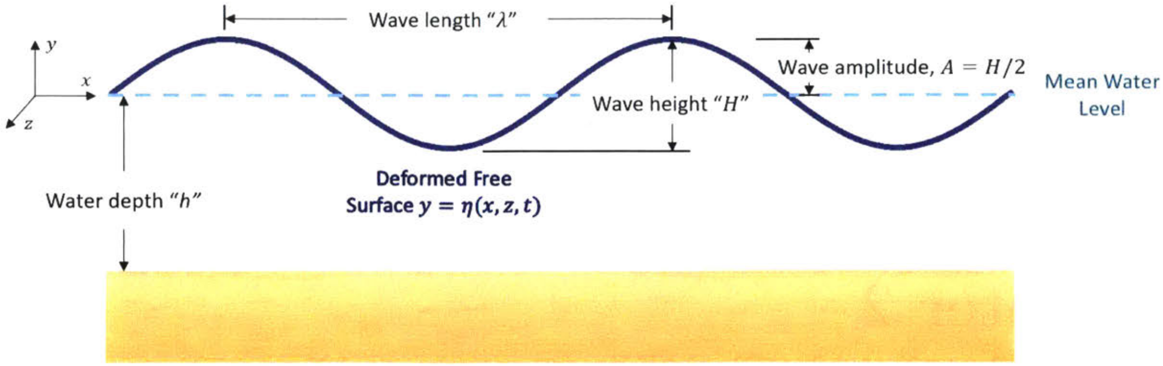

Figure 2-1: Monochromatic wave diagram.

2.1 Linear (Airy) Wave Theory

Assuming inviscid ($\nu = 0$), incompressible ($\nabla \cdot \vec{v} = 0$) and irrotational ($\nabla \times \vec{v} = 0$) fluid flow, there exists a potential function for which,

$$\vec{v} = \nabla \phi \tag{2.1}$$

The continuity equation, which express mass conservation, becomes a Laplace equation.

$$\nabla^2 \phi \equiv \frac{\partial^2 \phi}{\partial x^2} + \frac{\partial^2 \phi}{\partial y^2} + \frac{\partial^2 \phi}{\partial z^2} = 0 \tag{2.2}$$

Thanks to equation 2.2, the velocity potential and pressure are decoupled. The latter can be calculated through the unsteady Bernoulli equation, a statement of conservation of momentum for potential flow.

$$p = -\rho \left[\frac{\partial \phi}{\partial t} + \frac{1}{2} |\nabla \phi|^2 + gy \right] + F(t) \tag{2.3}$$

In the potential flow framework just introduced, we define the equation of linear free surface progressive waves (Fig. 2-1). We assume the wave slope is small (i.e. $A/\lambda \ll 1$) and, by keeping only linear terms in ϕ and η, we can write the kinematic and dynamic boundary conditions (BC) as per Table 2.1.

A single free surface BC can be written by taking the time derivative of the

Table 2.1: Boundary Value Problem (BVP) for Airy waves in finite and infinite depth

Boundary Condition	**Finite depth** $(-h < y < 0)$	**Infinite depth** $(h \to \infty)$
Body Kinematic	$\frac{\partial \phi}{\partial y} = 0$ at $y = -h$	$\nabla \phi \to 0$ as $y \to -\infty$
Free Surface Kinematic	$\frac{\partial \phi}{\partial y} = \frac{\partial \eta}{\partial t} = 0$	
Free Surface Dynamic	$\frac{\partial \phi}{\partial t} + g\eta = 0$	

dynamic BC stated in table 2.1,

$$\frac{\partial^2 \phi}{\partial t^2} + g\frac{\partial \eta}{\partial t} = 0 \tag{2.4}$$

and replacing $\frac{\partial \eta}{\partial t}$ by $\frac{\partial \phi}{\partial y}$, as given by the kinematic BC of table 2.1,

$$\frac{\partial^2 \phi}{\partial t^2} + g\frac{\partial \phi}{\partial y} = 0 \tag{2.5}$$

The plane progressive wave is a solution to equation 2.2. It is a 2D sinusoidal propagation of frequency $\omega = 2\pi/T$ and phase velocity V_p. The elevation and potential can be written (assuming no phase angle), respectively,

$$\eta(x,t) = A\cos(kx - \omega t) \tag{2.6}$$

$$\phi_I(x,y,t) = \frac{gA}{\omega}e^{ky}\sin(kx - \omega t) \tag{2.7}$$

The wavenumber is defined as $k = 2\pi/\lambda$ and the phase velocity $V_p = \omega/k$. By substituting equation 2.7 in the free surface BC (Eq. 2.5) we get the dispersion relation.

$$\omega^2 = gk\tanh(kh) \tag{2.8}$$

In deep waters, i.e. $h \to \infty$, equation 2.8 reduces to $\omega^2 = gk = \frac{g}{2\pi}T^2$. One great advantage of linearizing the wave problem is the possibility of representing any complicated wave pattern as a superposition of monochromatic waves of different heading, frequency and amplitude [11] (Fig. 2-2). The wave elevation, dependent on wave direction θ and frequency ω, becomes,

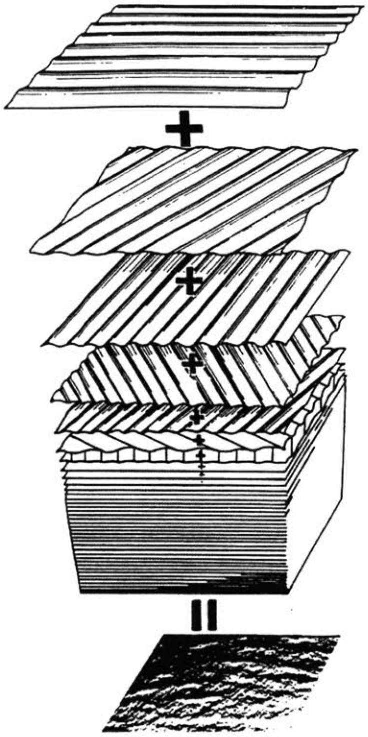

Figure 2-2: Complicated sea state as a superposition of different monochromatic waves [11].

$$\eta(x,z,t) = Re\left[\int_0^{\infty} d\omega \int_0^{2\pi} d\theta A(\omega,\theta) e^{-ik(\omega)(x\cos\theta + z\sin\theta) + i\omega t\dagger}\right] \tag{2.9}$$

The superposition of monochromatic waves of nearly equal wave length and direction results in a wave group. The individual waves travel at phase speed, while the entire group travels with a group velocity V_g, which can be written as,

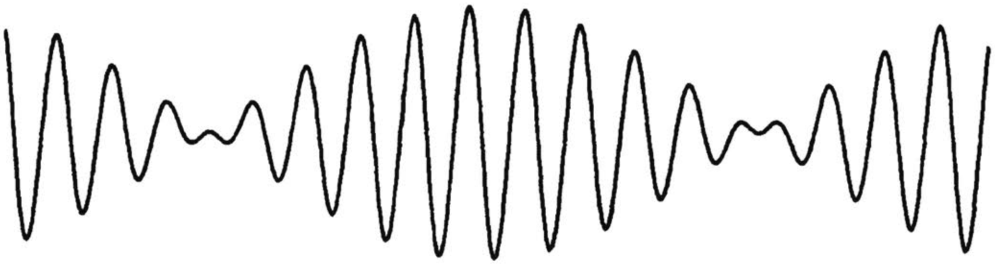

Figure 2-3: A wave group, resulting from the superposition of two similar monochromatic waves [12].

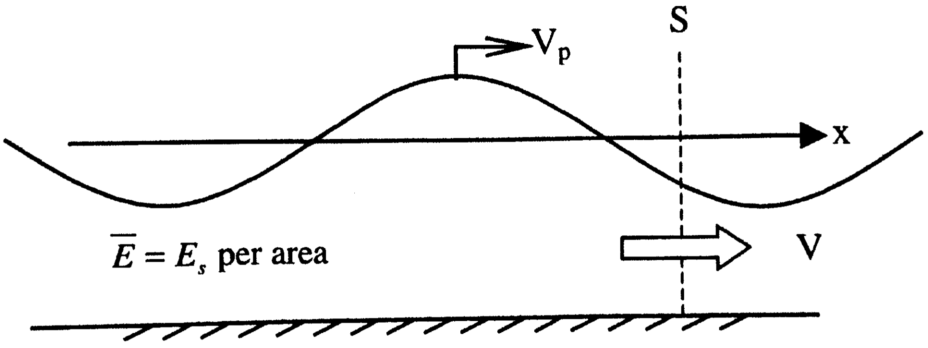

Figure 2-4: A wave group flowing through a control volume $\mathcal{V}$ with inlet surface S.

$$V_g = \left(\frac{1}{2} + \frac{kh}{\sinh 2kh}\right) V_p \tag{2.10}$$

The total energy in a wave is the summation of the kinetic and potential components. Integrating such summation along the depth yields the energy density E per unit area of the mean free surface [12],

$$E = \rho \int_{-h}^{\eta} \left(\frac{1}{2}|\vec{v}|^2 + gy\right) dy = \frac{1}{4}\rho g A^2 + \frac{1}{2}\rho g A^2 \cos(kx - \omega t) \tag{2.11}$$

Averaging equation 2.11 over one wave period allows a better estimate of the energetic content of a wave.

$$\overline{E} = \frac{1}{2}\rho g A^2 \tag{2.12}$$

Wave energy propagates with the group velocity V_g. This can be seen by calculating the energy flux $\mathfrak{F}$ across a control volume $\mathcal{V}$ as per Fig. 2-4. The flux averaged over one wave period,

$$\frac{d\overline{E}}{dt} = \overline{\mathfrak{F}} = \left(\frac{1}{2}\rho g A^2\right)\left(\frac{\omega}{k}\right)\left(\frac{1}{2} + \frac{kh}{\sinh 2kh}\right) = \overline{E}V_g \tag{2.13}$$

Falnes rewrites equation 2.13 by considering deep water (i.e. $k = \omega^2/g$) and knowing that the wave height is twice the amplitude [34]. The transported wave power per unit width of wave front becomes,

$$\frac{d\overline{E}}{dt} = \overline{\mathfrak{F}} = \frac{\rho g^2}{32\pi} T H^2 \tag{2.14}$$

2.2 Irregular Ocean Waves

Waves in the ocean are dispersive and random. This environment is usually treated stochastically by considering the superposition described previously (Fig. 2-2). Traditionally, ocean waves are assumed to be *ergodic*, i.e. a stationary random process fully characterized by one ensemble, a simplification which allows the derivation of all statistics from only one set of data [35]. The total free surface deformation can be written as a summation of equation 2.6,

$$\eta(\vec{x}, t) = \sum_{i=1}^{n} X_i(t) = \sum_{i=1}^{n} A_i \left(k_i \vec{x} - \omega_i t + \epsilon_i \right) \tag{2.15}$$

Where ϵ is the phase of the component. Usually $X_i(t)$ does not possess a Fourier transform (i.e. the Fourier integral does not converge). To overcome this the wave signal is truncated after some periods [35],

$$X_T^i(t) = \begin{cases} X^i(t), & \text{if } -T/2 < t < T/2 \\ 0, & \text{otherwise} \end{cases} \tag{2.16}$$

The Fourier transform of the truncation above is,

$$G_T^i(\omega) = \frac{1}{2\pi} \int_{-\infty}^{\infty} X_T^i(t) e^{-i\omega t} dt \tag{2.17}$$

It can be shown that the mean square of $X_T^i(t)$ over the range T is [35],

$$\langle (X^i(t))^2 \rangle = \int_{-\infty}^{\infty} \lim_{T \to \infty} \left[\frac{2\pi}{T} |G_T(\omega)|^2 \right] = \int_{-\infty}^{\infty} S_{xx}(\omega) d\omega \tag{2.18}$$

Where S_{xx} is defined as the mean square spectral density, and is a real and even function of ω. The auto-correlation function of $X_T^i(t)$ is [35],

$$R_T^i(\tau) = \frac{1}{T}\int_{-T/2}^{T/2} X_T^i(t)X_T^i(t+\tau)dt \tag{2.19}$$

The auto-correlation and spectral density are related by Fourier transform through the known Wiener-Khintchine relation [35],

$$\begin{aligned} S_{xx}(\omega) &= \frac{1}{2\pi}\int_{-\infty}^{\infty} R_{xx}(\tau)e^{-i\omega t}d\tau \\ R_{xx}(\tau) &= \int_{-\infty}^{\infty} S_{xx}(\omega)e^{i\omega t}d\omega \end{aligned} \tag{2.20}$$

Since both the auto-correlation and spectral density are real and even functions, the latter is rewritten as a one-sided spectrum [35],

$$R_{xx}(\tau) = \int_0^{\infty} 2S_{xx}(\omega)\cos(\omega\tau)d\omega = \int_0^{\infty} S_x(\omega)\cos(\omega\tau)d\omega \tag{2.21}$$

where,

$$S_x(\omega) = \begin{cases} 2S_{xx}(\omega), & \text{for } \omega \geq 0 \\ 0, & \text{otherwise} \end{cases} \tag{2.22}$$

This one-sided spectrum, being defined only for positive frequencies, is able to be measured experimentally. The relation in equation 2.20 has important ramifications. By making $\tau = 0$, the auto-correlation function in equation 2.19 yields the expected mean square value [35],

$$R_{xx}(0) = E\left[\eta^2(x,y,t)\right] = \lim_{T\to\infty}\frac{1}{T}\int_{-\infty}^{\infty}\eta^2(x,y,t)dt = \int_0^{\infty} S(\omega)d\omega \tag{2.23}$$

This means the process variance, which relates to the total energy in the system, is given by the area under the spectrum. Rewriting equation 2.11 to reflect the stochastic nature of the waves gives an even clearer relation between the total process energy and the spectral area,

$$E = \rho g E\left[\eta^2(x,y,t)\right] = \rho g \int_0^\infty S(\omega)d\omega \tag{2.24}$$

The significant wave height is a very important quantity. It is the 1/3 highest average wave height and is defined as four times the square-root of the zero moment of the spectrum,

$$H_s = 4\sqrt{\int_0^\infty S(\omega)d\omega} \tag{2.25}$$

The energy spectrum is usually described by semi-empirical relations such as the Bretschneider or JONSWAP (Joint North Sea Project) spectra [36, 37]. The latter is widely used in closed fetches and its equation can be seen below.

$$S(\omega) = \frac{\alpha g^2}{\omega^5} e^{-\beta\gamma^r\left(\frac{\omega_p}{\omega}\right)^4} \tag{2.26}$$

Where ω_p is the peak frequency and γ is the peak enhancement coefficient, which varies between 1 and 7 with mean of 3.3. β is usually taken as $\frac{5}{4}$. α and r model the intensity and peak of the spectrum, respectively,

$$\alpha = 5.061\left(\frac{\omega_p}{2\pi}\right)^4 {H_s}^2\left(1 - 0.287ln(\gamma)\right) \tag{2.27}$$

$$r = exp\left[-\frac{(\omega-\omega_p)^2}{2\omega_p^2\sigma^2}\right], \text{ with } \sigma = \begin{cases} 0.07, & \text{if } \omega \le \omega_p \\ 0.09, & \text{if } \omega > \omega_p \end{cases} \tag{2.28}$$

With the sea spectrum at hand, remembering the definition of the transported energy by each individual monochromatic wave component (eq. 2.13), the transported wave power per unit width of wave front can be written again, this time as a function of the significant wave height and energy period T_e.

$$\frac{d\overline{E}}{dt} = \overline{\mathfrak{F}} = \rho g \int_0^\infty S(\omega)V_g d\omega \simeq \frac{\rho g^2}{64\pi}{H_s}^2 T_e \tag{2.29}$$

2.3 Seakeeping in WEC Design

The design of WECs of the oscillating body type (Sec. 1.2.2) require the evaluation of the concept's motion in waves very early on. The objective is to tune the converter's natural frequency (be it translation, rotation or both) with the predominant wave period from the operating site spectrum. Traditionally, the solution of the equations of motion involves linearizing the problem (i.e. small wave amplitude and body motion compared to the device's nominal size) and solving them in Fourier domain, as done for ships [9, 38, 39, 40, 41, 42, 43, 44, 45]. The body response to a monochromatic wave, in frequency domain [12],

$$\sum_{j=1}^{6} \xi_j \left[-\omega^2 \left(M_{ij} + a_{ij} \right) + i\omega b_{ij} + c_{ij} \right] = A X_i \tag{2.30}$$

The determination of the added mass and damping coefficients and the wave exciting forces are calculated by solving the radiation potential (the scattering can be found through the Haskind relations from the radiation case [46]). The Boundary Value Problem is the same as in table 2.1, with the addition of the body BC.

$$\frac{\partial \phi}{\partial n} = v_n \tag{2.31}$$

The linearization of the motion allows the decomposition of the total fluid potential as a summation of the radiation and diffraction wave potentials. The latter is the superposition of incident and scattered waves [47].

$$\phi = \phi_R + \phi_D = \phi_R + \phi_I + \phi_S, \text{ where } \frac{\partial \phi_S}{\partial n} = 0 \tag{2.32}$$

The radiation potential models the waves generated by the moving body (with the same frequency as the incident wave) in calm water. It can be represented by the summation of each Degree of Freedom (DoF) displacement, subject to its own body BC [47].

$$\phi_R = i\omega \sum_{j=1}^{6} \xi_{jj}\phi_j \tag{2.33}$$

$$\frac{\partial \phi_j}{\partial n} = n_j \tag{2.34}$$

Where n_j is the normal vector $\vec{n}$ pointing out of the body and into the fluid for $j = 1, 2, 3$ and $\vec{x} \times \vec{n}$ for $j = 4, 5, 6$. The added-mass and damping come from the real and imaginary components of the radiation forces [47]. The exciting forces may be calculated straight from Haskind relations. All of these integral equations come from Green's theorem [48].

$$a_{ij} - (i/\omega)b_{ij} = \rho \iint_{S_b} \phi_j \frac{\partial \phi_i}{\partial n} dS \tag{2.35}$$

$$X_i = -i\omega\rho \iint_{S_b} \left(\frac{\partial \phi_i}{\partial n}\phi_I - \phi_i \frac{\partial \phi_I}{\partial n} \right) dS \tag{2.36}$$

Finding the velocity potential of this Boundary Value Problem means solving the integral equations derived through Green's theorem. WAMIT, an industry standard panel method code, presents the equation in the form below, solving it for discretized panels of the body wetted surface with center at $\vec{\xi'}$ [49].

$$2\pi\phi_j(\vec{x}) + \iint_{S_b} \phi_j(\vec{\xi'}) \frac{\partial G(\vec{\xi'}; \vec{x})}{\partial n_{\vec{\xi'}}} d\vec{\xi'} = \iint_{S_b} n_j G(\vec{\xi'}; \vec{x}) d\vec{\xi'} \tag{2.37}$$

$$\vec{\xi'} = \xi\hat{i} + \eta\hat{j} + \zeta\hat{k} \tag{2.38}$$

$$\vec{x} = x\hat{i} + y\hat{j} + z\hat{k} \tag{2.39}$$

The Green function $G(\vec{\xi'}; \vec{x})$ used by WAMIT is the wave source potential. It is the fluid potential at point $\vec{x}$ due to a point source of strength -4π at $\vec{\xi'}$ ($J_o(x)$ is the zero order Bessel function)[49].

$$G(\vec{x}; \vec{\xi'}) = \frac{1}{r} + \frac{1}{r''} + 2\int_0^\infty dk \frac{(k+K)\cosh k(z+h)\cosh k(\zeta+h)}{k\sinh kh - K\cosh kh} e^{-kh} J_o(kR) \tag{2.40}$$

$$r^2 = (x-\xi)^2 + (y-\eta)^2 + (z-\zeta)^2 \tag{2.41}$$

$$r''^2 = (x-\xi)^2 + (y-\eta)^2 + (z+\zeta+h)^2 \tag{2.42}$$

With the computation of the hydrodynamic coefficients of equation 2.30 from the solution of the BVP (equation 2.37), the transfer function, or Response Amplitude Operator (RAO), can be calculated. It is the response, in frequency domain, to a monochromatic wave of frequency ω and amplitude A [12].

$$Z_j(\omega) = \frac{\xi_j}{A} = \frac{X_i}{(M_{ij}+a_{ij}) + i\omega b_{ij} + c_{ij}} \tag{2.43}$$

The response of the body to a given sea state $S(\omega)$ can be calculated through a simple multiplication. This justifies the work in frequency domain, as time domain would require the evaluation of a convolution integral for the same purpose.

$$S_\xi(\omega) = S(\omega)|Z_j(\omega)|^2 \tag{2.44}$$

Cummins developed general equations of motion in time domain which are the primary tools used by engineers and designers to bridge frequency (evaluated by solving the BVP) and time domain quantities [50]. These equations are based on impulsive motion, by decomposing the flow around the body into two components, one due to an impulsive displacement on the body and another representing the decaying wave motion generated by such displacement. For a body translating on the water surface, the equation of motion becomes:

$$\sum_{i=1}^{6}\left[\left(M_{ij}+a^o_{ij}\right)\ddot{\xi}_j + b^o_{ij}\dot{\xi}_j + c_{ij}\xi_j + \int_{-\infty}^{t} K_{ij}(t-\tau)\dot{\xi}_j(\tau)d\tau\right] = f_k(t) \tag{2.45}$$

The kernel of the convolution integral is related to the frequency dependent quantities through Fourier transform [50, 51, 52]. It tells us how the radiation forces keeps influencing the body's motion for some time (i.e. fluid memory effects).

$$a_{ij}(\omega) = a_{ij}^{o} - \frac{1}{\omega}\int_{0}^{\infty} K(t)\sin(\omega t) \tag{2.46}$$

$$a_{ij}^{o} = \lim_{\omega \to \infty} a_{ij}(\omega) \tag{2.47}$$

$$b_{ij}(\omega) = \int_{0}^{\infty} K(t)\cos(\omega t) d\omega \tag{2.48}$$

$$K_{ij}(\tau) = \frac{2}{\pi}\int_{0}^{\infty} b_{ij}(\omega)\cos(\omega t) d\omega \tag{2.49}$$

Equations 2.45 is widely used, together with frequency domain panel methods (e.g. WAMIT [49]), to describe the motion of WECs in time domain. This is a very powerful and accurate approach for most bodies, yielding results with a very small computational effort. However, the description of the problem through Fourier transform makes it impossible to incorporate nonlinear effects into these models. Recent developments on panel methods have been focusing on solving the equations of motion directly, in time domain, introducing the possibility of extension to some nonlinearities. Kring tackled this problem, developing a time domain Rankine panel method, capable of solving both the body and free surface motions directly [14]. This work was further developed by himself, leading to the Boundary Element Method (BEM) code Aegir, capable of importing non-uniform basic spline surfaces of arbitrary bodies, discretize them and solve for the motions.

Aegir will be used in this work to study the converter presented in chapter 3. This particular WEC utilizes gyroscopes to extract energy from the hull motion. To model this, the state-space vector and external forces calculated by Aegir at every time-step will have to be corrected to account for the spinning flywheel dynamics. The change in angular momentum of the gyroscope will induce torques in all 3 directions, coupling all the rotation Degrees of Freedom (DoF). The corrections and time marching were implemented in a MATLAB code, which constantly shares information with Aegir through TCP/IP protocol.

Chapter 3

The Inertial Ocean Wave Energy Converter (IOwec)

The Inertial Ocean Wave Energy Converter (IOwec) is the case study of this thesis. It is an evolution of the ISWEC described in chapter 1.2.2 [1], meaning it also relies on gyroscopic mechanisms for power extraction. This concept was developed and first presented as a contender in the Department of Energy Wave Energy Prize (WEP) [53].

The first task was to determine the operation site. Since the reference wave climate announced by the WEP would be representative of the American west coast, the Oregon sea was chosen, due to its high energy content throughout the year (Fig. 1-1). Figure 3-1 presents the statistical description of the Oregon sea, showing $T_p = 8s$ as the most probable wave period [13]. A more comprehensive table is also presented in appendix B.

3.1 Hull Design and Internal Arrangement

The hull was sized by University of Torino researchers, with input from Dr. Stefano Brizzolara. It can be interpreted as an evolution of the ISWEC's old shape by intro-

---

[1] The ISWEC was initially designed to work in the open sea, like the Atlantic or Pacific oceans, instead than closed sea like the Mediterranean

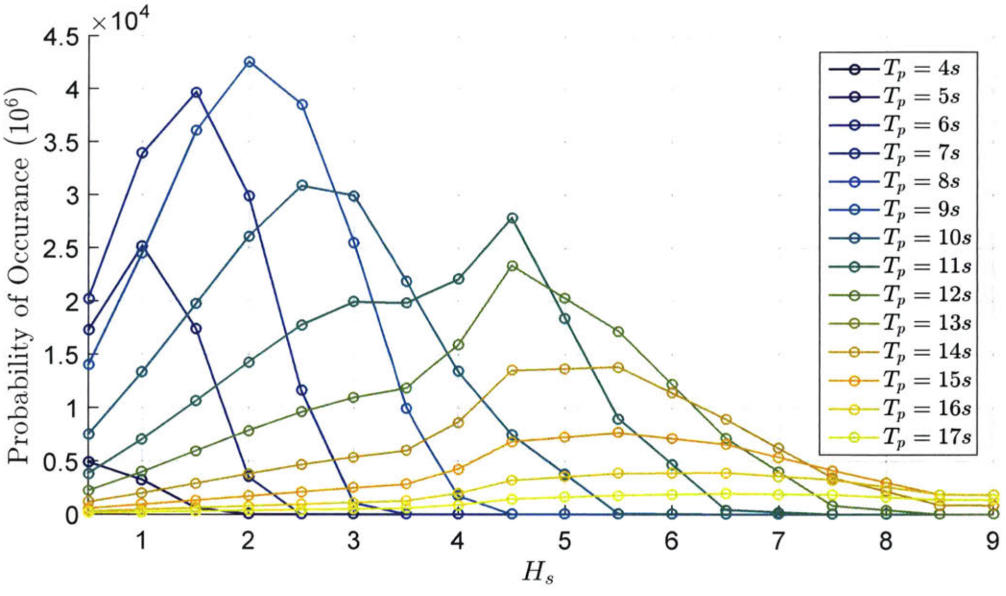

Figure 3-1: Probability of occurrence of a given H_s and T_p [13].

ducing a tapered top and sides, with the ultimate scope of increasing the resonance period of the ISWEC up to typical prevalent periods of open oceans. In fact, a narrower waterline beam at the extreme bow and stern means a reduction of the inertia moment, which in turn implies a reduction of the longitudinal metacentric height and an increase of natural resonance period (Eq. 3.1) [33]. Figures 3-2a and 3-2b show the evolution, from the ISWEC to the IOwec shape.

$$c_{55} = \rho g V \left(z_B - VCG\right) + \rho g \iint_{S_{wp}} x^2 dS = \rho g V \overline{GM}_L \tag{3.1}$$

Inside the hull we find two main components, the gyroscope housing and the U-Tanks (fig. 3-3a). The latter design and analysis will be addressed in Appendix A. The former is self explanatory, housing the flywheels and power take-off systems. It also provides a very low pressure atmosphere inside to minimize air friction (i.e. energy losses) on the flywheels, which are detrimental to maintain the spin. This chamber was also envisioned in a modular manner, such that, in case of failure of one of the components inside or loss of vacuum, the housing can be removed by a supply vessel and transported onshore for repairs (fig. 3-3b). This procedure leaves the hull in free floating condition, ready to receive a spare modulus or to wait for the

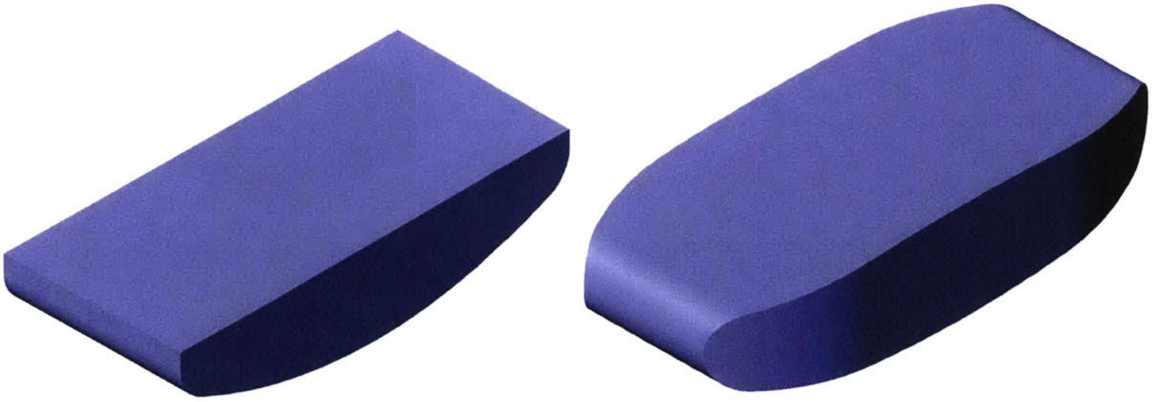
(a) (b)

Figure 3-2: a) ISWEC hull, with its taper from bottom to top; b) IOwec hull, with additional tapper at the stern and bow.

old one, which saves the unnecessary trouble of disconnecting the entire body from the mooring lines.

A great advantage of the IOwec is evident from the choice of an isolated gyroscope housing. It avoids contact of all the moving parts and mechanisms of the device with salt water, which greatly impedes the corrosion process. This guarantees very low maintenance costs, specially when compared to devices with open moving parts (e.g. WaveBob, fig. 1-5b). This isolation, as well as a welded construction of the hull with bolted hatches designed to resist to high outside pressures, creates the possibility of completely submerging the body in case of severe storm forecast, mitigating damage to the mooring lines and the hull. This is achievable thanks to the isolation of the mechanisms from the sea. This "survival mode" mitigates many risks typically associated with WEC technologies.

Figure 3-4 shows the pitch and heave RAOs generated by WAMIT for such values. It is interesting to notice how the natural period matches the desired $8s$ value. The two transfer functions are normalized as follows,

$$Z_3(\omega) = \frac{\Xi_3}{A} \tag{3.2}$$

$$Z_5(\omega) = \frac{\Xi_5}{kA} \tag{3.3}$$

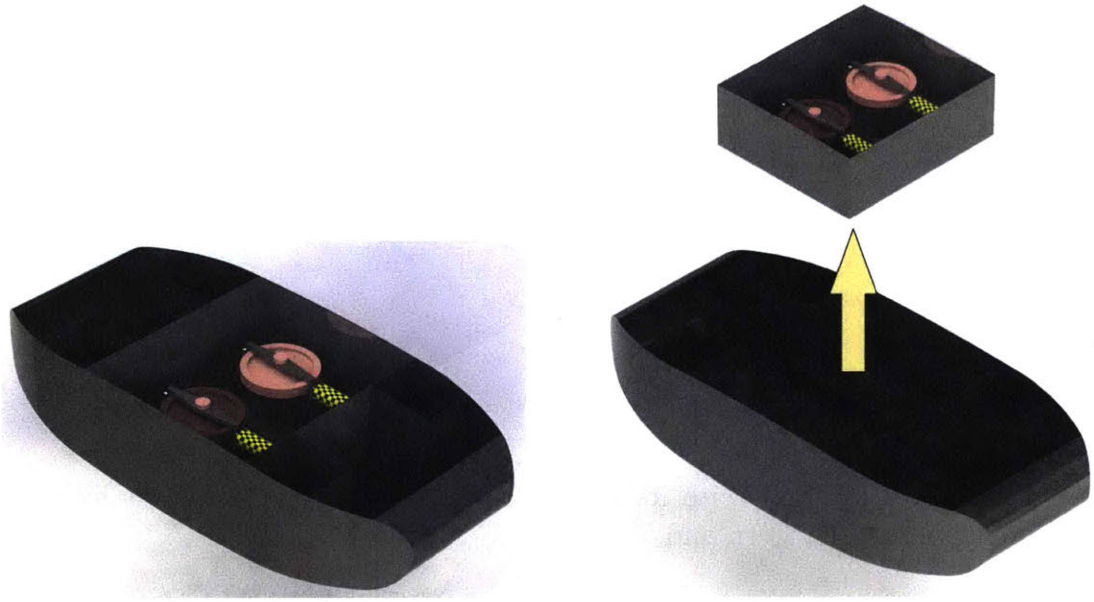

(a) (b)

Figure 3-3: a) IOwec internal arrangement; b) IOwec modular design, the gyroscope housing may be removed if repairs are needed.

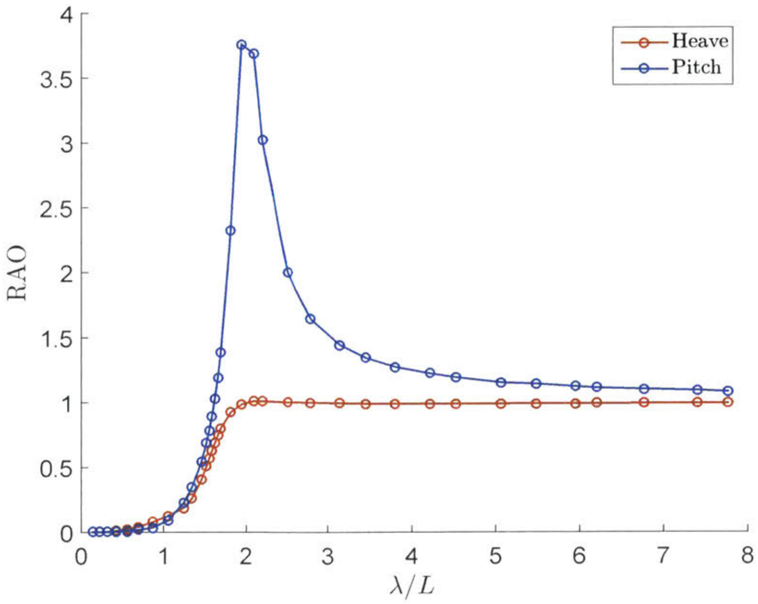

Figure 3-4: Heave and pitch RAO versus wave period.

Table 3.1 presents the design characteristics of the IOwec, which will be used for all subsequent studies. A preliminary structural design was also performed to clarify the hull's subdivision and bare weight. This was performed by a combination of the ABS Rules for Building and Classing for Barges [54] and for Steel Vessels [55], both considering unrestricted navigation. The former was utilized to find the minimum thickness of the deck, bottom, side and bulkheads plating, while the latter was used to determine the required Section Modulus of the reinforcements, their minimum thickness and, consequently, their minimum size. The bottom structures of the gyroscope compartment were dimensioned with the equations valid for machinery spaces, this was done to account for the considerable bending moments exerted by the gyroscopes on the IOwec structure.

Table 3.1: IOwec Main Dimensions.

Dimension	**Value**	**Unit**
L	45	m
B	20	m
D	10	m
T_d	7	m
VCG	-1.485	m
Δ	5217.87	ton
R_{xx}	8.45	m
R_{yy}	14.65	m
R_{zz}	3.84	m

Following the rules, the spacing between Primary (e.g. girders) and Secondary Structural Members (e.g. longitudinals) are, respectively, $2500mm$ and $500mm$ [55]. Both are reduced by half beneath the gyroscope housing. Figure 3-5 shows the midship cross section, with all reinforcements at the right scale. Table 3.2 summarizes the contribution of each individual element.

The final mass of the steel structure must account for the existence of brackets, bars and other members not considered before. Therefore, 2% more mass will be added for extra elements and another 3% for general allowance. This yields a total of $544.89t$ of structural mass alone. The IOwec has $4672.98t$ of extra displaced mass to accommodate the PTO and gyroscopes.

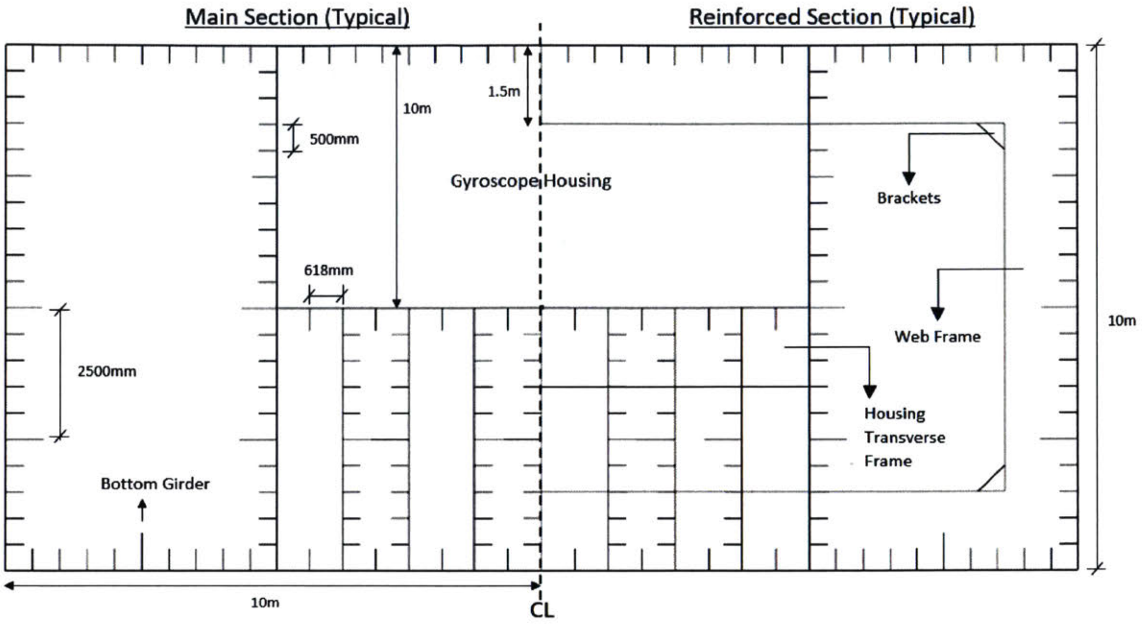

Figure 3-5: IOwec midship cross section.

Table 3.2: Hull structure components discretization and weight contribution

Element	Area	Thickness	Volume	Mass	Group
[-]	[m²]	[mm]	[m³]	[ton]	[-]
Deck	900.00	7.00	6.30	49.46	Plating
Sides	734.57	7.00	5.14	40.36	
Bottom	1094.18	7.00	7.66	60.13	
Bulkheads	801.86	5.50	4.41	34.62	
U-tanks	482.86	5.50	2.66	20.85	
Gyro Housing	500.00	5.50	2.75	21.59	
Bottom Girder	463.73	7.50	3.48	27.30	Primary Support Members
Deck Girder	67.31	4.50	0.30	2.38	
Side Girder	142.70	4.50	0.64	5.04	
Bulkhead Girder	288.27	4.50	1.30	10.18	
Bottom Longitudinals	924.32	4.50	4.16	32.65	Secondary Support Members
Side Longitudinals	401.96	4.50	1.81	14.20	
Deck Longitudinals	480.24	4.50	2.16	16.96	
Bulkhead Longitudinals	1132.44	4.50	5.10	40.00	
Web Frame	3693.37	4.50	16.62	130.47	Transversal Reinforcements
Bulkhead Web	360.91	4.50	1.62	12.75	
Total Surface Area [m²]	3711.61				
Total Hull Mass [ton]	518.94				

3.2 Two Gyroscopes Test Case

As presented in section 4.1.2, the gyroscope roll will induce torques in both pitch and yaw directions. The former activates the angular motion of the PTO shaft and it is used to directly produce electric power from a variable frequency alternator. The latter, however, is extremely undesirable, as it excites the yaw motion of the hull. In this case an offset between the prevalent sea direction and the hull's longitudinal symmetry plane will always exist, and part of the wave energy will be transmitted to undesirable modes in the horizontal diametral plane, i.e. sway, roll and yaw.

To mitigate the yaw torque pairs of counter-rotating gyroscopes is used. Both flywheels will generate the same pitch torque, with equal magnitude and direction, but for yaw the torque will be opposite, negating the z-axis induced rotation completely (Fig. 3-6).

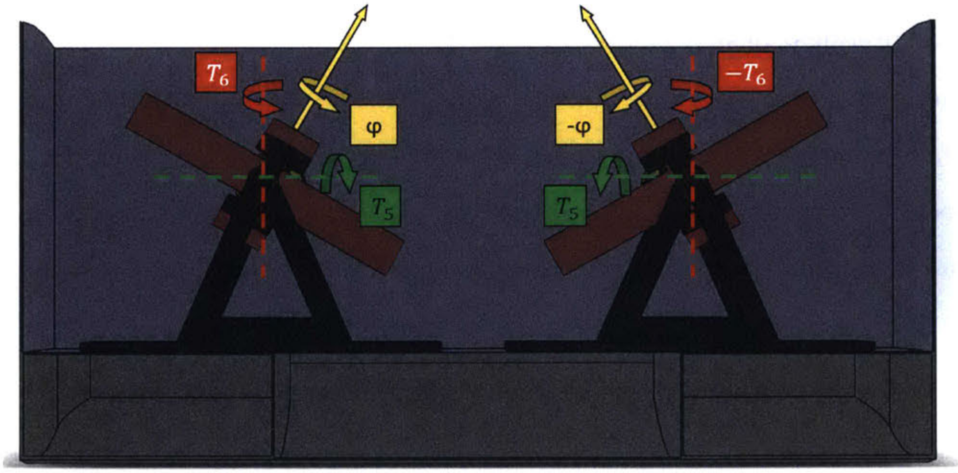

Figure 3-6: Pair of gyroscopes spinning counter to each other. The yaw torque is canceled, while the pitch is doubled.

In fact, the counter-rotating gyroscope pair solution is also desirable for other reasons, it creates redundancy of the power extraction system. This means the device will continue to extract energy, even if one of the gyroscope system fails.

For this specific case, the gyroscopes were sized to have the largest diameter possible, while still leaving gaps on the sides, bottom and top to allow for a complete 360° turn. Figure 3-7 shows the dimensions of gyroscope and hull of this case.

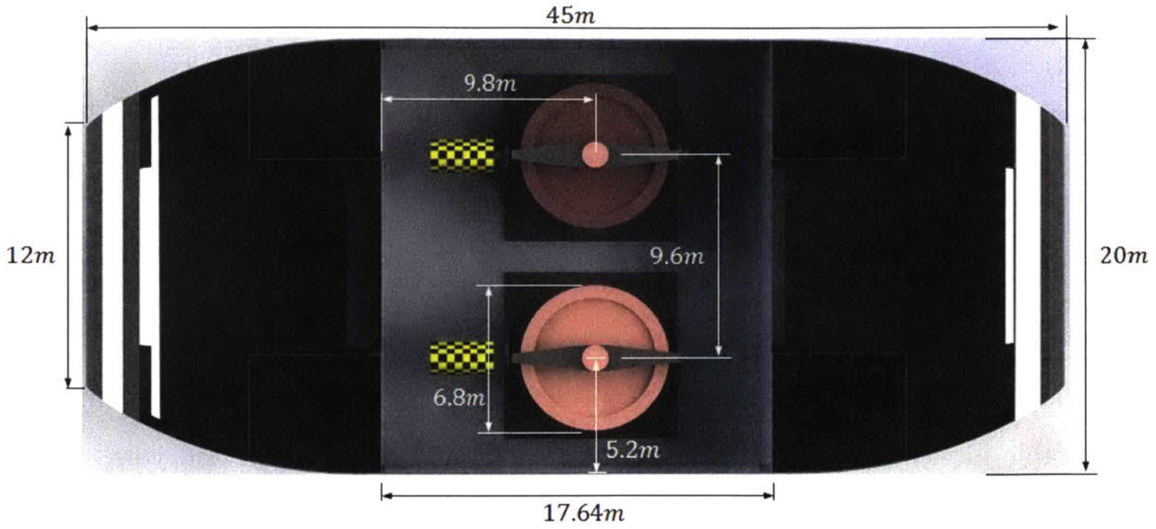

Figure 3-7: Dimensions of the 2 gyroscope case.

For this case the flywheel size and relative mass moment of inertia were chosen on the basis of practical design considerations which included criteria to minimize the construction costs. However, the quantity of interest is angular momentum, i.e. the product $J\varphi$, which is not known a priori. One idea is to use the bare hull's pitch RAO, make an educated guess of both the gyroscope's rotation amplitude at resonance and the desired nominal power output, through equation 4.42 estimate a value for the spin [9]. This complication can be avoided by using the ISWEC's design spin, scale it for our case and perform a sensibility analysis by means of the forthcoming numerical model.

The ISWEC model of $0.56m$ length has a design spin of $2150RPM$. This quantity scales with the square root of the scaling ratio and, assuming half the value,

$$\varphi = \frac{\varphi_{ISWEC}}{2}\sqrt{\frac{0.56}{45}} \simeq 120RPM \tag{3.4}$$

Table 3.3 summarizes all the characteristics of the two gyroscopes sized for this case. The VCG is measured from the free-surface, positive upwards, while the rest of the vertical quantities are measured from the keel.

Table 3.3: Gyroscope pair main dimensions.

Dimension	Value	Unit
d	6.8	m
m_f	140	ton
I_{xx}	$5.17 \cdot 10^5$	$kg \cdot m^2$
I_{yy}	$5.17 \cdot 10^5$	$kg \cdot m^2$
J	$1.02 \cdot 10^6$	$kg \cdot m^2$
I_x^f	$3.82 \cdot 10^3$	$kg \cdot m^2$
I_y^f	$3.32 \cdot 10^4$	$kg \cdot m^2$
I_z^f	$3 \cdot 10^4$	m

3.3 $1/50^{\text{th}}$ Scale Model Test Case

As part of the WEP program, a $1/50^{th}$ scale model experiment was carried out in the Davidson Laboratory from Stevens Institute of Technology. The model accounted for only one gyroscope, equipped with torque and rotational velocity measurement sensors, and a DC motor to drive the flywheel to the correct spin rate. The hull's motion tracking was done by placing four reflective spheres on the deck. These objects reflect infrared light, which are observed by a set of special cameras throughout the experiment. Figure 3-8 shows the model built for the tests, with its flywheel and load cells.

Table 3.4 presents all the dimensions of the scale model. A better discussion on the experimental setup and results will be presented later in chapter 7.

Figure 3-8: IOwec's $1/50^{\text{th}}$ scale model.

Table 3.4: $1/50^{\text{th}}$ scale model dimensions.

Body	**Dimension**	**Value**	**Unit**
Hull	L	0.9	m
	B	0.4	m
	D	0.2	m
	T_d	0.14	m
	VCG	-0.0297	m
	Δ	38.22	kg
	R_{xx}	0.169	m
	R_{yy}	0.299	m
	R_{zz}	0.077	m
Gyroscope	d	0.11	m
	m_f	1.45	kg
	I_x	$6.00 \cdot 10^{-3}$	$kg \cdot m^2$
	I_y	$2.377 \cdot 10^{-2}$	$kg \cdot m^2$
	J	$3.13 \cdot 10^{-3}$	$kg \cdot m^2$
	I_z^f	$5.11 \cdot 10^{-4}$	$kg \cdot m^2$

Chapter 4

Physical Model

This chapter covers the derivations of all dynamics of the IOwec, especially the coupling between hull and gyroscopes, as well as the Boundary Value Problem solved by Aegir. Since this work utilizes AEGIR as the BVP solver, the derivations of the hull motion will follow the same outline originally presented by Kring [14]. We will, however, limit ourselves to the dynamics of a stationary body. In case the reader desires a better understanding of the problem, including body translation, please refer to Kring's work.

4.1 Equations of Motion

4.1.1 Hull

Figure 4-1 shows an unrestricted floating body, free to move in its six, rigid-body, degrees of freedom about a non inertial frame of reference xyz_1 fixed to its equilibrium position. The body is stationary. The surfaces which constitute the problem are,

1. The sea free surface S_F, which contains the incoming wave signal and the body radiated waves;

2. The body surface S_B on which the waves pressure act. The integration of the pressures over this surface will later yield the external forcing;

3. The border surface S_∞, infinitely far from the body. The radiation condition is enforced on it (eq. 4.55).

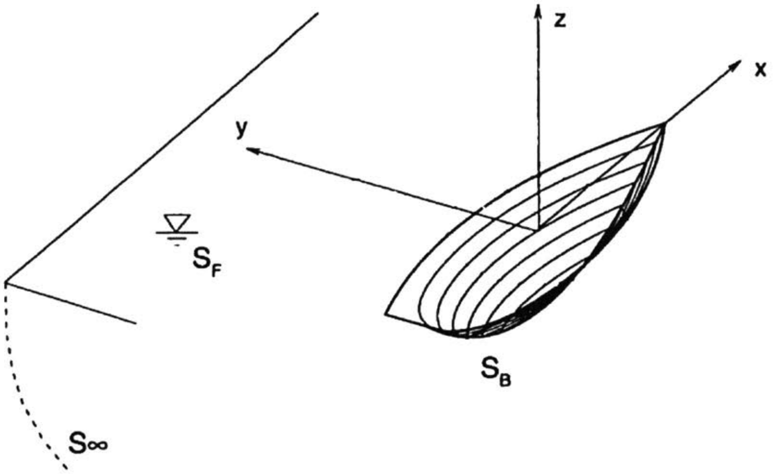

Figure 4-1: Submerged body reference frame [14].

The displacement $\vec{\delta}(\vec{x},t)$ of any point within the rigid body can be described by combining translation $\vec{\xi_T}(t)$ and rotation $\vec{\xi_R}(t)$.

$$\vec{\delta}(\vec{x},t) = \vec{\xi_T}(t) + \vec{\xi_R}(t) \times \vec{x} \tag{4.1}$$

From conservation of momentum (i.e. Newton's second law) we know the body's acceleration is proportional to the external forcing.

$$\begin{aligned} M_{ij}\ddot{\xi}_j(t) = F_j^h(\ddot{\xi}_j, \dot{\xi}_j, \xi_j, t) - c_{ij}\xi_j(t) \\ i,j = 1,2,...,6 \end{aligned} \tag{4.2}$$

The hydrostatic restoring coefficients c_{ij} are easily calculated from the traditional naval architecture knowledge [12]. The hydrodynamic forces F^h represent all the action of the waves on the body, depending on the displacement and its first and second derivatives of the latter. Since waves are intrinsic nonlinear, so are these forces [14].

The biggest simplification to this problem is the assumption of small body motions and wave disturbance with respect to the body's nominal size. This linearizes the problem, allowing the application of potential flow together with impulse theory and the decomposition of the forcing into impulsive (local) and wave (memory) forces, as proposed by Cummins [50]. We end up with an equation very similar to 2.45.

$$\left(M_{ij} + a^{o}_{ij}\right) \ddot{\xi}_j(t) + c_{ij}\xi_j = F^{m}_{j}(\dot{\xi}_j, \xi_j, t) \tag{4.3}$$

The fluid memory (wave) force F^m_j is independent of the body's acceleration, making the system solvable for $\ddot{\xi}_j$. Such forces may be written [14],

$$F^{m}_{j} = X_j(t) - \int_{-\infty}^{t} K(t-\tau)\dot{\xi}_j(\tau)d\tau \tag{4.4}$$

Where $K(t)$ is the velocity impulse function and $X_j(t)$ is the excitation force in the j^{th} mode. Figure 4-2 shows the IOwec's xyz_1 reference frame, where equation 4.3 is applicable, as well as the gyroscope's local frame xyz_2.

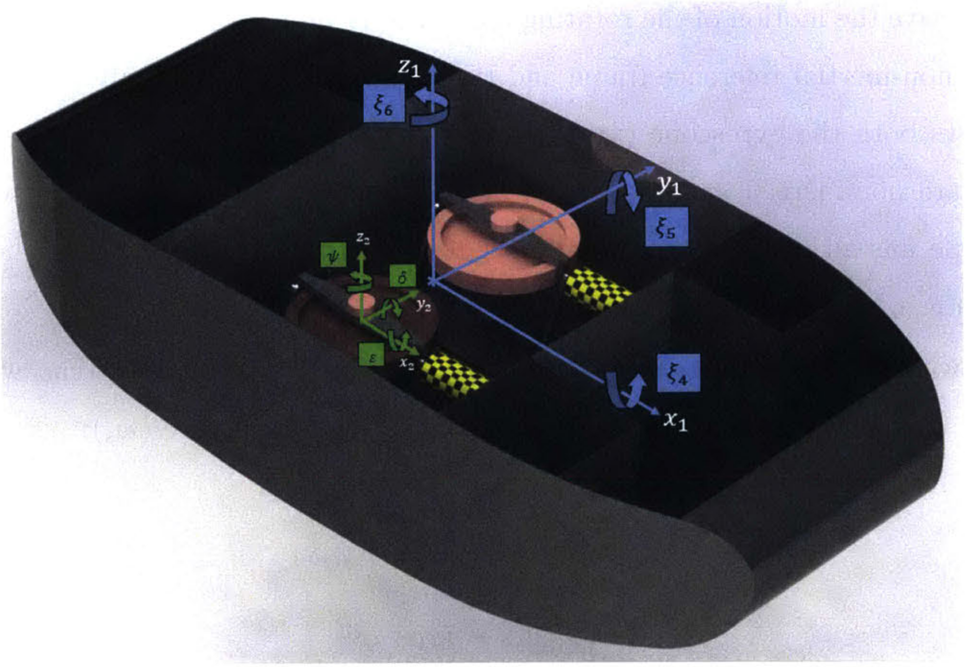

Figure 4-2: Hull Frame of Reference.

4.1.2 Gyroscope and Power Take-Off

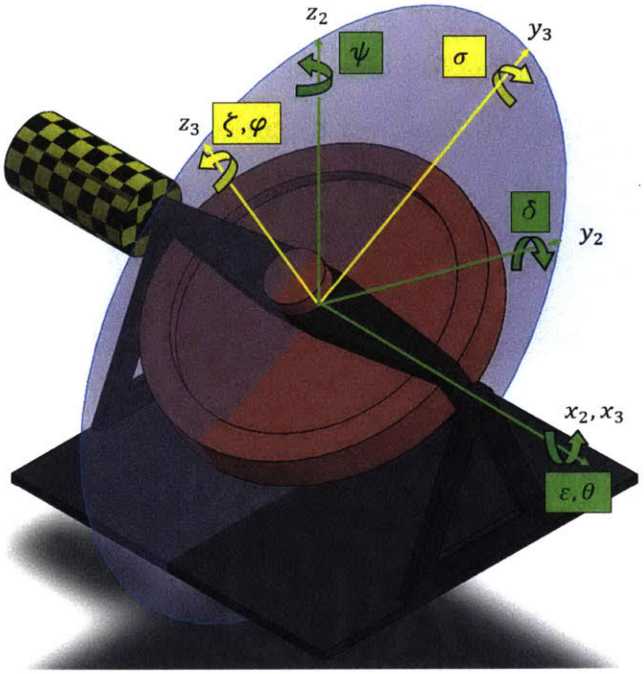

Figure 4-3: Gyroscope Frame of Reference.

To derive the motion of the rotating mass it is useful to describe it with respect to its own non-inertial reference frame and transform it back to the hull frame. Figure 4-3 shows both the gyroscope (xyz_3) and its support (xyz_2) reference frames. Both frames are non-inertial and the former rotates about the x-axis of the latter. The gyroscope has all DoFs fixed with respect to the moving hull, except for the x-axis rotation θ, where it is allowed to move freely.

Knowing that infinitesimal rotations can be treated as vectors, we can write the angular velocities of the flywheel (w_f) and of the whole structure (w_s):

$$\vec{w}_f = \dot{\theta}\hat{i}_3 + \dot{\sigma}\hat{j}_3 + (\dot{\zeta} + \dot{\varphi})\hat{k}_3 \tag{4.5}$$

$$\vec{w}_s = \dot{\theta}\hat{i}_3 + \dot{\sigma}\hat{j}_3 + \dot{\zeta}\hat{k}_3 \tag{4.6}$$

Both reference frames coincide with the gyroscope principal axes of inertia. The inertia matrix of the flywheel can then be diagonalized and written as:

$$[I]_3 = \begin{bmatrix} I_{xx} & & \\ & I_{yy} & \\ & & J \end{bmatrix} \tag{4.7}$$

The contribution of the gyroscope structural frame to the inertia will be added later on. With the angular velocities outlined we can proceed with the derivation of the equation of motion of the gyroscope.

We are interested in the frame following the gyroscope flywheel (Eq. 4.5), which is also the system's principal axis, sitting on top of the Center of Gravity (CoG). The angular momentum can be written as:

$$\vec{H}_f = [I]_3 \cdot \vec{w}_f = \begin{bmatrix} I_{xx} & & \\ & I_{yy} & \\ & & J \end{bmatrix} \begin{bmatrix} \dot{\theta} \\ \dot{\sigma} \\ \dot{\zeta} + \dot{\varphi} \end{bmatrix} \tag{4.8}$$

$$\vec{H}_f = I_{xx}\dot{\theta}\hat{\imath}_3 + I_{yy}\dot{\sigma}\hat{\jmath}_3 + J(\dot{\zeta} + \dot{\varphi})\hat{k}_3 \tag{4.9}$$

The principle of angular momentum conservation states that external torques applied to the system equal the change in angular momentum.

$$\vec{T}_{ext} = \frac{d\vec{H}_f}{dt} \tag{4.10}$$

Since the xyz_3 frame is not inertial, taking the time derivative of the angular momentum means also evaluating the variation of the axes versors.

$$\begin{aligned} \vec{T}_{ext} =& I_{xx}\left(\ddot{\theta}\hat{\imath}_3 + \dot{\theta}\frac{d\hat{\imath}_3}{dt}\right) + I_{yy}\left(\ddot{\sigma}\hat{\jmath}_3 + \dot{\sigma}\frac{d\hat{\jmath}_3}{dt}\right) \\ &+ J\left(\ddot{\zeta}\hat{k}_3 + \dot{\zeta}\frac{d\hat{k}_3}{dt} + \ddot{\varphi}\hat{k}_3 + \dot{\varphi}\frac{d\hat{k}_3}{dt}\right) \end{aligned} \tag{4.11}$$

The versors time derivatives are due to the frame rotation.

$$\frac{d\hat{\imath}_3}{dt} = \vec{w}_s \times \hat{\imath}_3 = \dot{\zeta}\hat{\jmath}_3 - \dot{\sigma}\hat{k}_3 \tag{4.12}$$

$$\frac{d\hat{j}_3}{dt} = \vec{w}_s \times \hat{j}_3 = \dot{\theta}\hat{k}_3 - \dot{\zeta}\hat{i}_3 \tag{4.13}$$

$$\frac{d\hat{k}_3}{dt} = \vec{w}_s \times \hat{k}_3 = \dot{\sigma}\hat{i}_3 - \dot{\zeta}\hat{j}_3 \tag{4.14}$$

Substituting the versors time derivatives into equation 4.11 yields the gyroscope equation for the xyz_3 frame.

$$\begin{aligned}\vec{T}_{ext} = &\left[I_{xx}\ddot{\theta} + (J - I_{yy})\dot{\sigma}\dot{\zeta} + J\dot{\sigma}\dot{\varphi}\right]\hat{i}_3 + \left[I_{yy}\ddot{\sigma} + (I_{xx} - J)\dot{\theta}\dot{\zeta} - J\dot{\theta}\dot{\varphi}\right]\hat{j}_3 \\ &+ \left[J(\ddot{\varphi} + \ddot{\zeta})\right]\hat{k}_3\end{aligned} \tag{4.15}$$

To transform the above equation from the xyz_3 to the xyz_2 frame we consider the following simple rotation matrix.

$$R = \begin{bmatrix} 1 & 0 & 0 \\ 0 & \cos\theta & \sin\theta \\ 0 & -\sin\theta & \cos\theta \end{bmatrix} \tag{4.16}$$

$$\begin{bmatrix} \dot{\theta} \\ \dot{\sigma} \\ \dot{\zeta} \end{bmatrix} = \begin{bmatrix} 1 & 0 & 0 \\ 0 & \cos\theta & \sin\theta \\ 0 & -\sin\theta & \cos\theta \end{bmatrix} \begin{bmatrix} \dot{\theta} \\ \dot{\delta} \\ \dot{\psi} \end{bmatrix} = \begin{bmatrix} \dot{\theta} \\ \dot{\delta}\cos\theta + \dot{\psi}\sin\theta \\ -\dot{\delta}\sin\theta + \dot{\psi}\cos\theta \end{bmatrix} \tag{4.17}$$

Previously, in section 4.1.1, we defined the hull as a rigid-body. This makes rotation on xyz_2 and xyz_1 frames essentially the same thing, turning the xyz_2 frame useful only as a mean of grabbing the mind by the hand and walking with it through very easy to follow derivation steps. Let's jump straight into the hull's xyz_1 frame, which is the one we really care about.

$$\dot{\sigma} = \dot{\xi}_5\cos\theta + \dot{\xi}_6\sin\theta \tag{4.18}$$

$$\dot{\zeta} = -\dot{\xi}_5\sin\theta + \dot{\xi}_6\cos\theta \tag{4.19}$$

We have now started to explicitly couple the gyroscope to the hull. The accelerations come from the time derivatives of the two equations above.

$$\ddot{\sigma} = \ddot{\xi}_5 \cos\theta - \dot{\xi}_5\dot{\theta}\sin\theta + \ddot{\xi}_6 \sin\theta + \dot{\theta}\cos\theta \tag{4.20}$$

$$\ddot{\zeta} = -\ddot{\xi}_5 \sin\theta - \dot{\xi}_5\dot{\theta}\cos\theta + \ddot{\xi}_6 \cos\theta - \dot{\xi}_6\dot{\theta}\sin\theta \tag{4.21}$$

The torque equation suffers the same transformation from equation 4.17.

$$\begin{bmatrix} T_{x3} \\ T_{y3} \\ T_{z3} \end{bmatrix} = \begin{bmatrix} 1 & 0 & 0 \\ 0 & \cos\theta & \sin\theta \\ 0 & -\sin\theta & \cos\theta \end{bmatrix} \begin{bmatrix} T_{x1} \\ T_{y1} \\ T_{z1} \end{bmatrix} = \begin{bmatrix} T_{x1} \\ T_{y1}\cos\theta + T_{z1}\sin\theta \\ -T_{y1}\sin\theta + T_{z1}\cos\theta \end{bmatrix} \tag{4.22}$$

The Power Take-Off (PTO), responsible for the conversion of mechanical energy to electricity, acts on the gyroscope x-axis, as illustrated in figure 4-3. The simplest model for it is a linear spring-dashpot, where the spring represents a reactive control, responsible for tuning the PTO's natural frequency to that of the incoming waves, and the dashpot represents the mechanics of power extraction, as a damping term.

$$T_{x1} \equiv T_{PTO} = -k_l\theta - c_l\dot{\theta} \tag{4.23}$$

The gyroscope roll acceleration is independent of the hull's, making this specific DoF uncoupled and solvable by just rearranging the terms of equation 4.15 and making use of relations 4.18, 4.19 and 4.23.

$$\begin{aligned} I_{xx}\ddot{\theta} =& (I_{yy} - J)\left[\dot{\xi}_5\dot{\xi}_6(\cos^2\theta - \sin^2\theta) + (\dot{\xi}_6^2 - \dot{\xi}_5^2)\sin\theta\cos\theta\right] \\ & - J\dot{\varphi}(\dot{\xi}_5\cos\theta + \dot{\xi}_6\sin\theta) - k_l\theta - c_l\dot{\theta} \end{aligned} \tag{4.24}$$

The pitch and yaw torques induced by the gyroscope on the hull:

$$\begin{aligned} T_{y1} =& (I_{yy}\cos^2\theta + J\sin^2\theta)\ddot{\xi}_5 + (I_{yy} - J)\sin\theta\cos\theta\ddot{\xi}_6 \\ & + (2J - I_{xx} - I_{yy})\dot{\xi}_5\dot{\theta}\cos\theta + (\sin^2\theta - \cos^2\theta)J\dot{\xi}_6\dot{\theta} \\ & + (I_{xx} + I_{yy})\cos^2\theta\dot{\xi}_6\dot{\theta} - J\dot{\varphi}\dot{\theta}\cos\theta \end{aligned} \tag{4.25}$$

$$\begin{aligned} T_{z1} =&(I_{yy} - J)\sin\theta\cos\theta\ddot{\xi}_5 + (I_{yy}\sin^2\theta + J\cos^2\theta)\ddot{\xi}_6 \\ &- (I_{xx} + I_{yy} - J)\dot{\xi}_5\dot{\theta}\sin^2\theta - (I_{xx} + I_{yy} - 2J)\dot{\xi}_6\dot{\theta}\sin\theta\cos\theta \\ &- J\dot{\xi}_5\dot{\theta}\cos^2\theta - J\dot{\varphi}\dot{\theta}\sin\theta \end{aligned} \tag{4.26}$$

The gyroscope moments of inertia from relation 4.7 consider only the distribution of the flywheel mass. To write the final equations of motion we must incorporate the gyroscope frame. The total system inertia matrix is:

$$[I]_{tot} = \begin{bmatrix} I_x & & \\ & I_y & \\ & & I_z \end{bmatrix} = \begin{bmatrix} I_{xx} + I_{fx} & & \\ & I_{yy} + I_{fy} & \\ & & J + I_{fz} \end{bmatrix} \tag{4.27}$$

The final equations of motion of the gyroscope reduce to:

$$\begin{aligned} I_x\ddot{\theta} =&(I_y - I_z)\left[\dot{\xi}_5\dot{\xi}_6(\cos^2\theta - \sin^2\theta) + (\dot{\xi}_6^2 - \dot{\xi}_5^2)\sin\theta\cos\theta\right] \\ &- J\dot{\varphi}(\dot{\xi}_5\cos\theta + \dot{\xi}_6\sin\theta) - k_l\theta - c_l\dot{\theta} \end{aligned} \tag{4.28}$$

$$\begin{aligned} T_{y1} =&(I_y\cos^2\theta + I_z\sin^2\theta)\ddot{\xi}_5 + (I_y - I_z)\sin\theta\cos\theta\ddot{\xi}_6 \\ &+ (2I_z - I_x - I_y)\dot{\xi}_5\dot{\theta}\cos\theta\sin\theta + (\sin^2\theta - \cos^2\theta)J\dot{\xi}_6\dot{\theta} \\ &+ (I_x + I_y)\cos^2\theta\dot{\xi}_6\dot{\theta} - J\dot{\varphi}\dot{\theta}\cos\theta \end{aligned} \tag{4.29}$$

$$\begin{aligned} T_{z1} =&(I_y - I_z)\sin\theta\cos\theta\ddot{\xi}_5 + (I_y\sin^2\theta + I_z\cos^2\theta)\ddot{\xi}_6 \\ &- (I_x + I_y - I_z)\dot{\xi}_5\dot{\theta}\sin^2\theta - (I_x + I_y - 2I_z)\dot{\xi}_6\dot{\theta}\sin\theta\cos\theta \\ &- I_z\dot{\xi}_5\dot{\theta}\cos^2\theta - J\dot{\varphi}\dot{\theta}\sin\theta \end{aligned} \tag{4.30}$$

It is interesting to notice the difference between the yaw and pitch induced torques. The dominating terms for both are, respectively, $J\dot{\varphi}\dot{\theta}\sin\theta$ and $J\dot{\varphi}\dot{\theta}\cos\theta$. Considering small oscillations of the gyroscope, these two terms reduce to $J\dot{\varphi}\dot{\theta}\theta$ and $J\dot{\varphi}\dot{\theta}$. This means, due to the product $\dot{\theta}\theta$, the yaw rotation induced by the flywheel should have a frequency equivalent to twice that of the wave, while pitch retains the same period.

4.1.3 Gyroscope Linearization and Power Prediction

To better understand the system we should linearize equation 4.28. Doing so will allow us to draw early conclusions on how the PTO should be setup. Getting rid of all terms of order $O({\xi_j}^2, \theta^2)$ and above, while also considering small roll angles for the gyroscope, we find,

$$I_x\ddot{\theta} = -J\varphi\dot{\xi}_5 - c_l\dot{\theta} - k_l\theta \tag{4.31}$$

We are now allowed to apply the Fourier Transform and move into frequency domain. The relevant variables assume the form below.

$$\begin{aligned} \theta &= \Theta(\omega)e^{i\omega t} \\ \dot{\theta} &= i\omega\Theta(\omega)e^{i\omega t} \\ \ddot{\theta} &= -\omega^2\Theta(\omega)e^{i\omega t} \\ \dot{\xi}_5 &= i\omega\Xi_5(\omega)e^{i\omega t} \end{aligned} \tag{4.32}$$

Substituting the relations in 4.32 into equation 4.31 and rearranging the terms we find a relation between the hull pitch and the gyroscope roll,

$$\Theta = \frac{J\varphi i\omega}{I_x\omega^2 - i\omega c_l - k_l}\Xi_5 \tag{4.33}$$

Now, we know the PTO acts on the flywheel. We can then substitute the reactive control spring by introducing a PTO natural frequency ω_{PTO} [9],

$$\omega_{PTO}^2 = \frac{k_l}{J} \tag{4.34}$$

Equation 4.33 then becomes,

$$\Theta = \frac{J\varphi i\omega}{(I_x\omega^2 - J\omega_{PTO}^2) - i\omega c_l}\Xi_5 \tag{4.35}$$

It is clear now that we must tune ω_{PTO} to match the wave's incoming frequency. The ideal PTO spring constant becomes,

$$k_l = I_x \cdot \omega^2 \tag{4.36}$$

The power is extracted by the PTO through the linear damping coefficient c_l. In time-domain, the instantaneous power extracted can be expressed as,

$$P_E(t) = c_l \cdot \dot{\theta}^2 \tag{4.37}$$

It is easier to evaluate the average power extracted over one wave period, since this will directly relate the PTO with equation 2.14, giving us a more reasonable metric for efficiency,

$$\bar{P_E}(t) = \frac{1}{T}\int_0^T c_l \dot{\theta}^2 dt \tag{4.38}$$

The averaged power extracted over one wave period can also be written in the frequency domain,

$$\bar{P_E}(\omega) = \frac{1}{2} c_l \left|\dot{\theta}\right|^2 = \frac{1}{2} c_l \omega^2 \Theta^2 \tag{4.39}$$

Substituting equation 4.35 into 4.39,

$$\bar{P_E}(\omega) = \frac{c_l}{2} \frac{(J\varphi\omega^2\Xi_5)^2}{(I_x\omega^2 - J\omega_{PTO}^2)^2 + \omega^2 {c_l}^2} \tag{4.40}$$

For the optimum reactive control, the power extracted becomes,

$$\bar{P_E}(\omega) = \frac{(J\varphi\omega\Xi_5)^2}{2c_l} \tag{4.41}$$

We know, from equation 4.39, that $c_l = 2\bar{P_E}/\omega^2\Theta^2$. The relation for the averaged extracted power takes the final form,

$$\bar{P_E}(\omega) = \frac{J\varphi\omega^2\Xi_5\Theta}{2} \tag{4.42}$$

We now have a very easy way to estimate what would be the power prediction of the device by just knowing the hull and gyroscope motions. Also, the optimum reactive control can be designed for every incoming wave frequency, guaranteeing resonance. The damping would always be optimized for such condition.

4.1.4 State-Space Model

The mathematical formulations regarding the hull, stated in sections 4.1.1 and 4.1.2, are written in a state-space format in Aegir. The MATLAB code which implement the gyroscope and PTO mechanics also has to follow the same convention. Going down the same path as outlined by Kring, the six DoF, second order, equations of motion can be modified into twelve of first degree [14].

$$\frac{d\vec{y}}{dt} = \vec{f}(t) \tag{4.43}$$

With the state vector $\vec{y}$ written as a combination of displacements and velocities.

$$\vec{y}(t) = \begin{bmatrix} \vec{y}_1(t) \\ \vec{y}_2(t) \end{bmatrix} = \begin{bmatrix} \dot{\xi}_j(t) \\ \xi_j(t) \end{bmatrix} \tag{4.44}$$

Gyroscopic terms $\vec{T}_i^a(t)$, proportional to the hull's acceleration, will go alongside mass terms, just like the added-mass. The forcing vector becomes:

$$f(\vec{t}) = \begin{bmatrix} \vec{f}_1(t) \\ \vec{f}_2(t) \end{bmatrix} = \tag{4.45}$$

$$\begin{bmatrix} -\left[M + a_o + \sum_{i=1}^{n} T_i^a(t)\right]^{-1} \left[C\vec{y}_2(t) + \int_0^t K(t-\tau)\vec{y}_1(\tau)d\tau + \sum_{i=1}^{n} T_i^v(\vec{y}_1, t)\right] \\ \vec{y}_1(t) \end{bmatrix}$$

Where n is the total number of gyroscopes inside the hull. Both acceleration and velocity proportional gyroscope torque matrices, coming from equations 4.29 and 4.30, are non-zero only for pitch and yaw.

$$T_i^a(\dot{\vec{y}}_1, t) = \begin{bmatrix} 0 & \cdots & \cdots & \cdots & \cdots & 0 \\ \vdots & \ddots & & & & \vdots \\ \vdots & & \ddots & & & \vdots \\ \vdots & & & \ddots & & \vdots \\ \vdots & & & & T^a_{55,i} & T^a_{56,i} \\ 0 & \cdots & \cdots & \cdots & T^a_{65,i} & T^a_{66,i} \end{bmatrix} \tag{4.46}$$

Where,

$$\begin{aligned} T^a_{55,i} &= I_y \cos^2\theta + I_z \sin^2\theta \\ T^a_{56,i} &= (I_y - I_z)\sin\theta\cos\theta \\ T^a_{65,i} &= (I_y - I_z)\sin\theta\cos\theta \\ T^a_{66,i} &= I_y \sin^2\theta + I_z \cos^2\theta \end{aligned} \tag{4.47}$$

The gyroscope velocity proportional vector,

$$T_i^v(\vec{y}_1, t) = \begin{bmatrix} 0 \\ \\ \vdots \\ \\ T^v_{5,i} \\ T^v_{6,i} \end{bmatrix} \tag{4.48}$$

Where,

$$\begin{aligned} T_5^v =& -(2I_z - I_x - I_y)\dot{\xi}_5\dot{\theta}\cos\theta\sin\theta - (\sin^2\theta - \cos^2\theta)J\dot{\xi}_6\dot{\theta} \\ & - (I_x + I_y)\cos^2\theta\dot{\xi}_6\dot{\theta} + (-1)^i J\dot{\varphi}\dot{\theta}\cos\theta \\ T_6^v =& (I_x + I_y - I_z)\dot{\xi}_5\dot{\theta}\sin^2\theta + (I_x + I_y - 2I_z)\dot{\xi}_6\dot{\theta}\sin\theta\cos\theta \\ & + I_z\dot{\xi}_5\dot{\theta}\cos^2\theta + (-1)^i J\dot{\varphi}\dot{\theta}\sin\theta \end{aligned} \tag{4.49}$$

As will be seen in section 5.2.2, the time scheme used for body motion is a 4^{th} order Runge-Kutta. This means we have predictor and corrector steps before computing the next state vector. Aegir will give us the hull state without any external dynamics, and we consider that these values can be used for ξ_5 and ξ_6, allowing us to retain all the terms in the gyroscope equation of motion. The solution is expected to converge for a time-step small enough.

4.2 The Time-Domain Boundary Value Problem

Here we consider the fluid flow incompressible, irrotational and inviscid, making all the derivations of chapter 2 applicable to this hull with gyroscopes problem. This means the flow can be represented by a velocity potential $\Psi(\vec{x},t)$, which must satisfy the conservation of mass stated by equation 2.2. The flow pressure can also be calculated in the xyz_o frame by equation 2.3. The kinematic and dynamic free-surface boundary conditions are treated the same way as in table 2.1, respectively [14],

$$\left(\frac{d}{dt} + \nabla\Psi(\vec{x},t)\cdot\nabla\right)\left[z - \eta\left(x,y,t\right)\right] = 0 \quad \text{applied on} \quad z = \eta\left(x,y,t\right) \tag{4.50}$$

$$\frac{\Psi}{dt} = -g\eta - \frac{1}{2}\nabla\Psi\cdot\nabla\Psi \quad \text{applied on} \quad z = \eta\left(x,y,t\right) \tag{4.51}$$

We now have the body surface inside the domain. Its boundary condition states no fluid may flow through it [14],

$$\frac{\partial\Psi(\vec{x},t)}{\partial n} = \vec{V}_B\cdot\vec{n} \quad \text{applied on} \quad S_B \tag{4.52}$$

The body velocity $\vec{V}_B$ is further divided into steady and unsteady components [14]. The former is, for our purposes, null.

$$\vec{V}_{Bs} = 0 \quad \text{applied on} \quad S_B \tag{4.53}$$

$$\vec{V}_{Bu} = \frac{\partial\delta}{\partial t} \quad \text{applied on} \quad S_B \tag{4.54}$$

The radiation condition must also be imposed, it states that the velocity potential must decay to zero infinitely away from the body within a finite period of time.

$$\nabla\Psi \rightarrow 0 \quad \text{at} \quad S_\infty \tag{4.55}$$

Kring follows the same approach first presented by Cummins, and considers the total disturbance potential $\Psi(\vec{x},t)$ to be a superposition of three flows, the basis Φ, the local ϕ_l and the memory (wave) ψ [50].

$$\Psi(\vec{x},t) = \Phi(\vec{x}) + \phi_l(\vec{x},t) + \psi(\vec{x},t) \tag{4.56}$$

The basis flow $\Phi(\vec{x})$ is only important for ships translating on the free-surface, which is not our case. The local flow $\phi_l(\vec{x},t)$ represents the instantaneous fluid response due to the impulsive body motion, which "talks" to the memory flow $\psi(\vec{x},t)$, which represents the wave flow, through the free-surface boundary condition [14].

To arrive at the linear boundary conditions we first drop second order terms. Then we apply a Taylor expansion about the mean body position for the body condition and about $z = 0$ for the free-surface, keeping only its linear terms [14].

1. Kinematic Free-Surface Condition

$$\frac{\partial\eta}{\partial t} = \frac{\partial\phi_l}{\partial z} + \frac{\partial\psi}{\partial z} \quad \text{applied on} \quad z = 0 \tag{4.57}$$

2. Dynamic Free-Surface Condition

$$\frac{\partial}{\partial t}(\phi_l + \psi) = -g\eta - \frac{1}{2}\nabla\phi_l \cdot \nabla\phi_l \quad \text{applied on} \quad z = 0 \tag{4.58}$$

3. Body Boundary Condition

$$\frac{\partial\phi_l}{\partial n} = \frac{\partial\delta}{\partial t} \cdot \vec{n} - \nabla\psi \cdot \vec{n} \quad \text{applied on} \quad S_B \tag{4.59}$$

Substituting equation 4.1 into 4.59 yields the body boundary condition in Ogilvie and Tuck's notation, minus the m-terms. These omitted terms would be fundamental if our body had a translation velocity [14, 56].

$$\frac{\partial \phi_l}{\partial n} = \sum_{j=1}^{6} \left(\frac{\partial \xi_j}{\partial t} \right) \tag{4.60}$$

Where,

$$\begin{aligned} (n_1, n_2, n_3) &= \vec{n} \\ (n_4, n_5, n_6) &= \vec{x} \times \vec{n} \end{aligned} \tag{4.61}$$

Particularly for the pressure calculation, the linearized Bernoulli equation can be decomposed into local p_l, memory p_m and hydrostatic p_h components. The total pressure is $p = p_l + p_m + p_h$ [14].

$$p_l = -\rho \frac{\partial \phi_l}{\partial t} \tag{4.62}$$

$$p_m = -\rho \frac{\partial \psi}{\partial t} \tag{4.63}$$

$$p_h = -\rho g z \tag{4.64}$$

Finally, the force acting on the body is the integration of the pressure on S_B.

$$F_j = \iint_{S_B} p \cdot n_j dS \quad \text{for} \quad j = 1, \ldots, 6 \tag{4.65}$$

4.2.1 The Local Flow Contribution

The local flow can be decomposed into terms proportional to the acceleration, velocity and displacement of the body. Only the ones due to acceleration are non-zero for a stationary body (i.e. the basis flow is absent), yielding the a^0 term written in equation 4.3 [14].

$$a^0_{jk} = \rho \iint_{S_B} (\mathcal{N}_k) n_j dS \tag{4.66}$$

Where,

$$
\begin{aligned}
&\mathcal{N}_k = 0 \quad \text{on} \quad z = 0 \\
&\frac{\mathcal{N}_k}{\partial n} = n_k \quad \text{on} \quad S_B \\
&\text{for} \quad k = 1, \ldots, 6
\end{aligned}
\tag{4.67}
$$

4.2.2 The Memory Flow Contribution

If an incident wave is imposed in the domain, it is represented as an extra component of the memory flow ($\psi = \psi + \Psi_I$ and $\eta = \eta + \eta_I$). The body boundary condition becomes [14],

$$
\frac{\partial \psi}{\partial n} = -\frac{\Psi_I}{\partial n} \quad \text{on} \quad S_B \tag{4.68}
$$

The free-surface conditions outlined in equations 4.57 and 4.58 have the unknown velocity potentials. They will be solved by Aegir at every time-step, calculating the free-surface deformation [14].

4.2.3 The boundary integral formulation

Green's second identity is applied to the boundary value problem in the very same way as previously described in section 2.3, yielding a very similar equation to 2.37 [14],

$$
2\pi\Psi(\vec{x}) - \iint_{S_F \cup S_B} \frac{\partial \Psi(\vec{x}')}{\partial n} G(\vec{x}'; \vec{x}) dx' + \iint_{S_F \cup S_B} \Psi(\vec{x}') \frac{\partial G(\vec{x}'; \vec{x})}{\partial n} dx' = 0 \tag{4.69}
$$

Finally, Aegir is called a Rankine panel method due to its choice on the Rankine source potential as the known function in the integral,

$$
G(\vec{x}'; \vec{x}) = \frac{1}{|\vec{x} - \vec{x}'|} \tag{4.70}
$$

4.3 Nonlinear Effects in Aegir

Resolving the free-surface deformation allows Aegir to be extended to consider some nonlinearities. The first of them are nonlinear incident (Froude-Krylov) and restoring forces, which, despite linearization of the boundary conditions, can now have the pressure integral up to the actual, deformed, free-surface.

The second is nonlinear body boundary condition. This means that, instead of using the mean body position, Aegir will re-mesh the hull and re-compute the waterline intersection at every time-step.

Unfortunately, nonlinear body boundary condition is prohibitive due to its high computational cost. As we will see in section 5.2.2, a 4^{th} order Runge-Kutta will be used for motion integration, meaning the re-meshing has to be performed four times for every time-step. In a standard workstation, with 8 nodes of 3.6GHz processing speed, it takes about 25 minutes to compute one time-step, meaning it would take about 11 days to finish a run of only one wave period.

Chapter 5

Numerical Model

With the boundary value problem outlined in section 4.2 we are ready to describe the numerical method utilized to solve it. We will need to do both space and time discretization, transforming equations 4.57 to 4.59 and 4.69 into a discrete representation.

Aegir in particular is a high-order panel method, meaning the surfaces are represented mathematically as non-uniform basic spline surfaces (NURBS) which will be broken down into the desired number of discreet quadrilateral facets. As stated previously, it is a Rankine panel method due to the choice of the Ranking source as the Green function in the boundary integral formulation (eq. 4.70).

Finally, in a discrete scenario, our domain is bounded. This means the radiation condition (eq. 4.55) must be imposed on the edges of the domain somehow. This is achieved in Aegir by placing "numerical beaches" which will artificially dampen the outgoing waves far from the body.

5.1 Spatial Discretization

Applying Green's second identity to the boundary value problem in section 4.2 transformed it into surface integrals across the boundaries. This is where panel methods do a fantastic job, taking those surfaces and breaking them down in discrete pieces for numerical analysis of the governing equations.

In the spatial discretization we are concerned in representing the free-surface and the body. The former has elevation $\eta(x,y,t)$, potential $\psi(\vec{x},t)$ and vertical velocity $\partial\psi/\partial z$ as unknowns. The latter has the potential $\psi(\vec{x},t)$ on the body as unknown.

Space is discretized in Aegir through B-splines weighted by specific time-dependent coefficients [14],

$$\begin{aligned}\psi(\vec{x},t) &\simeq \sum_j \psi_j(t)B_j(\vec{x}) \\ \eta(\vec{x},t) &\simeq \sum_j \eta_j(t)B_j(\vec{x}) \\ \frac{\partial\psi}{\partial n}(\vec{x},t) &\simeq \sum_j (\psi_z)_j(t)B_j(\vec{x})\end{aligned} \tag{5.1}$$

with,

$$B(x,y) = b(x)b(y) \tag{5.2}$$

The basis functions within a panel is a second-order B-spline, meaning first and second derivatives can be obtained analytically [14],

$$b(x) = \begin{cases} \frac{1}{2l_p^2}\left(x+\frac{3l_p}{2}\right)^2, & \text{on} \quad -\frac{3l_p}{2} < x < -\frac{l_p}{2} \\ \frac{1}{l_p^2}\left(-x^2+\frac{3l_p^2}{4}\right), & \text{on} \quad -\frac{l_p}{2} < x < \frac{l_p}{2} \\ \frac{1}{2l_p^2}\left(-x+\frac{3l_p}{2}\right)^2, & \text{on} \quad \frac{l_p}{2} < x < \frac{3l_p}{2} \end{cases} \tag{5.3}$$

Where l_p is the panel width. Applying such basis function on equations 4.57, 4.58 and 4.69 yields the discreet formulation of the kinematic and dynamic boundary conditions and boundary integral formulation, respectively. The first two are time dependent, while the last is a linear system of equations whose size depends on the number of panels in the problem [14].

$$\frac{\partial\eta_j}{\partial t}B_{ij} = \frac{\partial\phi_l}{\partial z} + \frac{\psi_j}{\partial z}B_{ij} \tag{5.4}$$

$$\frac{\partial\psi_j}{\partial t}B_{ij} = -\eta_j g B_{ij} \tag{5.5}$$

$$2\pi\psi_j B_{ij} + \psi_j D_{ij} - \frac{\partial \psi_j}{\partial z} S_{ij} = 0 \tag{5.6}$$

Where,

$$\begin{aligned} B_{ij} &= B_j(\vec{x}_i) = B_{i-j} \\ D_{ij} &= \iint_{-\infty}^{\infty} B_j(\vec{x}')\frac{dG(\vec{x}_i;\vec{x}')}{dn}d\vec{x}' = D_{i-j} \\ S_{ij} &= \iint_{-\infty}^{\infty} B_j(\vec{x}')G(\vec{x}_i;\vec{x}')d\vec{x}' = S_{i-j} \end{aligned} \tag{5.7}$$

5.2 Temporal Discretization

5.2.1 Free-Surface Boundary Condition

The free-surface temporal discretization uses what Kring calls an emplicit method, which is a mix of explicit and implicit euler schemes. Equations 5.4 through 5.6 become [14],

$$\frac{\eta_j^{n+1} - \eta_j^n}{\Delta t} B_{ij} = \frac{\partial \phi_l}{\partial z} + \frac{\partial \psi_j^n}{\partial z} B_{ij} \tag{5.8}$$

$$\frac{\psi_j^{n+1} - \psi_j^n}{\Delta t} B_{ij} = -\eta_j^{n+1} g B_{ij} \tag{5.9}$$

$$2\pi\psi_j^{n+1} B_{ij} + \psi_j^{n+1} D_{ij} - \frac{\partial \psi_j^{n+1}}{\partial z} S_{ij} = 0 \tag{5.10}$$

5.2.2 Body Motion

The time marching scheme for the body motion is the Runge-Kutta 4^{th} order. It consists of four steps, the first is a forward euler of half-step, the second an implicit euler corrector, still with half-step, but now using the previous prediction as current state-vector. The third is a full step mid-point rule, using the predicted value. Finally, the last consists of a Simpson's rule which uses all previous steps to build the true state-vector [57]. Using a multi-point method allows the use of larger time-steps while still maintaining numerical stability, while, in particular for the Runge-Kutta, not needing extra points for calculation.

1. Forward Euler Predictor

$$\vec{y}^{*}_{n+\frac{1}{2}} = \vec{y}_n + \frac{\Delta t}{2}\frac{d\vec{y}_n}{dt} \tag{5.11}$$

2. Implicit Euler Corrector

$$\vec{y}^{**}_{n+\frac{1}{2}} = \vec{y}_n + \frac{\Delta t}{2}\frac{d\vec{y}^{*}_{n+\frac{1}{2}}}{dt} \tag{5.12}$$

3. Midpoint Rule Predictor

$$\vec{y}^{*}_{n+1} = \vec{y}_n + \Delta t\frac{d\vec{y}^{**}_{n+\frac{1}{2}}}{dt} \tag{5.13}$$

4. Simpson's Rule Corrector

$$\vec{y}_{n+1} = \vec{y}_n + \frac{\Delta t}{6}\left(\frac{d\vec{y}_n}{dt} + \frac{d\vec{y}^{*}_{n+\frac{1}{2}}}{dt} + \frac{d\vec{y}^{**}_{n+\frac{1}{2}}}{dt} + \frac{d\vec{y}^{*}_{n+1}}{dt}\right) \tag{5.14}$$

Finally, Figure 5-1 better illustrates the information exchange between Aegir and the MATLAB code. The latter calculates the true state vector from Aegir's bare hull estimation.

5.3 Radiation Condition

Since the free-surface is finite in a numerical analysis, we need to force the outgoing waves to decay to zero at the borders. If we don't do that we could have undesirable numerical reflection, with waves bouncing back into the domain. Aegir achieves the radiation condition by placing an artificial beach on an area close to the borders,

$$\begin{aligned} \frac{d\psi}{dt} &= -\, g\eta \\ \frac{d\eta}{dt} &= \frac{d\psi}{dz} - 2\nu\eta + \frac{\nu^2}{g}\psi \end{aligned} \tag{5.15}$$

where ν is an artificial viscosity imposed on the waves for their decay near the edges.

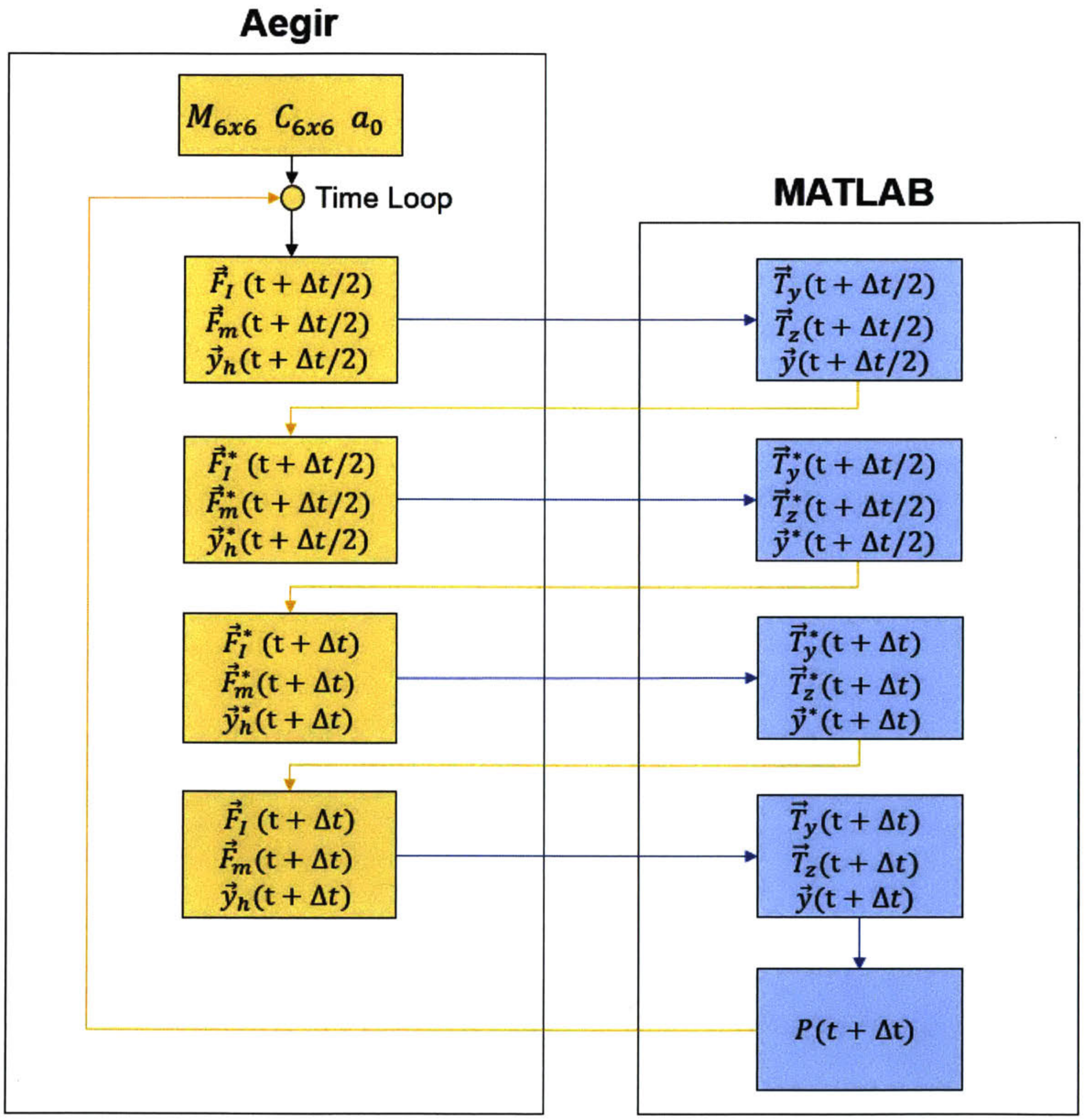

Figure 5-1: Schematics describing the information change between Aegir and the MATLAB code for each time-step. Where $\vec{F}_I(t)$ and $\vec{F}_m(t)$ are the incident and memory force vectors, respectively.

Chapter 6

Two Gyroscopes Case Study

In chapter 4 we outlined the physical model, making clear the main dynamics that govern hull, gyroscope and PTO. Then, in chapter 5, the numerical model was described, not only coupling the dynamics outlined previously, but also applying the appropriate time and spatial discretization of the governing equations.

We can now start to quantitatively evaluate the IOwec design outlined in chapter 3. We will start by defining the domain size, mesh density and time-step in a way to guarantee numerical accuracy and stability, while reducing computational costs. Then we will analyze the two gyroscope design case outlined in section 3.2. Chapter 7 follows with the simulation of the $1/50^{\text{th}}$ scale model and its comparison to the experiments undertaken in Davidson Laboratory, for the Wave Energy Prize.

Before starting, however, it is worth pointing out that all Aegir outputs are raw time-domain signals. Every related quantity had to be calculated from them and for that Fourier transform was used a number of times. The FFT algorithm was used for quick processing and its implementation, as well as other insights, are summarized in appendix C.

6.1 Sensibility Analysis

All the analyses carried out are done with monochromatic waves in head seas, with periods ranging from $5s$ to $12s$. The numerical simulation has to, therefore, be stable and accurate within that range. The dispersion relation outlined by equation 2.8 connects wave period with length, a metric which is easier to use to size the domain. Considering infinite depth, the wave lengths range from $39m$ to $225m$, the higher one driving the domain size. Time-step and mesh density must then be fine enough to perceive the $5s$ one.

6.1.1 Domain Size

The geometry was prepared using the CAD commercial package Rhinoceros, with the same full scale measures as reported in table 3.1. The IOwec was subdivided into NURBs surfaces with the correct orientation with respect to the incoming flow, with its surfaces extending above the free-surface. The linearized wave mechanics collapse the water surface to its mean level, making any piece of body surface extending after it virtually useless. That won't be the case, however, for the later nonlinear analysis, where Froude-Krylov forces will be calculated up to the actual deformed free-surface defined by equations 5.8 and 5.9. Figure 6-1 shows the final geometry utilized for the sensibility analyses.

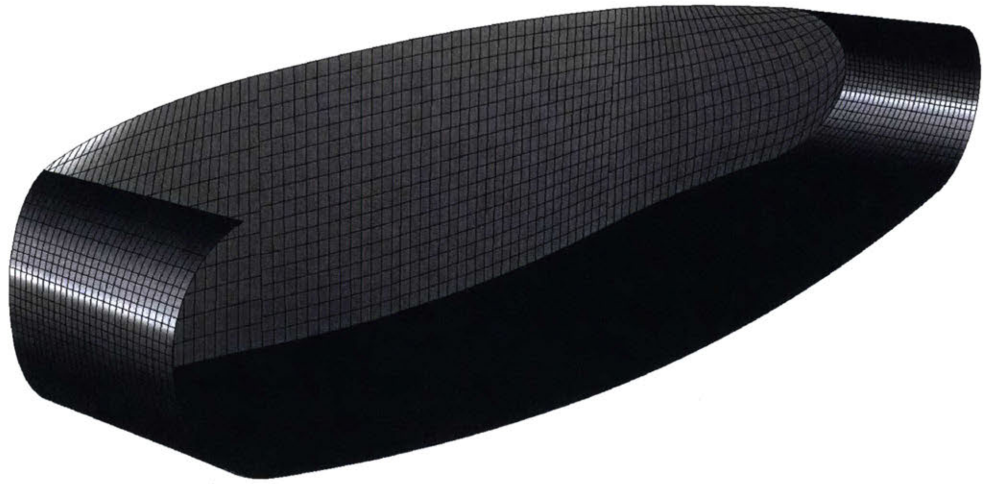

Figure 6-1: NURBS representation of the IOwec's hull.

The domain initial sizing was based on the model length and the longest wave to be simulated, which has a period of $12s$ and length $\lambda = 225m$. Table 6.1 presents the values used.

Table 6.1: Initial Domain Size.

Extent	**Direction**	**Reference**	**Value**	**Unit**
Domain	Upstream	λ	112.5	m
	Downstream	$-3 \cdot \lambda$	-337.5	m
	Side	3·L	135	m
Beach	Upstream	-	45	m
	Downstream	-	112.5	m
	Side	-	54	m

To be certain the domain was sized correctly, the longest wave ($T = 12s$) with amplitude $A = 1m$ was run for three domain multipliers of 1.0, 1.5 and 2.0 applied to all three distances. The pitch motion is plotted against the simulation time in Figure 6-2. For this run a $60s$ of Ramp Time and $0.1s$ time-step was used, which should be more than enough for the considered wave. Also, a simulation time of $150s$ was enough to achieve steady state motion. No noticeable difference was observed between the first two multipliers, while the last diverged in less than 0.2%. The domain size corresponding to the 1.5 multiplier was selected.

6.1.2 Mesh Density

Three mesh density factors were tested against the smallest wave: 0.5, 1.0 and 1.5, corresponding to panel sizes of $3.75m$ and $2.50m$ and $1.25m$, respectively. For this run, the same ramp and time-step inputs presented in section 6.1.1 were used. Figure 6-3 shows the IOwec's pitch motion plotted against the simulation time, it can be seen that the coarse mesh, with $3.75m$ panel size, yielded results which diverged about 2.36% from the finest one. Since no noticeable difference was observed between the two finest meshes, the $2.5m$ panel width was chosen for subsequent runs.

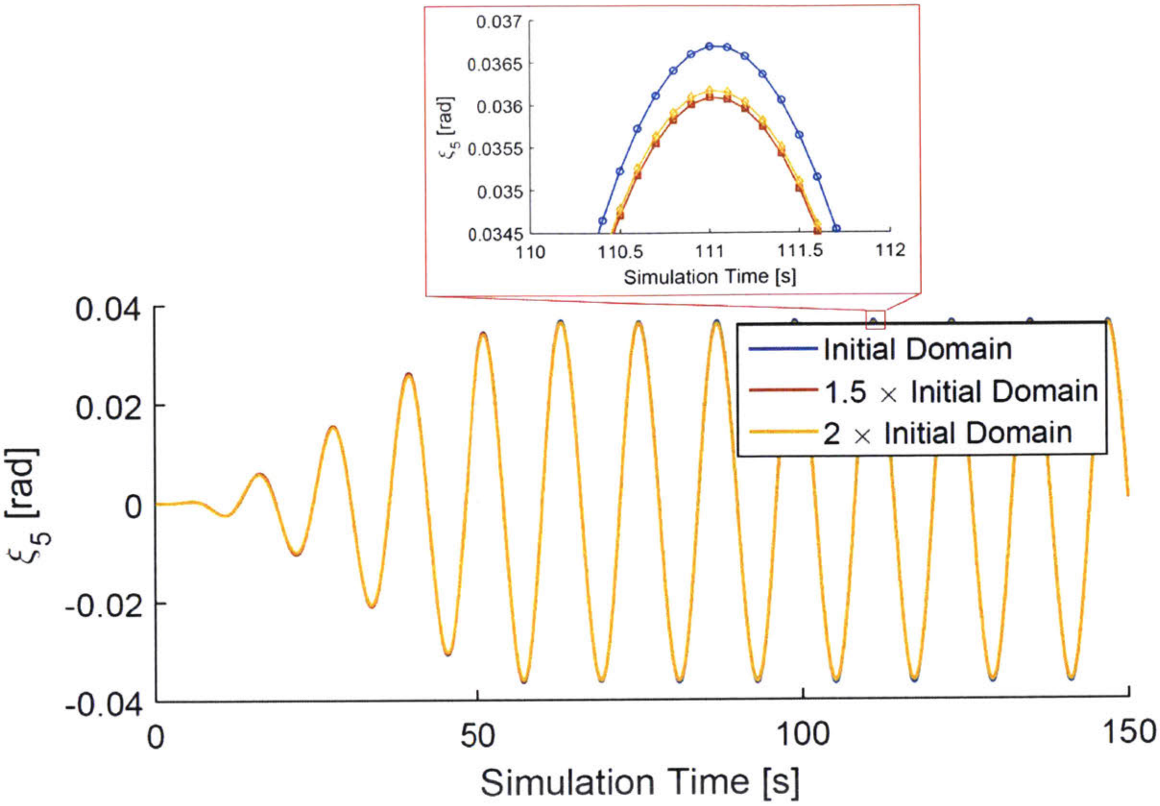

Figure 6-2: Domain Sensitivity Analysis.

6.1.3 Time Step

The simulation time-step had to be chosen to accurately solve the smallest wave period. To select a proper step, four values were tested while simulating the $T = 5s$ wave: $0.05s$, $0.1s$, $0.2s$ and $0.5s$. Figure 6-4 shows the pitch motion versus simulation time for each time-step, with the exception of $0.5s$ which diverged. It was observed that the least fine step, $0.2s$, showed a deviation of about 0.35% from the $0.05s$ one and was, therefore, was chosen for the subsequent runs.

Finally, table 6.2 shows all the best domain, mesh and time inputs based on the sensibility analyses carried. Figure 6-5 shows the final domain, with the free-surface and body meshing.

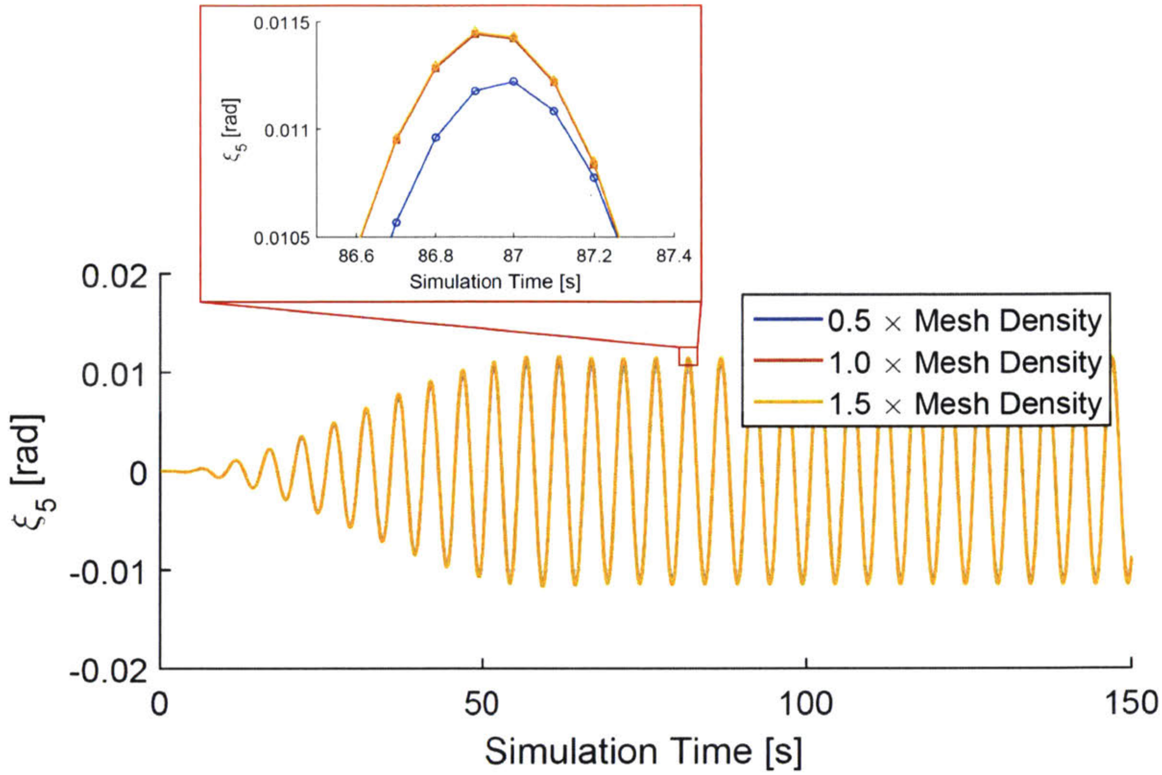

Figure 6-3: Free-Surface Mesh Sensitivity Analysis.

Table 6.2: Final Domain Size.

Extent	**Direction**	**Reference**	**Value**	**Unit**
Domain	Upstream	$1.5 \cdot \lambda$	168.75	m
	Downstream	$-4.5 \cdot \lambda$	−506.25	m
	Side	$4.5 \cdot L$	202.5	m
Beach	Upstream	-	67.5	m
	Downstream	-	202.5	m
	Side	-	81	m
Time	Ramp Time	-	60	s
	Time-step	-	0.2	s

6.2 Bare Hull Motion

Before assessing the gyroscope dynamics and power extraction we will take a look into the hull's bare motion. This will serve as a sanity check against WAMIT results.

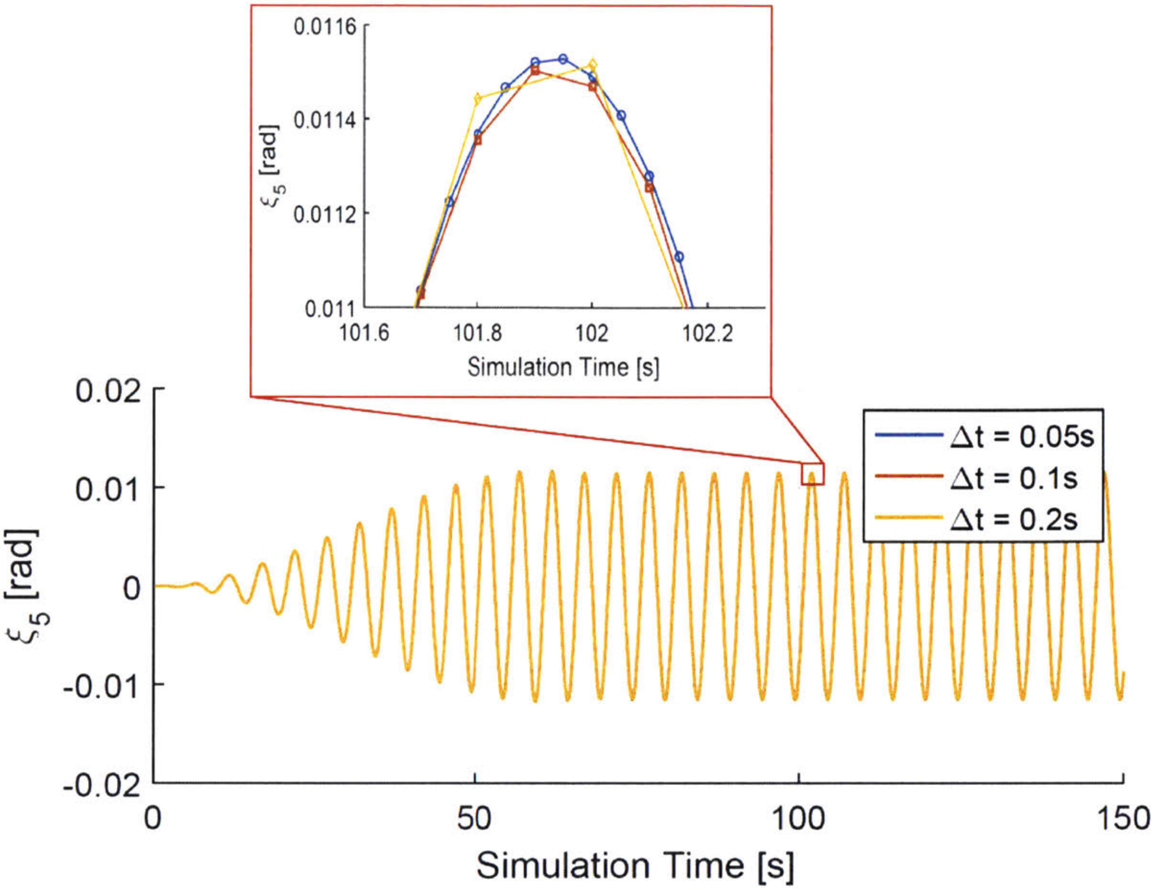

Figure 6-4: Time-Step Sensitivity Analysis.

The inputs were defined earlier in tables 3.1 and 6.2. Figures 6-6 and 6-7 show the heave and pitch RAO, respectively. The former has an excellent agreement, while the latter is just slightly off at the resonant peak.

It is easier to assess the accuracy of Aegir's pitch RAO by bringing the time-domain problem into the frequency-domain. As stated in section 2.3, WAMIT solves the radiation potential and, through equations 2.35 and 2.36, calculate the added-mass, damping and exciting forces. To be able to represent such quantities with Aegir we will need to borrow the abstract thinking of classical seakeeping, which explain the motion by exploiting its linearity and decomposing it into the radiation and diffraction problem. Starting with the latter, let's imagine the IOwec fixed while the incident waves hit the hull, diffracting. The integration of the pressure over the hull will yield the classical exciting force (i.e. Froude-Krylov plus diffraction forces). Figures 6-8

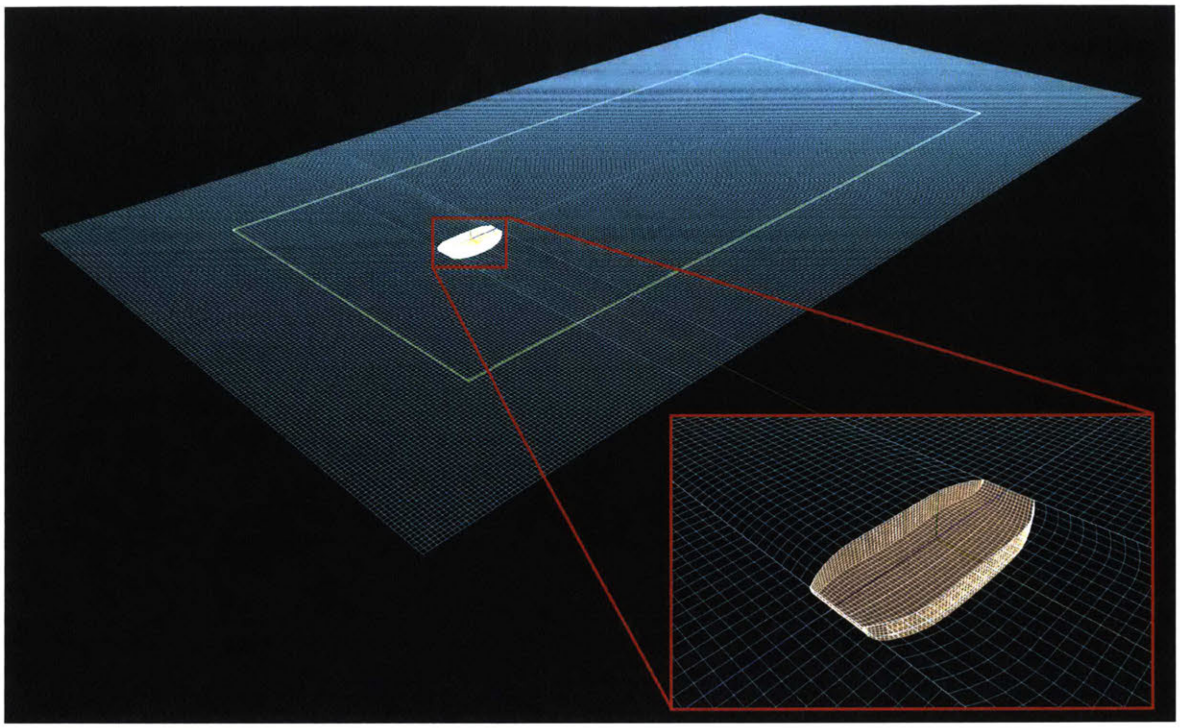

Figure 6-5: Final domain and meshing.

and 6-9 show the comparison between Aegir and WAMIT exciting force and moment. This problem was well modeled and didn't show any meaningful discrepancy between both methods (the incident pressure integration is being performed correctly).

Now, instead of having the body fixed, we will oscillate it under a prescribed motion of amplitude A and frequency ω on an undisturbed free surface. The hull will generate outgoing waves whose, pressure, when integrated on the hull, describes a force out of phase with the motion. This "lag" between motion and force allows us to break the latter into a component in phase with the acceleration (i.e. added-mass) and another in phase with the velocity (i.e. damping). Both coefficients can be calculated by knowing the force signals magnitude and phase with respect to the motion. The diagonal elements are,

$$a_{ii} = \frac{X_i \cos\left(\epsilon_f - \epsilon_m\right)}{\Xi_i \omega^2} \tag{6.1}$$

$$b_{ii} = -\frac{X_i \sin\left(\epsilon_f - \epsilon_m\right)}{\Xi_i \omega} \tag{6.2}$$

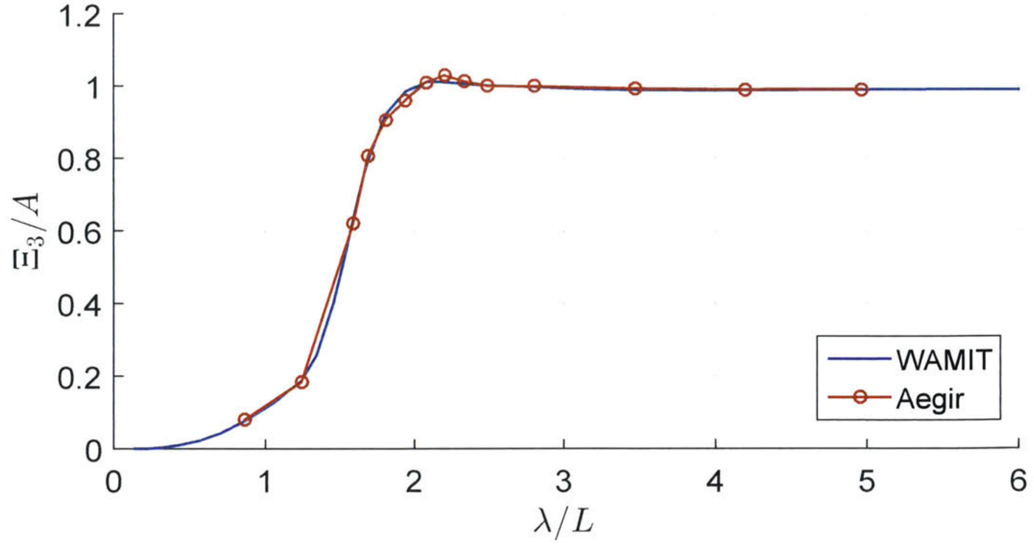

Figure 6-6: Heave RAO comparison between WAMIT and Aegir for the bare hull case (i.e. no gyroscope).

Figures 6-10 *a*) through *d*) show both Aegir and WAMIT added-mass and damping coefficients for heave and pitch. We can see an excellent agreement for the former, while pitch presents higher damping at resonance and a slight offset on the added-mass for λ/L starting at 3. This means the memory potential in Aegir, which accounts for the radiation problem, yields a slightly different solution than WAMIT. The extra damping may explain why the pitch RAO peak is a bit smaller for Aegir.

Both DoF considered are in excellent agreement between WAMIT and Aegir. We are now safe to proceed with the implementation of the gyroscope and PTO mechanics outlined in chapter 4.

6.3 Gyroscope Spin Sensibility

The hull has guaranteed pitch resonance at $T_p = 8s$ as required by the predominant sea at the coast of Oregon. The first step after that is to use equation 4.36 to size our PTO spring. Ideally, we would need to specify a value for each incoming wave frequency, but at this time we will only consider hull resonance. The reactive control constant becomes,

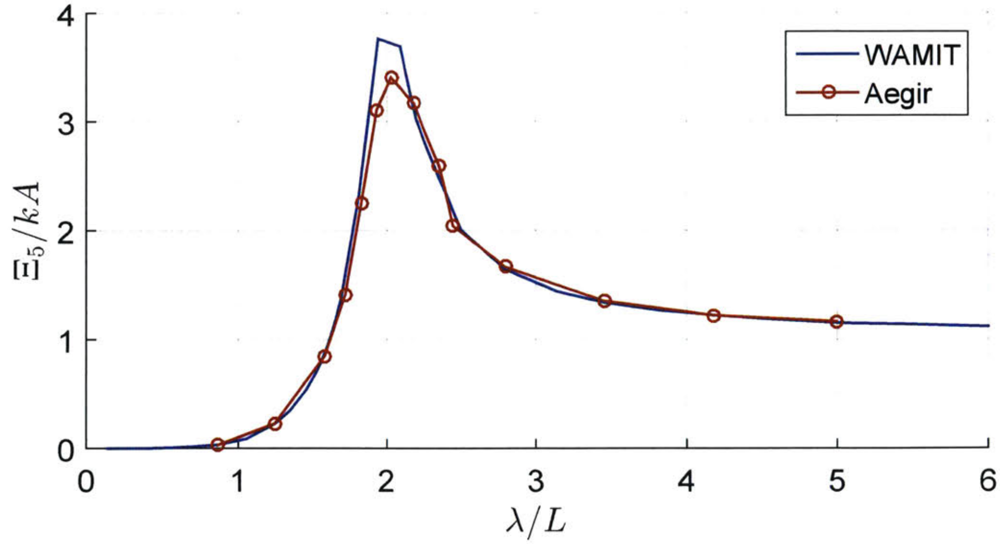

Figure 6-7: Pitch RAO comparison between WAMIT and Aegir for the bare hull case (i.e. no gyroscope).

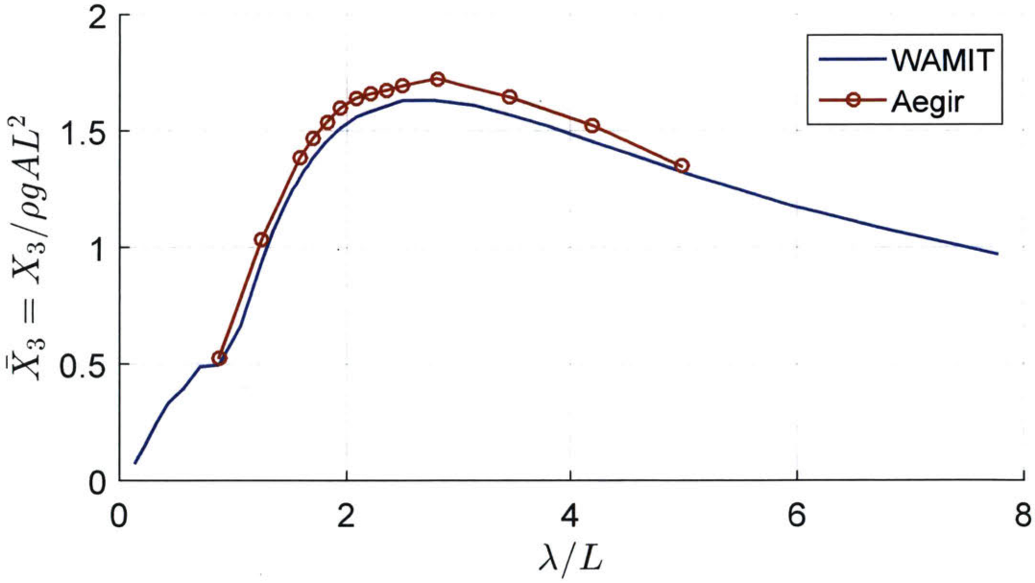

Figure 6-8: Heave scattering force coefficient.

$$k_l = I_x \cdot \omega_n^2 \simeq 604,921.50 \frac{kg \cdot m^2}{s^2} \tag{6.3}$$

As stated before, what matters for this system is the angular velocity $J\varphi$. The inertia is prescribed by table 3.3. The base spin rate was defined by relation 3.4. We

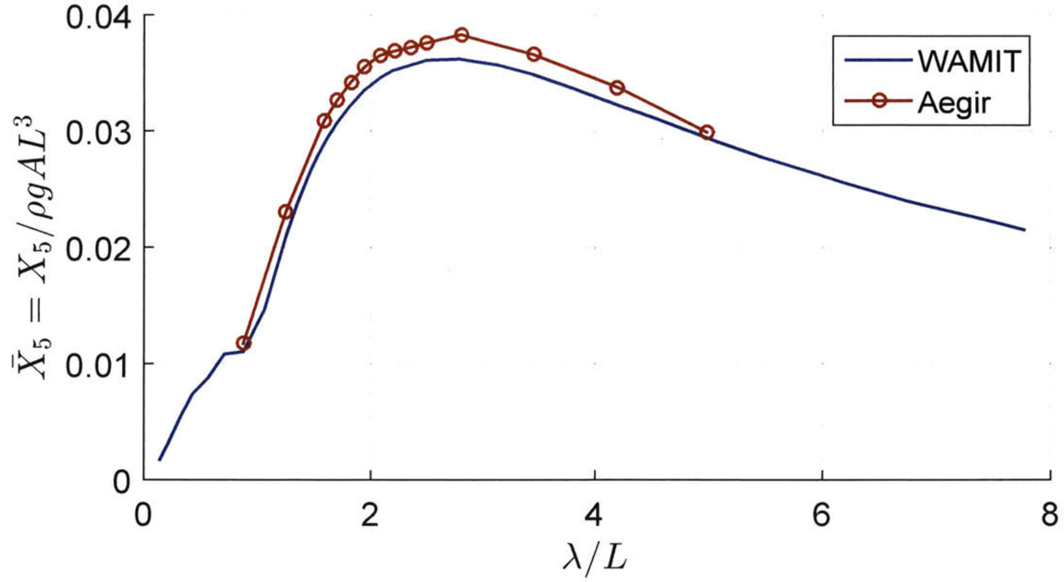

Figure 6-9: Pitch scattering moment coefficient.

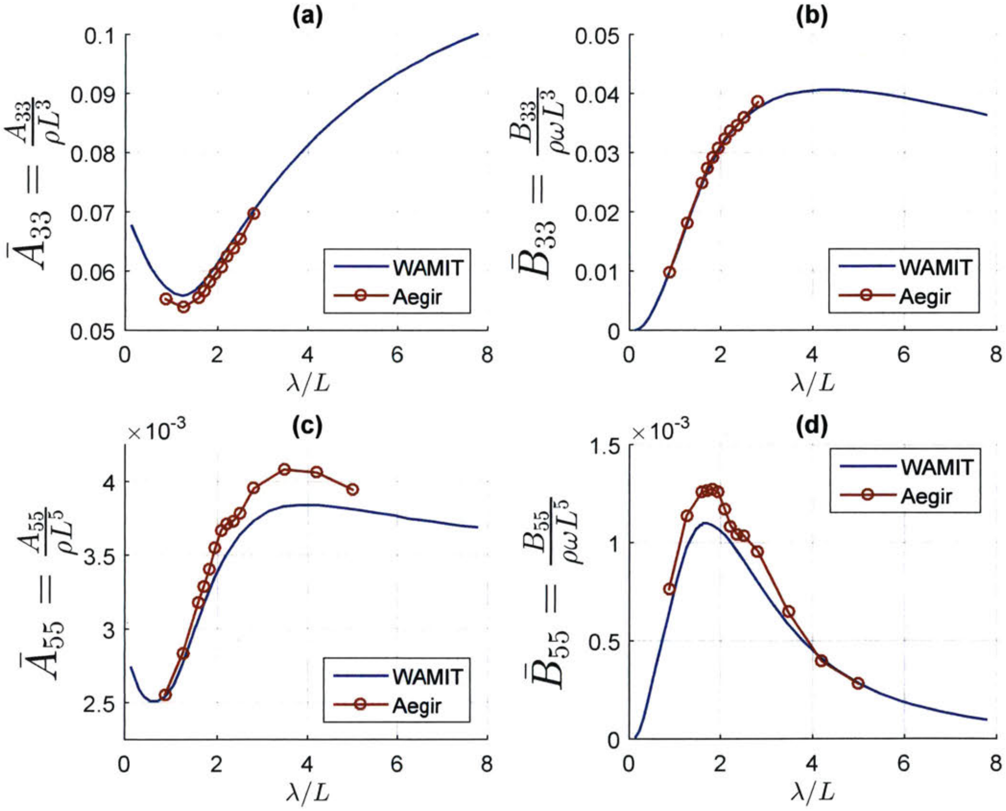

Figure 6-10: a) Heave added-mass coefficient; b) Heave damping coefficient; c) Pitch added-mass coefficient; d) Pitch damping coefficient.

still don't know the appropriate PTO damping, so equation 4.42, which only uses hull pitch and gyroscope roll amplitudes, will be utilized to estimate the averaged power extraction over one wave period. Figure 6-11 shows such power by different multipliers of the base spin rate.

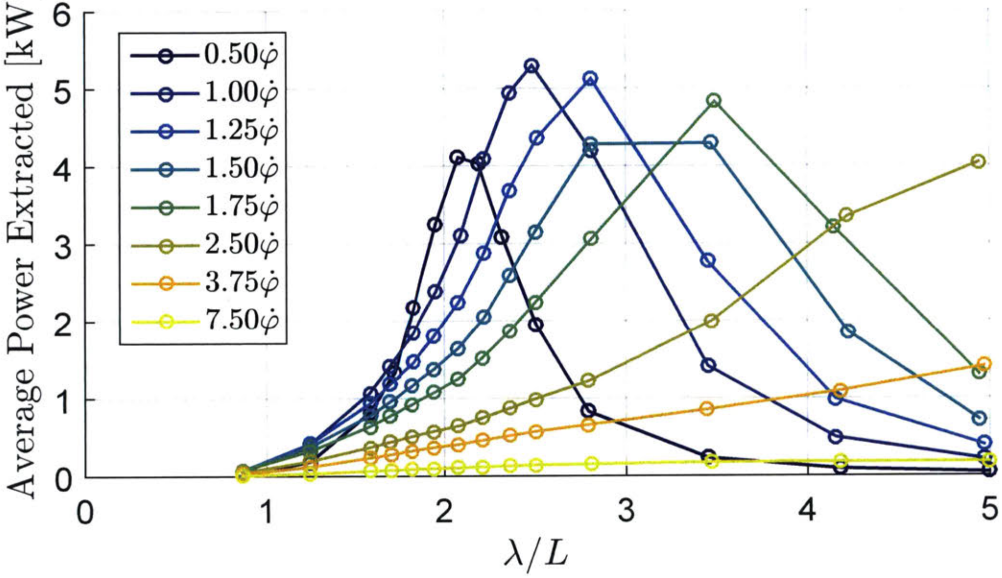

Figure 6-11: Average power extracted for different multiples of the base spin rate. This is estimated through equation 4.42, since we still don't know the appropriate PTO damping. The waves have amplitude of $0.1m$.

We can notice that, starting from low spin rates, the power extracted increases until an optimum value. After that the peak extraction moves to longer waves, until it is not noticeable within the selected wave bandwidth. Increasing the flywheel spin makes the system stiffer, moving the hull's natural frequency towards longer waves, as can be seen in Figure 6-12.

The best spin found, considering operation in the Oregon sea, is $1.25\dot{\varphi}$ (i.e. 150 RPM). This rate will be used for the subsequent runs.

6.4 PTO Damping Sensibility

Maintaining the same PTO spring, optimized for the hull natural frequency, and with the chosen spin rate, we can do a sensibility analysis with the PTO damping.

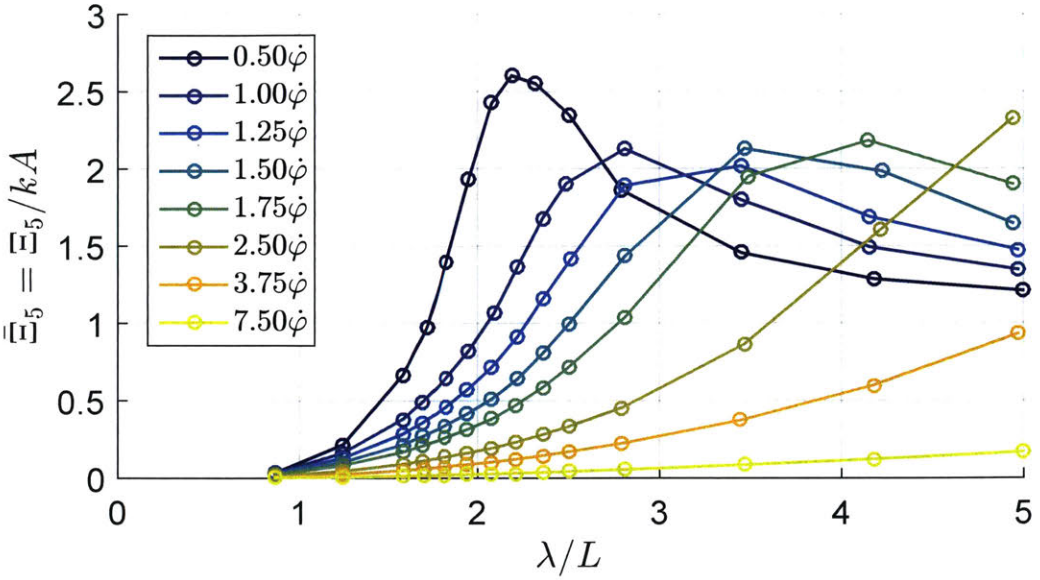

Figure 6-12: Pitch RAO for different multipliers of the basis spin rate. We can see a shift in the natural frequency towards longer waves as the spin is increased and the system gets stiffer.

Equation 4.39 can be utilized, using the power predicted during the spin analysis, to estimate the required damping.

$$c_l = \frac{2\bar{P}_E(\omega)}{\omega^2\Theta^2} \simeq 455,667.00 \quad kg \cdot m^2/s \tag{6.4}$$

This time around we can actually calculate the average power extraction over one wave period through the instantaneous power signal. For that equation 4.38 is used. We can observe, from figure 6-13, a shift of the peak energy extracted towards smaller waves as the damping is increased, due to the decrease of gyroscopic roll. An optimum damping of $5c_l$ is attained, after which the device quickly loses energy extraction efficiency, especially for longer waves.

The effects of damping are evident on the hull's pitch as well. The optimum damping guarantees that its natural frequency remains at $8s$, while minimizing the motion as much as possible. Figure 6-14 shows how the pitch RAO changes for all the damping variation.

Reporting power extracted by itself is not a good representation of the IOwec's

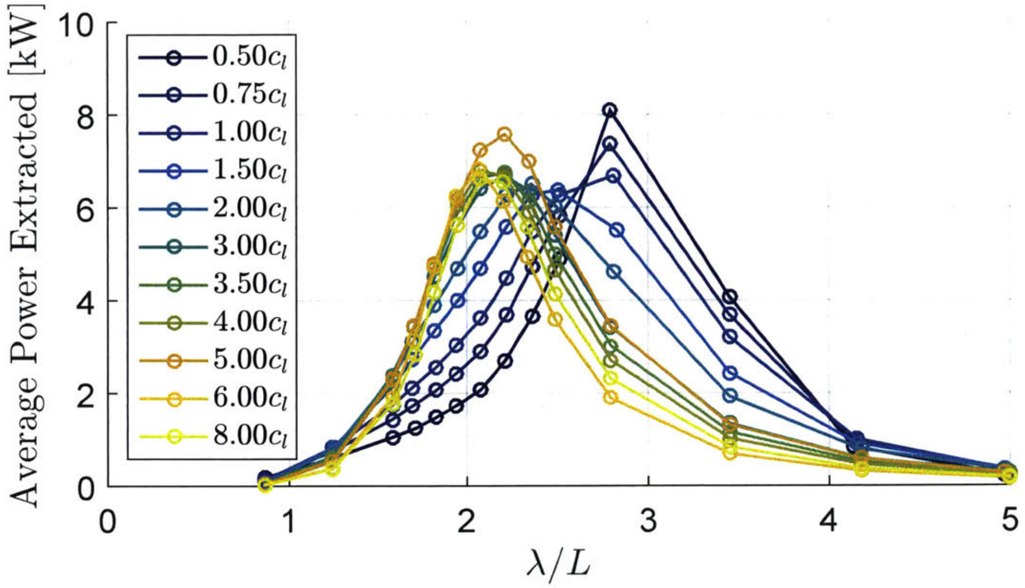

Figure 6-13: Average power extracted over one wave period. The optimum damping identified is $2c_l$, after which the device quickly loses efficiency for longer lengths. All waves have amplitude of $0.1m$.

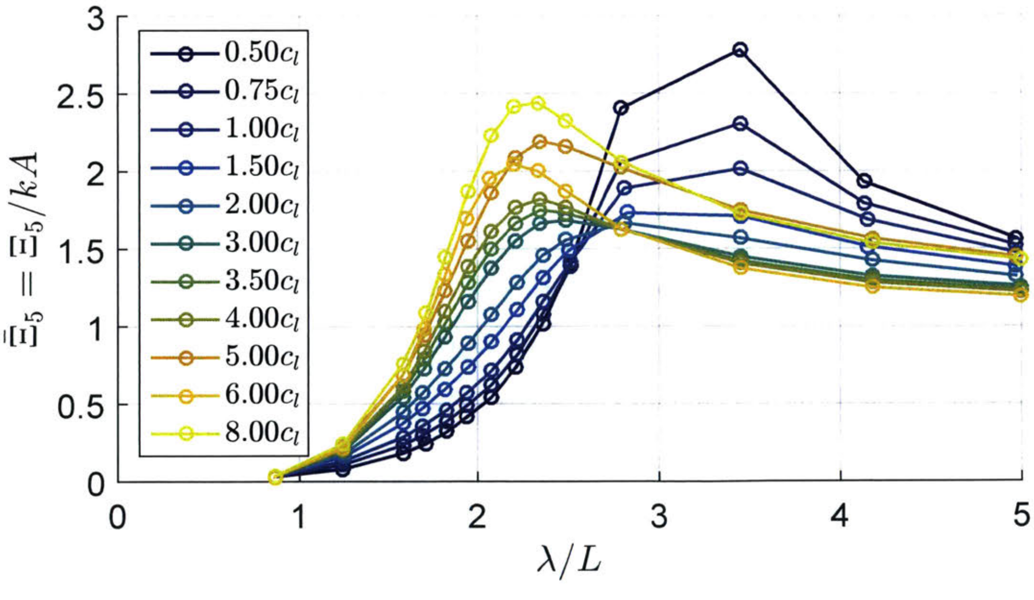

Figure 6-14: Pitch RAO for all the damping values considered. We can see the optimal damping of $2c_l$ tries to minimize the motion throughout all wave lengths, while still retaining the natural frequency at $8s$.

capabilities, especially since it varies with the wave amplitude. A better way to quantify efficiency is to plot the capture width, which is the ratio between the average powers extracted and incoming from a 2D section of the wave profile.

$$C_W = \frac{\bar{P_E}(t)}{\bar{\mathfrak{F}}} = \frac{32\pi}{\rho g^2 T^2 H^2} \int_t^{t+T} P(t)dt \tag{6.5}$$

Figure 6-15 shows the IOwec is capable to, at resonance, extract a monochromatic wave $25m$ wide, 1.25 times its beam.

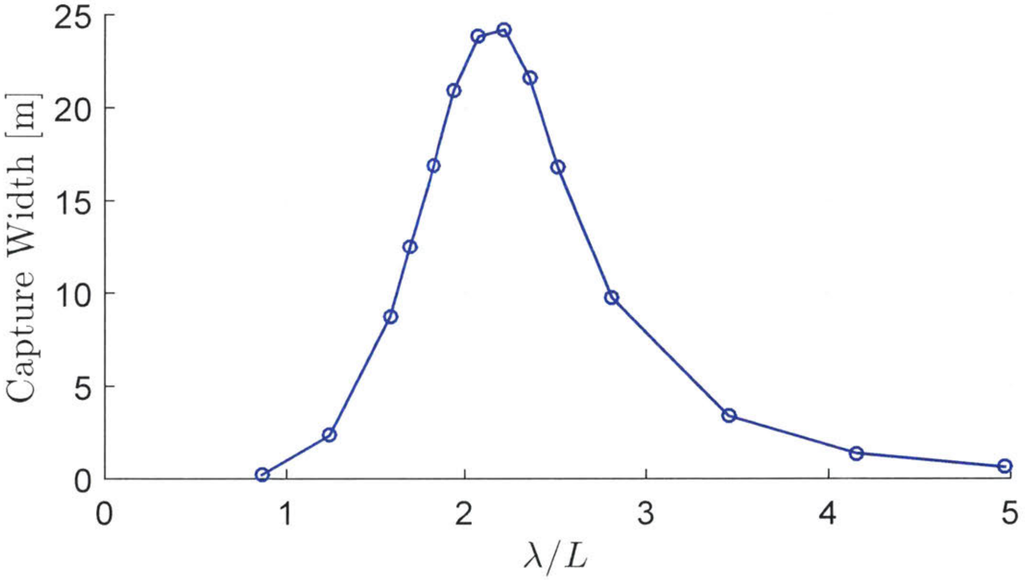

Figure 6-15: Capture width of the IOwec. The device is able to, at resonance, extract a wave equivalent to 1.25 its beam.

The yaw torque induced by both counter-rotating flywheels is seen to cancel one another. Figure 6-16 shows the torques from both gyroscopes for the $T = 8s$ wave, with frequency exactly twice that of the wave.

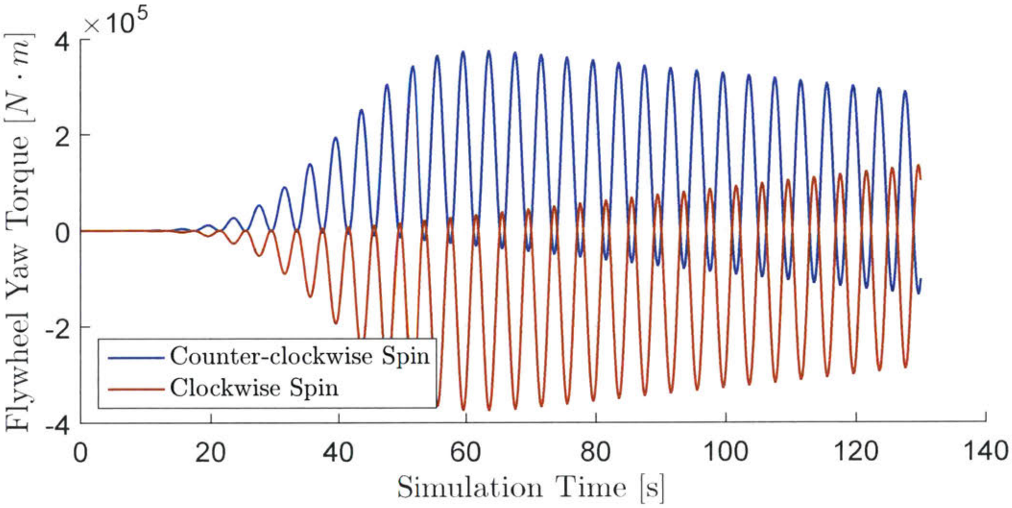

Figure 6-16: Yaw torque from both counter-rotating gyroscopes for the $T = 8s$ wave. Their summation goes perfectly to zero, and the frequency is exactly twice that of the wave.

Chapter 7

$1/50^{\text{th}}$ Experimental Model Testing

As part of the Wave Energy Prize, a $1/50^{\text{th}}$ scale model test of the IOwec was tested at the Davidson Laboratory, part of the Stevens Institute of Technology. The model dimensions are summarized in table 3.4.

7.1 Test Setup

Davidson's wave tank is $95.4m$ long, $5m$ wide and $1.97m$ deep. Seven monochromatic waves were demanded by the prize judges, ranging, in full scale, from $6s$ to $15s$. This means the longer waves are in the shallow water regime, which demands special attention when running the numerical model. Table 7.1 states the waves considered, as well as the height and depth condition, all head-seas.

The two most important quantities to be measured are torque and angular velocity of the gyroscope shaft. The first was captured by a LCMFD Omega load cell, which supplies a signal with varying voltage proportional to the torque. The second was captured by a Bourns AMS22S analog encoder, which supplies voltage proportional to the shaft's angular velocity.

The flywheel was spun by a Allied Motion CL 29 Series DC motor. The rotation rate was controlled by an Arduino motor shield speed and measured by a XS6 M8 inductive sensor. It was observed, during the tests, that the DC motor was undersized for the flywheel inertia, causing small variations of the spin during experiments. The

Table 7.1: Monochromatic waves tested for the Wave Energy Prize in model scale

Index	**Period**	**Length**	**Height**	**Depth Condition**
[−]	[s]	[m]	[m]	[−]
M1	0.85	1.11	0.0098	Deep Water
M2	1.06	1.75	0.0214	Deep Water
M3	1.27	2.51	0.0371	Deep Water
M4	1.48	3.46	0.0414	Deep Water
M5	1.70	4.51	0.0597	Intermediate Depth
M6	1.91	5.58	0.0694	Shallow Water
M7	2.12	6.75	0.0901	Shallow Water

mean spin was reported and used for the comparative numerical simulations to come. Figure 7-1 shows the variation of the spin along the acquisition of the sensor.

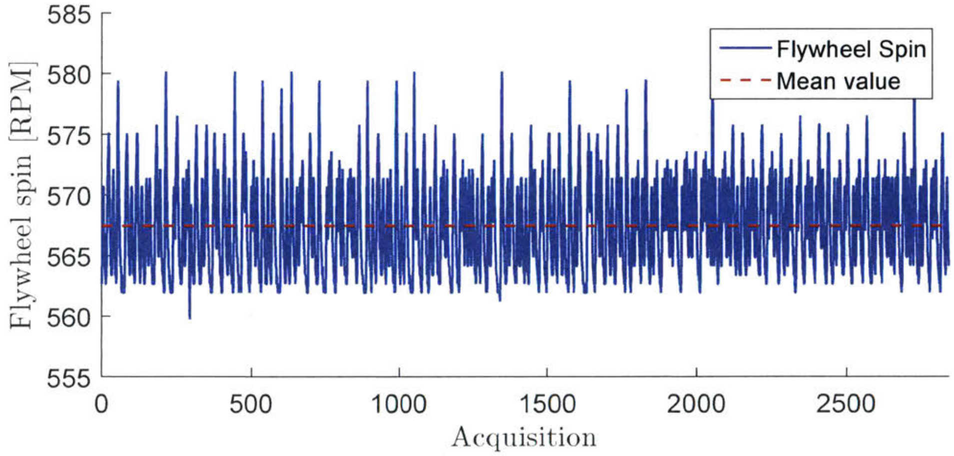

Figure 7-1: Flywheel spin variation during the M4 wave period. The mean is 567.4RPM.

Regarding the hull, oscillation in all 6 DoF was measured by a motion tracking device. It is composed of two cameras capable of capturing infrared frequencies reflected by spheres placed on the hull. The mooring system consisted of a cable running from the bow to a weight, which ran through a second cable to a submerged buoy (Fig. 7-2).

A wave probe was positioned ahead of the device, far enough to measure the incident wave train without disturbance from the body radiated waves or diffraction. These values were used to calculate the actual wave frequency and height, which were used in the analysis.

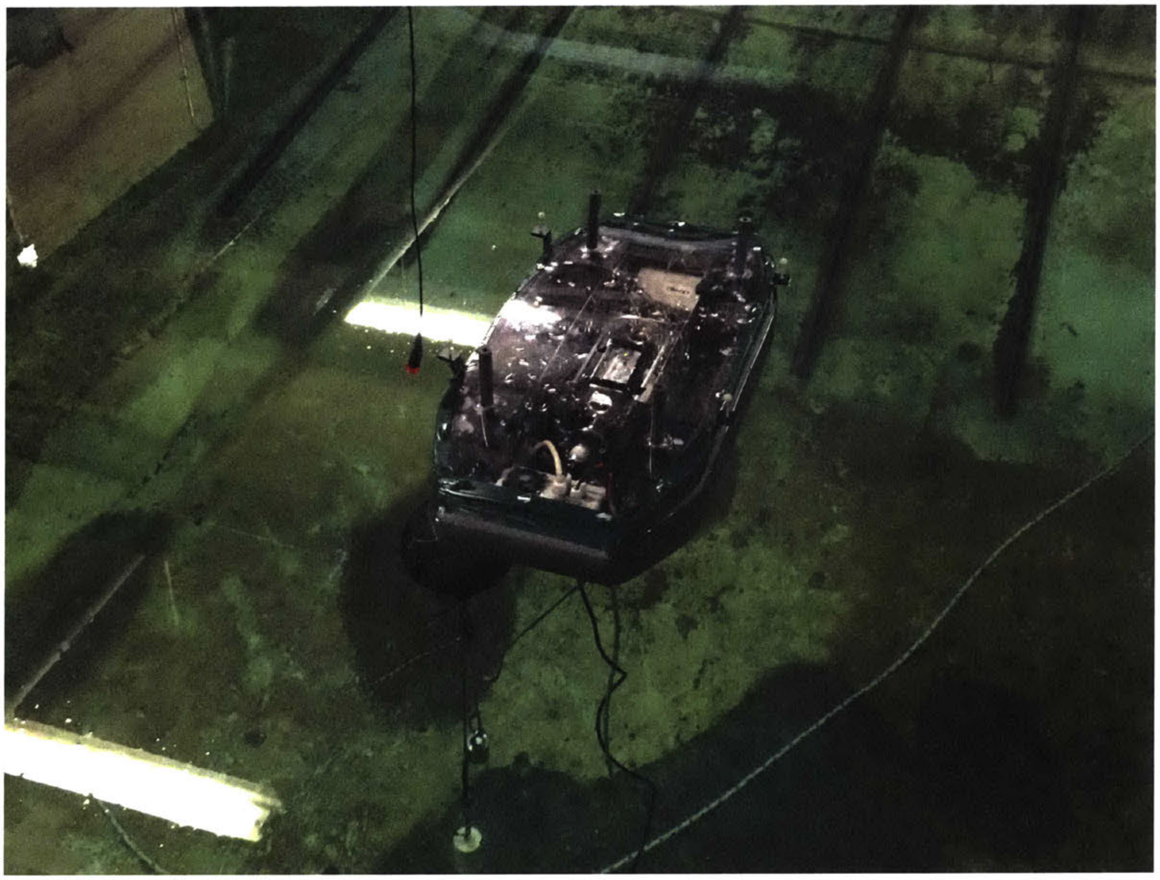

Figure 7-2: IOwec's $1/50^{\text{th}}$ scale model positioned in Davidson's Laboratory wave tank. The mooring buoy and weight can be seen beneath the water, as well as the flywheel under the acrylic screen.

7.2 Results

Despite our participation during the experiments, the post-processing was done by the testing facility to guarantee transparency on the submitted data. The final values of motion amplitude, PTO damping and power extracted were release to us after the examination. The damping coefficient was estimated through a linear correlation between measure shaft torque and angular velocity.

If the coefficient is expected to be linear, than a line fit should yield the desired damping as its derivative. However, during experiments, the torque sensors were seen to introduce a frictional damping, as it gripped the shaft. In fact, we could observe the gyroscope locking in position for frequencies outside the resonance, showing it was unable to win this coulomb damping. Figure 7-3 shows the correlation between torque and angular velocity for the M4 wave. Particularly for monochromatic waves, the WEP judges considered only the points of maximum angular velocity and its corresponding torque, so as to minimize the system's inertial effects influence on the measurements. Table 7.2 presents all PTO damping coefficients and flywheel spin reported.

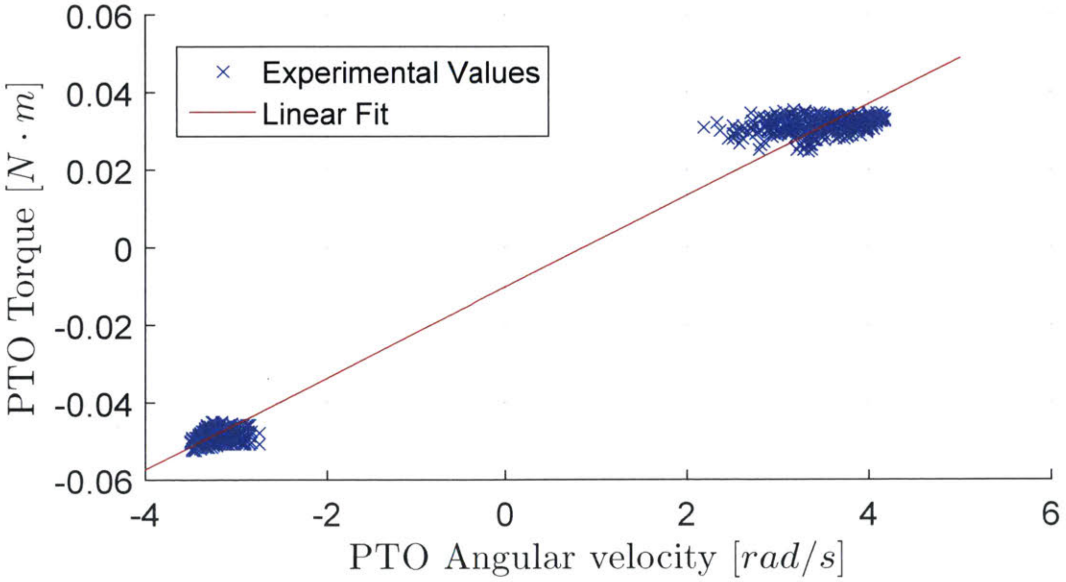

Figure 7-3: PTO damping for the M4 wave measured through the correlation between PTO torque and angular velocity. The line fit derivative yields the desired coefficient.

The motion amplitude was calculated by averaging the steady state response peaks. Figure 7-4 gives an example of the pitch motion after transient effects die out.

Finally, figures 7-5 and 7-6 show the heave and pitch RAO, respectively. The former showed what seems to be a resonant peak which was not observed in Aegir (or WAMIT, as shown earlier in figure 6-6). The motion, however, quickly approaches the numerical solution at the long wave limit.

Table 7.2: Flywheel spin and PTO damping reported for each monochromatic wave studied.

Index $[-]$	**Flywheel Spin** $[RPM]$	**PTO Damping** $[m]$
M1	480.1	0.1263
M2	314.7	0.0316
M3	468.4	0.0199
M4	567.4	0.0118
M5	464.0	0.0556
M6	538.5	0.0715
M7	524.2	0.0569

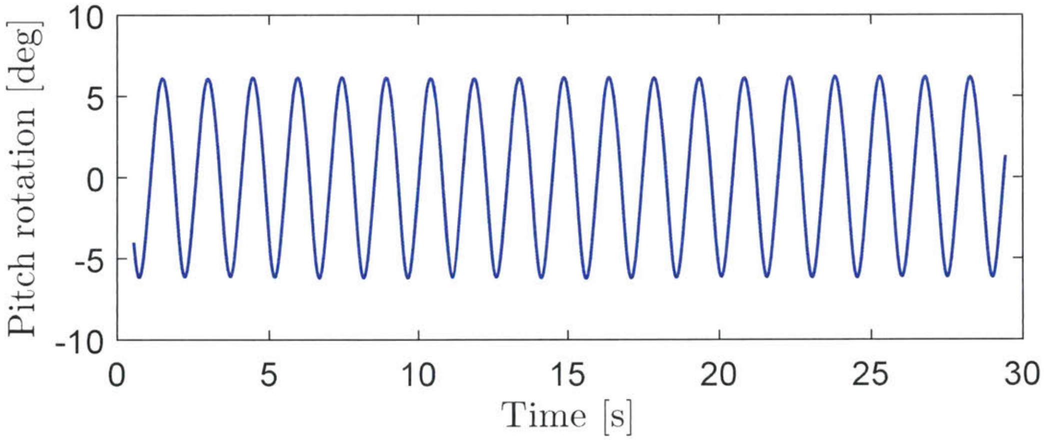

Figure 7-4: Steady state pitch motion for the M4 wave. The motion amplitude was estimated by averaging the peaks of each oscillation.

Numerical solution for pitch, on the other hand, seems better than heave, matching the experiments everywhere but close to resonance. The numerics never consider viscous effects, which will introduce some extra damping. Considering the fairness of the hull, bow and stern symmetry and nonexistence of sharp curvatures leads to believe that most of the viscous damping comes from friction rather than pressure effects.

Aegir's pitch RAO curves alone tell us another thing. Adding the PTO damping to the simulations barely change the hull motion. This most likely means that such damping is either too low or too high - probably the latter, due to the aforementioned coulomb damping introduced by the shaft velocity sensor - indicating an inefficient power absorption.

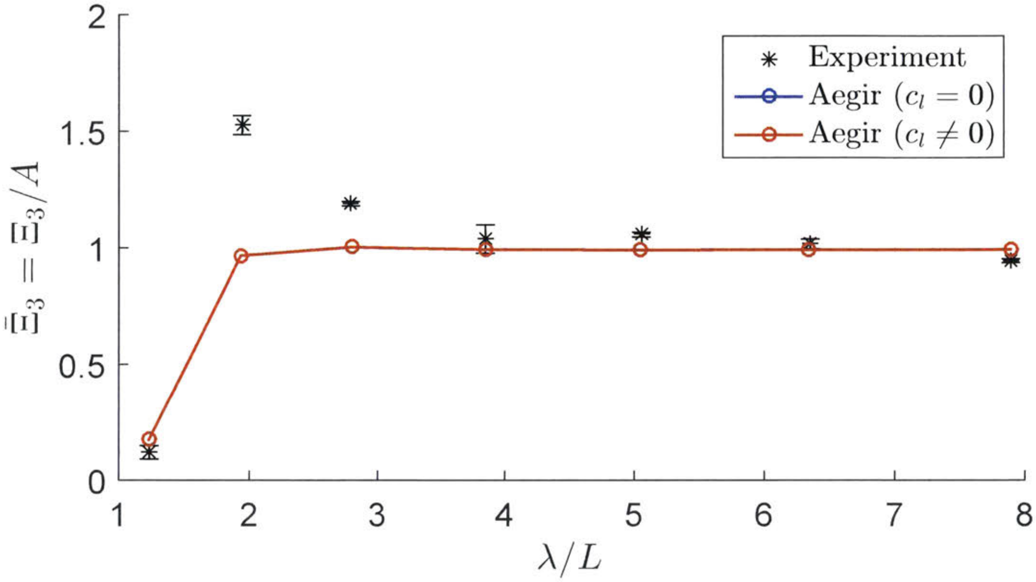

Figure 7-5: Heave RAO comparison between Aegir and scale model test measurements.

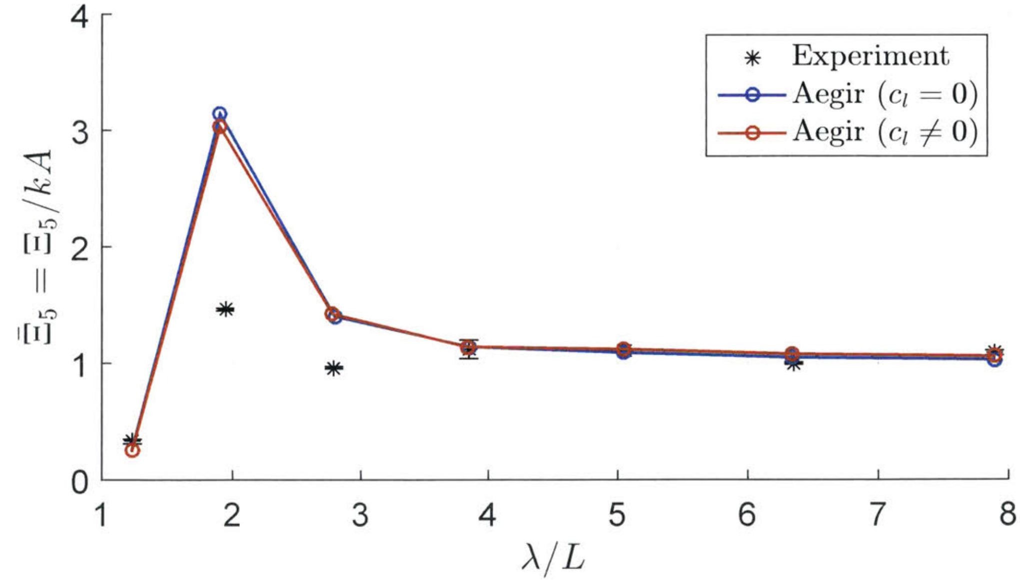

Figure 7-6: Pitch RAO comparison between Aegir and scale model test measurements.

Besides fluid friction, two other factors contribute to the differences in both pitch and heave motion. The first is the mooring system. It the mass which maintains the cables under tension was deemed too heavy early on and replaced by another, lighter, but still significant, which was also observed to enter in a harmonic swinging motion during tests. Such swing of the mooring mass might explain the slower oscillation perceived in the yaw motion induced by the gyroscope (Fig. 7-7). Also, the cable connecting to the mooring mass was placed on the bow, creating an artificial pitch moment.

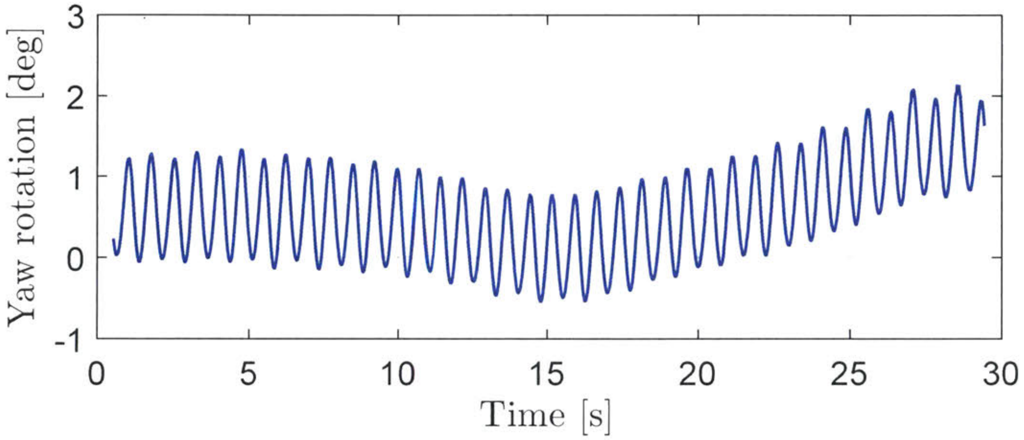

Figure 7-7: Yaw motion captured during the same time interval as the steady pitch motion shown in figure 7-4. We notice two superposed patterns, of low and high frequency. The high frequency oscillation is induced by the gyroscope, since it is exactly twice the incoming wave frequency. The low frequency is probably caused by the lateral swing of the mooring mass.

The second factor was the occurrence of green water, i.e. water on the deck, which happens due to the tapering on the bow and stern top. This phenomenon is not captured by Aegir, and affects both translational and rotational motions. Figures 7-8a and 7-8b show two moments of the IOwec motion under resonance, first a bow displaced high up, followed by the plunging, with the green water effect.

The average power extracted was calculated, for the experiments, through the product of torque and shaft angular velocity measured by the sensors. The numerical model, on the other hand, gives us the instantaneous power signal, which we can integrate and average over one wave period. By dividing both by equation 2.14 we get the capture width as in relation 6.5, which states the width of the wave

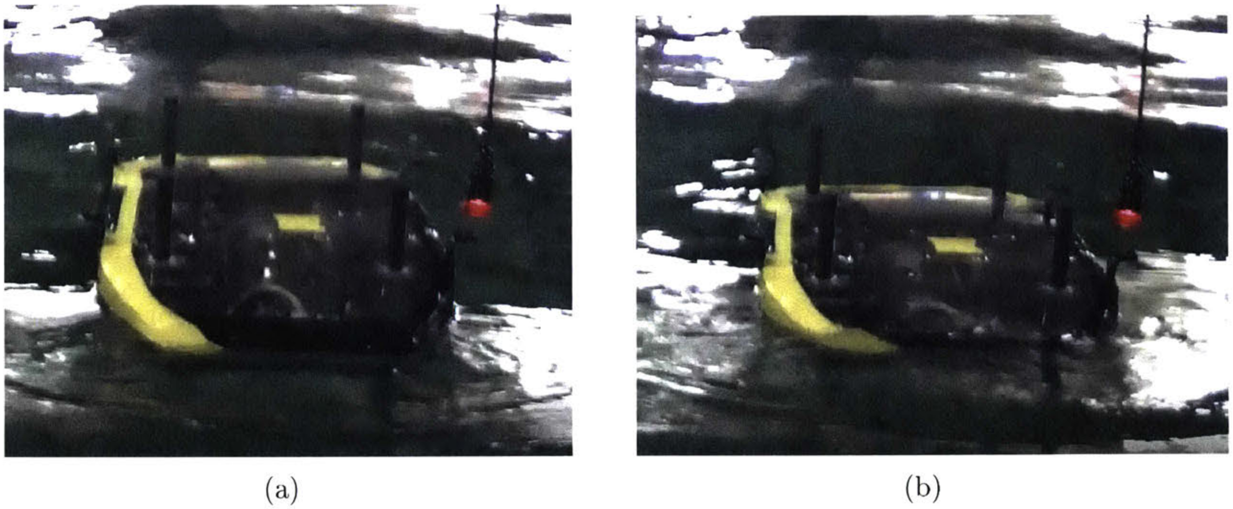

(a) (b)

Figure 7-8: a) Bow view of the IOwec, on the moment of largest negative pitch; b) The same view, right after the bow plunging into the water, showing the green water effect.

train carrying the energy captured. Figure 7-9 shows the capture width, in full scale for both experimental and numerical tests. We can see how inefficient this model is, probably due to the combination of poorly chosen spin and bad PTO damping, especially when comparing to the study case shown in figure 6-15.

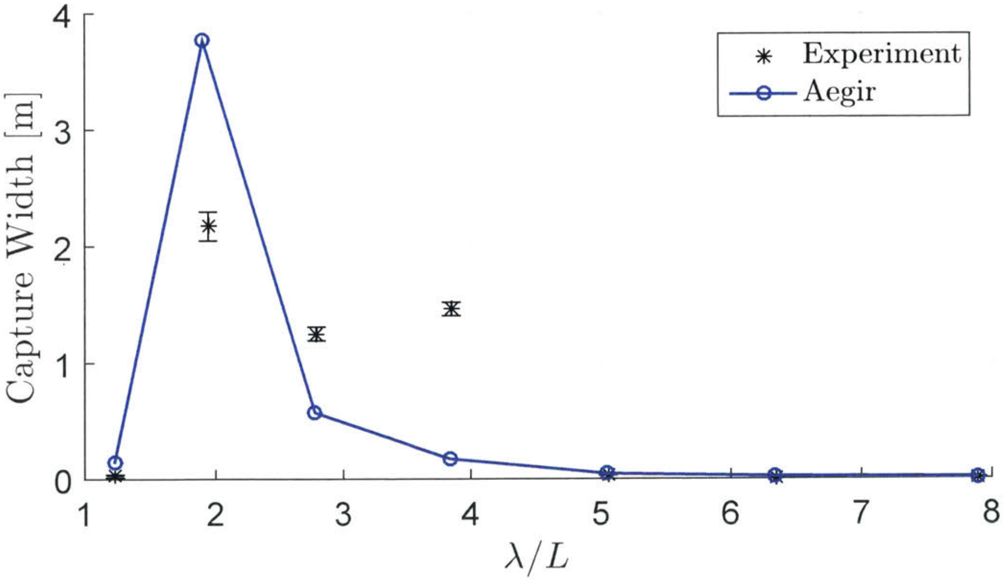

Figure 7-9: Capture width comparison, at full scale, between Aegir and experimental data.

Chapter 8

Conclusion

After certifying excellent agreement between WAMIT and Aegir heave and pitch RAO, the dynamics of the gyroscopes and Power Take-Off were successfully implemented. The MATLAB code managed, as expected, to use the time-domain panel method as a force block, correcting its output to account for the external dynamics at every time-step. Using Aegir's motion predictions, we were able to keep all terms from the gyroscope equations of motion.

The test case with two gyroscopes presented in chapter 6 showed how such system does have an optimum PTO damping and flywheel spin rate. A designer resorting to the developed code could, very early on, find the best configuration for his device. In fact, this could be extended to consider other mechanics for energy extraction such as pendulums, masses free to rotate in more than one DoF, etc. It was also shown how two counter-rotating gyroscopes can eliminate the negative effects of yaw torque, while doubling the pitch influence, as well as power extraction.

Aegir's use for this design exercise was justified by its capabilities of solving the deformed free-surface and extension to nonlinear effects. However, performing calculations with incident and restoring pressure integration up to the deformed free-surface yields strange results. For one, the exciting forces divided by the wave amplitude are always larger for the nonlinear case. The motion also shifts by exactly -90^o with no apparent explanation. Nonlinear body boundary condition could never be fully tested for different wave periods and amplitudes, due to its high computational demands from re-meshing at every time-step, which eliminates the advantage of using a panel method for early design.

Experiments performed for the Wave Energy Prize, although limited to the rules of the competition, allowed us to attempt a validation of the proposed model. Both pitch and heave RAOs have the same trend as the experimental points, but disagree on their magnitude close to resonance. The capture width for the experiments showed two outliers generating more energy than predicted by the panel method, which is not possible. New tests are needed, with better torque sensors to eliminate the frictional damping exerted on the shaft and with repeatability of the results. The mooring should also be redesigned, as it was seen to influence the hull motion considerably.

Future work must concentrate on understanding and correcting the nonlinear calculations. Also, better PTO control techniques should be investigated, the linear spring-damper used, for example, could have its value varying over different wave periods.

Regarding the design of the IOwec, it was noticed that the device needs a considerable amount of ballast. This opens the door to devising movable masses inside the hull, allowing for changes of the system's pitch inertia and, consequently, natural frequency, during operation, tuning it to the incoming wave frequency.

During the development of this project the author participated in the MIT Sandbox, an initiative to foment entrepreneurship and student ideas. The program resource's were mainly used in an attempt to identify the costs associated with the construction, installation and operation of the IOwec. Only with such a number, could a true metric of efficiency (e.g. US$/kWh) be identified and compared to other WECs currently in development and operation. However, talks with specialists in ship construction didn't result in an accurate quantification of the costs, as many divergent values were suggested. It is recommended that next steps of this project look for a solution to the cost problem, which is fundamental to understand the IOwec's place in the renewable energy market.

Appendix A

U-Tank Basic Design

The IOwec was originally designed with motion detuning passive tanks, which are usually u-shaped structures filled with water. As the hull moves, the water oscillates inside, with a natural frequency defined by its longitudinal shape. If the tank's resonance is achieved, then an anti-resonance effect on the hull occurs, drastically reducing the motion for that particular frequency. However, this hull-tank coupling only detunes the motion, meaning that two resonant peaks are created after and before the anti-resonance frequency. Figure A-1 shows an illustration of such passive tanks. Active ones would include pumps underwater or increased pressure over the free-surface to control the flow of water.

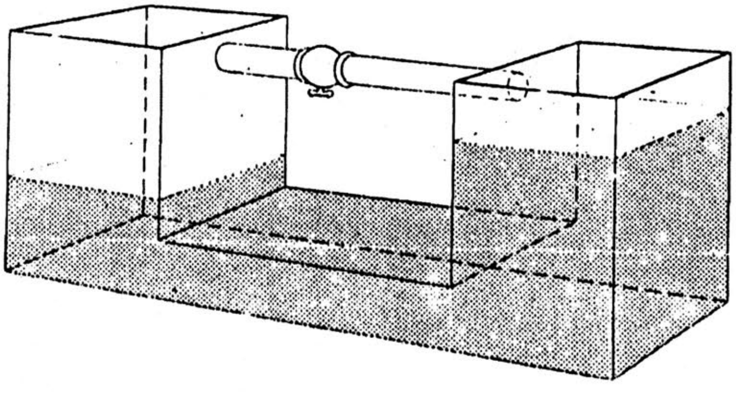

Figure A-1: Passive U-Tank used to stabilize roll motion of ships [15].

In his book, Lloyd linearizes the water flow problem inside these tanks, arriving at a very simple analytical solution. Figure A-2 shows Lloyd's illustration of the tank dimensional variables.

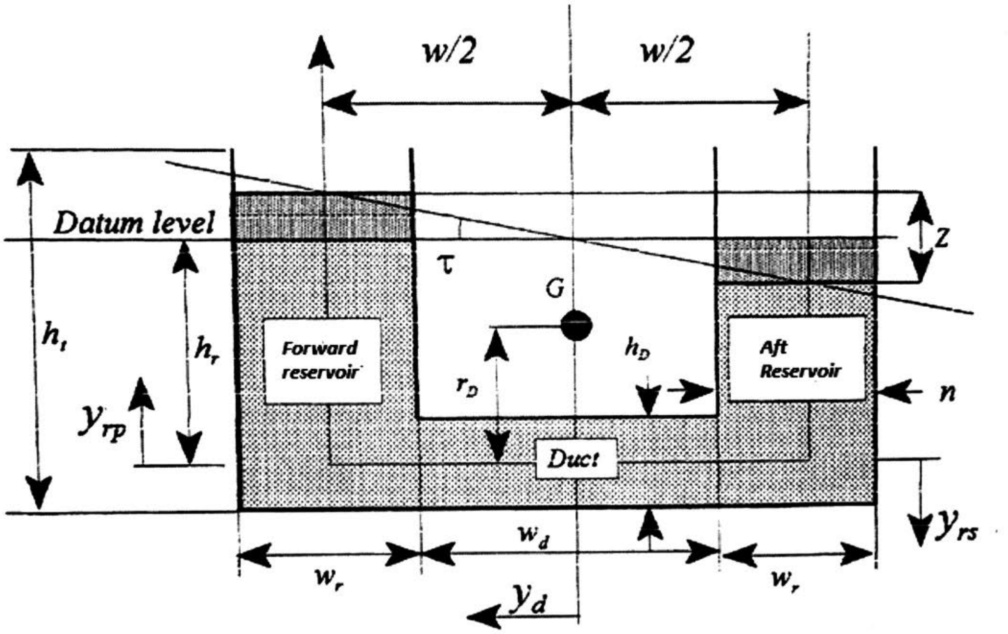

Figure A-2: Passive U-Tank dimensional variables [16].

In frequency domain, using equation 2.30 for a tank acting on the pitch direction, we find [16],

$$\xi_5 \left[-\omega^2 \left(I_{55} + a_{55}\right) + i\omega b_{55} + c_{55}\right] - \tau \left[-\omega^2 a_{5\tau} + c_{5\tau}\right] = AX_5 \tag{A.1}$$

For the water inside the tank,

$$\tau \left[-\omega^2 a_{\tau\tau} + i\omega b_{\tau\tau} + c_{\tau\tau}\right] + \xi_5 \left[-\omega^2 a_{\tau 5} + c_{\tau 5}\right] = 0 \tag{A.2}$$

The tank coefficients take the simple form [16],

$$\begin{aligned}
a_{T5} =& a_{5T} = Q_t \left(r_d + h_r \right) \\
c_{T5} =& c_{5T} = c_{TT} = Q_t g \\
a_{TT} =& Q_t w_r \left(\frac{w}{2h_d} + \frac{h_r}{w_r} \right) \\
Q_t =& \frac{\rho w_r w^2 x_t}{2} \\
b_{TT} =& 2\eta_t Q_t \sqrt{g w_r \left(\frac{w}{2h_d} + \frac{h_r}{w_r} \right)}
\end{aligned} \tag{A.3}$$

Where η_t is the non-dimensional tank damping coefficient, which is usually calculated through a simple free-decay test. The tank's natural frequency, in rad/s, takes the familiar form (also outlined by Belvins, in his Applied Fluid Dynamics Handbook) [16, 58],

$$\omega_n = \sqrt{\frac{2g}{2h_r + \frac{w_r w}{h_d}}} \tag{A.4}$$

and the maximum moment generated by the tank, ignoring damping,

$$M = Q_t g \left(1 - \frac{r_d + h_r}{w_r \left(\frac{w}{2h_d} + \frac{h_r}{w_r} \right)} \right) \tag{A.5}$$

A simple optimization can now be programmed using Microsoft Excel's solver. We will force the natural period defined through equation A.4 to be $8s$ while maximizing the moment given by relation A.5. However, some restrictions must be placed upon the variables, as they may not be larger than the hull itself, or interfere with the gyroscope housing.

Starting with known dimensions, if the gyroscope housing is $20m$ long and $5m$ deep, then $w_r \leq 20m$ and $h_d \leq 5m$. There is no reason to make the tank height less than the maximum, so $h_t = 10m$. Immediately we see the tank should be filled halfway, so as to maximize the flow,

$$h_r = \frac{h_t - h_d}{2} + \frac{h_d}{2} = 7.5m \tag{A.6}$$

By noticing that $w_r = w - w_d$, we can rewrite equation A.4 into a second order polynomial for w, which upon solving, should yield the right tank length for the desired frequency,

$$w^2 - w_d \cdot w - \left[h_d^2 + \left(14 - \frac{2g}{\omega_n^2}\right)\right] = 0 \tag{A.7}$$

Excel's solver was asked to change w_d, h_d and x_t (tank's width) to maximize equation A.5 while respecting, not only the aforementioned constraints, but also a maximum of 78% on the ratio between mass inside the tank and the hull's displacement. The last constraint made sure the tank wouldn't consume more than the available ballast. Table A.1 summarizes the dimensions found to satisfy anti-resonance at $T = 10s$. This single, large tank, will be divided into two smaller ones with half the depth and, consequently, volume, in each one.

Table A.1: U-Tank optimal dimensions for resonance at $T = 10s$.

Dimension	**Value**	**Description**
h_r	$7.50m$	Water level height
h_d	$5.00m$	Connection duct height
w_r	$5.89m$	Reservoir width
w	$30.72m$	Reservoir spacing
w_d	$24.83m$	Connection duct length
x_t	$11.78m$	U-Tank depth
m_t/Δ	46%	Ratio between the mass inside a tank and the IOwec's displacement

Using the exciting forces, added-mass and damping found by WAMIT for the bare hull case, we can get a sense on how the tank is changing the hull's motion. The IOwec's hull pitch rotation, in the frequency domain, uncoupled from heave and surge, takes the form,

$$\frac{\Xi_5}{A} = \frac{X_5\left(-\omega^2 a_{\tau\tau} + i\omega b_{\tau\tau} + c_{\tau\tau}\right)}{\left[-\omega^2\left(I_{55} + a_{55}\right) + i\omega b_{55} + c_{55}\right]\left[-\omega^2 a_{\tau\tau} + i\omega b_{\tau\tau} + c_{\tau\tau}\right] + \left[\omega^2 a_{5\tau} - c_{5\tau}\right]} \tag{A.8}$$

Finally, figure A-3 shows how the IOwec's hull pitch motion, uncoupled from heave, changes when the tank acts on it. For simplicity, we consider $b_{\tau\tau} = 0$, even though it could be estimated through a free-decay test or a Moody diagram for pipes. We can notice the anti-resonance effect exactly at $T = 10s$. However, it is worth to notice that, during his derivations, Lloyd assumes the tank's cross-sectional area doesn't change along its length. This will never be true for the IOwec due to its bottom-up tapering. In fact, there is a big change in cross-sectional area from the connecting duct extremes to its center. A more thorough analysis is required in the next design iteration of the U-tanks.

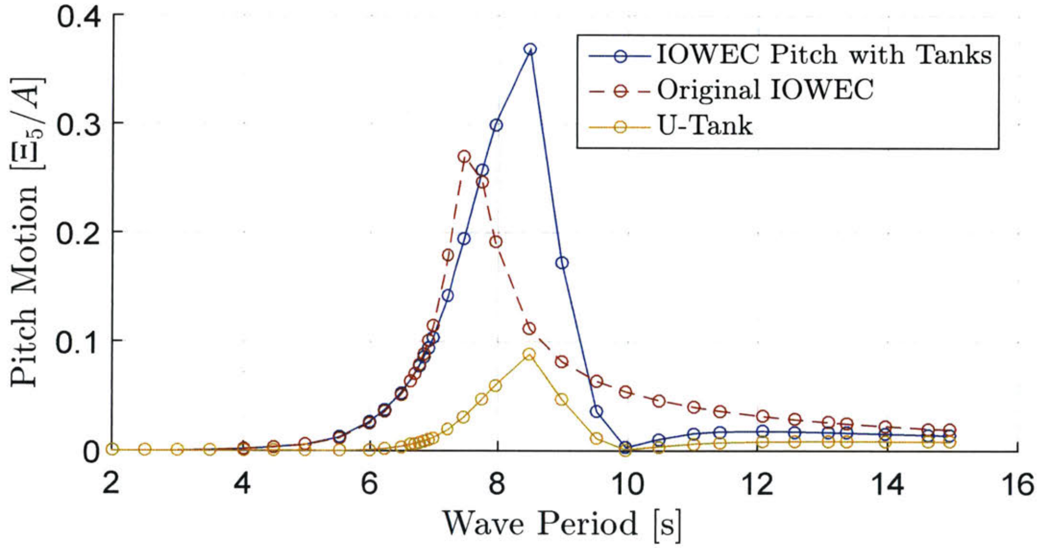

Figure A-3: U-tank action on the IOwec's bare hull when sized for resonance at $T = 10s$.

Appendix B

Oregon Sea Statistics

Table B.1: Probability of occurrence of a given H_s and T_p, with cells highlighted for values to be used in the $1/20^{th}$ scale test of the WEP [13].

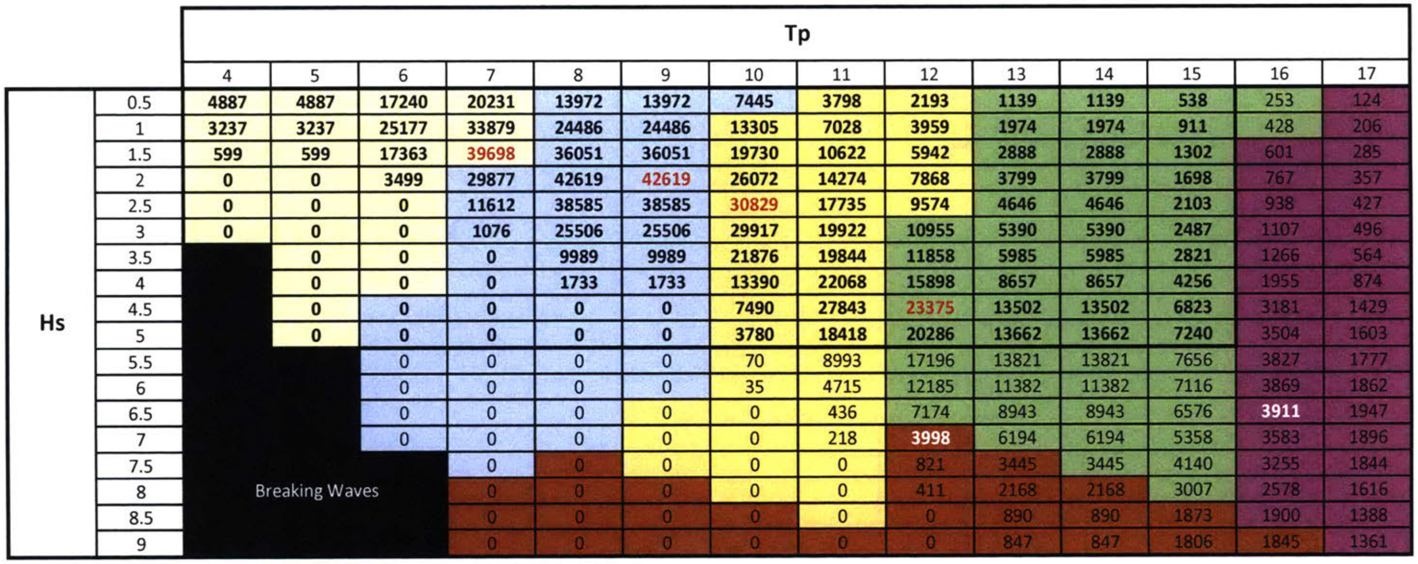

		Tp													
		4	5	6	7	8	9	10	11	12	13	14	15	16	17
Hs	0.5	**4887**	**4887**	**17240**	**20231**	**13972**	**13972**	**7445**	**3798**	**2193**	**1139**	**1139**	**538**	253	124
	1	**3237**	**3237**	**25177**	**33879**	**24486**	**24486**	**13305**	**7028**	**3959**	**1974**	**1974**	**911**	428	206
	1.5	**599**	**599**	**17363**	**39698**	**36051**	**36051**	**19730**	**10622**	**5942**	**2888**	**2888**	**1302**	601	285
	2	**0**	**0**	**3499**	**29877**	**42619**	**42619**	**26072**	**14274**	**7868**	**3799**	**3799**	**1698**	767	357
	2.5	**0**	**0**	**0**	**11612**	**38585**	**38585**	**30829**	**17735**	**9574**	**4646**	**4646**	**2103**	938	427
	3	**0**	**0**	**0**	**1076**	**25506**	**25506**	**29917**	**19922**	**10955**	**5390**	**5390**	**2487**	1107	496
	3.5		**0**	**0**	**0**	**9989**	**9989**	**21876**	**19844**	**11858**	**5985**	**5985**	**2821**	1266	564
	4		**0**	**0**	**0**	**1733**	**1733**	**13390**	**22068**	**15898**	**8657**	**8657**	**4256**	1955	874
	4.5		**0**	**0**	**0**	**0**	**0**	**7490**	**27843**	**23375**	**13502**	**13502**	**6823**	3181	1429
	5		**0**	**0**	**0**	**0**	**0**	**3780**	**18418**	**20286**	**13662**	**13662**	**7240**	3504	1603
	5.5			0	0	0	0	70	8993	17196	13821	13821	7656	3827	1777
	6			0	0	0	0	35	4715	12185	11382	11382	7116	3869	1862
	6.5			0	0	0	0	0	436	7174	8943	8943	6576	**3911**	1947
	7			0	0	0	0	0	218	**3998**	6194	6194	5358	3583	1896
	7.5				0	0	0	0	0	821	3445	3445	4140	3255	1844
	8	Breaking Waves			0	0	0	0	0	411	2168	2168	3007	2578	1616
	8.5				0	0	0	0	0	0	890	890	1873	1900	1388
	9				0	0	0	0	0	0	847	847	1806	1845	1361

Appendix C

Fourier Transform

Aegir outputs everything as time-domain signals. Usually we are interested in the amplitude and frequency of such signals, which means Fourier transform must be applied to move between time and frequency domains. Figure C-1 illustrates a pitch motion signal for $T = 8s$ of the 2 gyroscope case after both spin and damping sensibilities.

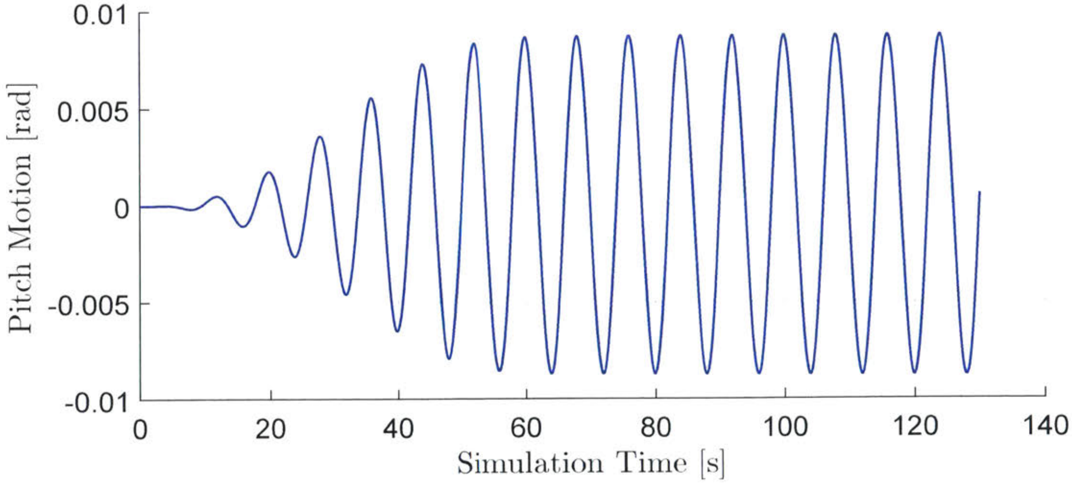

Figure C-1: Pitch motion signal for $T = 8s$ of the 2 gyroscope case after both spin and damping sensibilities.

The first step is to exclude the ramp function. We know, from table 6.2, that the steady state should be achieved around $60s$ of simulation time. If this is the case, then applying the Fourier transform to this cropped signal should yield a delta function. Figure C-2 shows the absolute value of the Fourier transform applied to the cropped signal, where, in discrete time [59],

$$|X_5(\omega)| = \left|\sum_{0}^{\infty} \xi_5[n]e^{-j\omega n}\right| \tag{C.1}$$

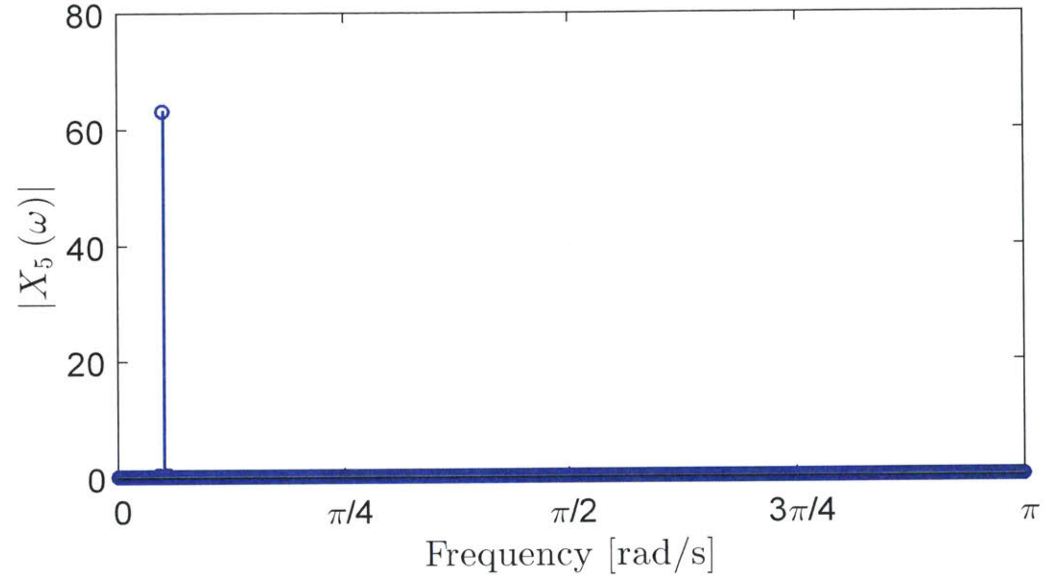

Figure C-2: Absolute value of the Fourier transform applied to the $8s$ wave motion signal. The delta function expected is found, located exactly at $8s$. By multiplying its magnitude by two and dividing by the number of samples yields the motion amplitude.

Particularly for the added-mass and damping calculations shown in section 6.2, not only the forces amplitudes are needed, but also their phase. The latter can be easily found through the ratio between the transform imaginary and real parts,

$$\epsilon_m = atan\left(\frac{Im\{X_5\}}{Re\{X_5\}}\right) \tag{C.2}$$

Bibliography

[1] I. López, J. Andreu, S. Ceballos, I. Martínez De Alegría, and I. Kortabarria, "Review of wave energy technologies and the necessary power-equipment," *Renewable and Sustainable Energy Reviews*, vol. 27, pp. 413–434, 2013.

[2] A. F. d. O. Falcão, "Wave energy utilization: A review of the technologies," *Renewable and Sustainable Energy Reviews*, vol. 14, pp. 899–918, apr 2010.

[3] OpenEI, "Marine and Hydrokinetic Technology Glossary." `http://en.openei.org/wiki/Marine_and_Hydrokinetic_Technology_Glossary`. Accessed: 09-27-2016.

[4] M. Takao and T. Setoguchi, "Air turbines for wave energy conversion," *International Journal of Rotating Machinery*, vol. 2012, 2012.

[5] N.d., "Islay LIMPET." `https://en.wikipedia.org/wiki/Islay_LIMPET`. Accessed: 09-28-2016.

[6] WavEC, "OWC PICO Power Plant." `http://www.pico-owc.net/gallery.php?cat=42&id=224&wnsid=b37ab7e8e23269e98a44080d6f89f9b8`. Accessed: 09-28-2016.

[7] H. Osawa, T. Miyazaki, and S. Miyajima, "Characteristics of Hydrodynamics and Generating Output of the Offshore Floating Wave Energy Device "Mighty Whale"," *Journal of Offshore Mechanics and Arctic Engineering*, vol. 135, p. 9, feb 2013.

[8] E. W. P. Group, "1979: Sealed gyro tube." `http://www.homepages.ed.ac.uk/v1ewaveg/`. Accessed: 10-3-2016.

[9] G. Bracco, *ISWEC : a Gyroscopic Wave Energy Converter*. PhD thesis, Politecnico di Torino, 2010.

[10] J. P. Kofoed, P. Frigaard, E. Friis-Madsen, and H. C. Sørensen, "Prototype testing of the wave energy converter wave dragon," *Renewable Energy*, vol. 31, no. 2, pp. 181–189, 2006.

[11] W. J. Pierson, G. Neumann, and R. W. James, "Observing and Forecasting Ocean Waves by Means of Wave Spectra and Statistics," *Hydrographic Office Publication*, vol. 603, p. 284, 1955.

[12] J. N. Newman, "The Motion of an Ideal Fluid," in *Marine Hydrodynamics*, ch. 4, pp. 102–158, Cambridge: MIT Press, 1977.

[13] H. Söding, *Global seaway statistics.* Arbeitsbereiche Schiffbau der Techn. Univ., 2001.

[14] D. C. Kring, *Ship motions by a three-dimensional Rankine panel method.* Doctoral thesis, Massachusetts Institute of Technology, 1994.

[15] R. Bhattacharyya, *Dynamics of Marine Vehicles.* John Wiley & Sons Inc, 1978.

[16] A. Lloyd, "Seakeeping: ship behaviour in rough weather," 1989.

[17] IEA, "Energy and Climate Change," tech. rep., International Energy Agency, Paris, jun 2015.

[18] T. S. Project, "Breakdown of Electricity Generation by Energy Source." `http://tsp-data-portal.org/Breakdown-of-Electricity-Generation-by-Energy-Source#tspQvChart`. Accessed: 12-23-2015.

[19] U.S. Energy Information Administration, "Annual Energy Outlook 2015," *Office of Integrated and International Energy Analysis*, vol. 1, pp. 1–244, 2015.

[20] B. Drew, A. Plummer, and M. N. Sahinkaya, "A review of wave energy converter technology," *Journal of Power and Energy*, vol. 223, pp. 887–902, 2009.

[21] R. Pelc and R. M. Fujita, "Renewable energy from the ocean," *Marine Policy*, vol. 26, no. 6, pp. 471–479, 2002.

[22] S. H. Salter, "Wave power," *Nature*, vol. 249, pp. 720–724, 1974.

[23] EMEC, "Wave Devices." `http://www.emec.org.uk/marine-energy/wave-devices/`. Accessed: 09-26-2016.

[24] T. V. Heath, "A review of oscillating water columns.," *Philosophical transactions. Series A, Mathematical, physical, and engineering sciences*, vol. 370, no. 1959, pp. 235–45, 2012.

[25] Y. Nagata, S. Yamashita, Y. Washio, H. Osawa, T. Ogata, and Y. Tsuritani, "The Offshore Floating Type Wave Power Device "Mighty Whale" Open Sea Tests - Environmental Conditions," *Proceedings of the Twelfth (2002) International Offshore and Polar Engineering Conference*, vol. 12, pp. 601–606, 2002.

[26] K. Budal, J. Falnes, L. Iversen, P. M. Lillebekken, G. Oltedal, T. Hals, and T. Onshus, "The Norwagian wave power buoy project," in *The second international symposium on wave energy utilization*, (Trondheim), pp. 22–24, 1982.

[27] S. F. Estefen, P. d. T. T. Esperança, E. Ricarte, P. R. da Costa, M. M. Pinheiro, C. H. P. Clemente, D. Franco, E. Melo, and J. A. de Souza, "Experimental and Numerical Studies of the Wave Energy Hyberbaric Device for Electricity Production," in *Volume 6: Nick Newman Symposium on Marine Hydrodynamics; Yoshida and Maeda Special Symposium on Ocean Space Utilization; Special Symposium on Offshore Renewable Energy*, (Estoril), pp. 811–818, ASME, jan 2008.

[28] W. Dick, "Wave Energy Converter," 2001.

[29] M.-R. Alam, "A Flexible Seafloor Carpet for High-Performance Wave Energy Extraction," in *Volume 4: Offshore Geotechnics; Ronald W. Yeung Honoring Symposium on Offshore and Ship Hydrodynamics*, (Rio de Janeiro), pp. 839–846, ASME, jul 2012.

[30] M. Lehmann, R. Elandt, H. Pham, R. Ghorbani, M. Shakeri, and M.-R. Alam, "An artificial seabed carpet for multidirectional and broadband wave energy extraction: Theory and Experiment," *Proceedings of the 10th European Wave and Tidal Energy Conference*, 2013.

[31] K. Budar and J. Falnes, "A resonant point absorber of ocean-wave power," *Nature*, vol. 256, no. 5517, pp. 478–479, 1975.

[32] Bloomberg, "Wavebob Shuts Down After Failing to Raise Funds, Find Partner." `http://www.bloomberg.com/news/articles/2013-04-03/wavebob-shuts-down-after-failing-to-raise-funds-find-partner`. Accessed: 09-30-2016.

[33] O. M. Faltinsen, *Sea Loads on Ships and Offshore Structures*. Cambridge: Cambridge University Press, 4 ed., 1998.

[34] J. Falnes, *Ocean Waves and Oscillating Systems*. Cambridge: Cambridge University Press, 1 ed., 2002.

[35] W. G. Price and R. E. D. Bishop, *Probabilistic theory of ship dynamics*. Halsted Press, 1974.

[36] C. L. Bretschneider, "Wave Variability and Wave Spetra for Wind-Generated Gravity Waves," tech. rep., Department of the Army, Washington D.C., 1959.

[37] K. Hasselmann, T. P. Barnett, E. Bouws, H. Carlson, D. E. Cartwright, K. Enke, J. A. Ewing, H. Gienapp, D. E. Hasselmann, P. Kruseman, A. Meerburg, P. Muller, D. J. Olbers, K. Richter, W. Sell, and H. Walden, "Measurements of Wind-Wave Growth and Swell Decay during the Joint North Sea Wave Project (JONSWAP)," Tech. Rep. 80, 1973.

[38] P. Ricci, J.-B. Saulnier, A. F. d. O. Falcão, and M. T. Pontes, "Time-Domain Models and Wave Energy Converters Performance Assessment," in *Volume 6:*

Nick Newman Symposium on Marine Hydrodynamics; Yoshida and Maeda Special Symposium on Ocean Space Utilization; Special Symposium on Offshore Renewable Energy, (Estoril), pp. 699–708, ASME, jan 2008.

[39] J. J. Cândido and P. A. P. Justino, "Frequency, Stochastic and Time Domain Models for an Articulated Wave Power Device," in *Volume 6: Nick Newman Symposium on Marine Hydrodynamics; Yoshida and Maeda Special Symposium on Ocean Space Utilization; Special Symposium on Offshore Renewable Energy*, (Estoril), pp. 633–643, ASME, jan 2008.

[40] S. J. Beatty, C. Hiles, R. S. Nicoll, J. E. Adamson, and B. J. Buckham, "Design Synthesis of a Wave Energy Converter," in *Volume 4: Ocean Engineering; Ocean Renewable Energy; Ocean Space Utilization, Parts A and B*, (Honolulu), pp. 891–900, ASME, 2009.

[41] K. Rhinefrank, A. Schacher, J. Prudell, J. Cruz, N. Jorge, C. Stillinger, D. Naviaux, T. Brekken, A. von Jouanne, D. Newborn, S. Yim, and D. Cox, "Numerical and Experimental Analysis of a Novel Wave Energy Converter," in *29th International Conference on Ocean, Offshore and Arctic Engineering: Volume 3*, (Shanghai), pp. 559–567, ASME, 2010.

[42] M. J. Muliawan, Z. Gao, T. Moan, and A. Babarit, "Analysis of a Two-Body Floating Wave Energy Converter With Particular Focus on the Effects of Power Take Off and Mooring Systems on Energy Capture," in *Volume 5: Ocean Space Utilization; Ocean Renewable Energy*, (Rotterdam), pp. 317–328, ASME, 2011.

[43] J. J. M. B. Cândido, P. a. P. Justino, and J. C. C. Henriques, "Frequency and Stochastic Domain Models for Two Geometries of the IPS Wave Power Buoy," in *9th European Wave and Tidal Energy Conference*, p. 10, 2011.

[44] B. Passione, *Modelling and Control of wave energy converters*. PhD thesis, Politecnico di Torino, 2014.

[45] R. Eatock Taylor, P. H. Taylor, and P. K. Stansby, "A coupled hydrodynamic-structural model of the M4 wave energy converter," *Journal of Fluids and Structures*, vol. 63, pp. 77–96, 2016.

[46] M. D. Haskind, "The Exciting Forces and Wetting of Ships in Waves," tech. rep., Izvest Akademii Nauk SSSR, 1957.

[47] J. N. Newman, "The Interaction of Stationary Vessels with Regular Waves," in *Eleventh Symposium on Naval Hydrodynamics*, (London), pp. 491–501, University College London, MIT, 1977.

[48] H. Lamb, *Hydrodynamics*. Cambridge: Cambridge University Press, 6 ed., 1932.

[49] C. H. Lee, "WAMIT User Manual," tech. rep., WAMIT Inc., Cambridge, 2008.

[50] W. E. Cummins, "The impulse response function and ship motions," Tech. Rep. DTMB-1661, David Taylor Model Basin, Washington D.C., 1962.

[51] T. Perez and T. I. Fossen, "Joint Identification of Infinite-Frequency Added Mass and Fluid-Memory Models of Marine Structures," *Modeling, Identification and Control: A Norwegian Research Bulletin*, vol. 29, no. 3, pp. 93–102, 2008.

[52] T. Perez and T. I. Fossen, "Time- vs. Frequency-domain Identification of Parametric Radiation Force Models for Marine Structures at Zero Speed," *Modeling, Identification and Control: A Norwegian Research Bulletin*, vol. 29, no. 1, pp. 1–19, 2008.

[53] U. D. of Energy, "IOwec." `http://waveenergyprize.org/teams/iowec`. Accessed: 10-18-2016.

[54] ABS, "Rules for Building and Classing Steel Vessels," tech. rep., 2015.

[55] ABS, "Rules for Building and Classing Steel Barges," tech. rep., 2015.

[56] T. F. Ogilvie and E. O. Tuck, "A rational strip theory of ship motions: part I," tech. rep., University of Michigan Ann Arbor, Ann Arbor, 1969.

[57] J. H. Freziger and M. Peric, *Computational Methods for Fluid Dynamics*. No. 3, Springer, 2003.

[58] R. D. Blevins, "Applied fluid dynamics handbook," *New York, Van Nostrand Reinhold Co., 1984, 568 p.*, vol. 1, 1984.

[59] A. V. Oppenheim, A. S. Willsky, and S. H. Nawab, *Signals and systems*, vol. 2. Prentice-Hall Englewood Cliffs, NJ, 1983.